

NMR imaging of curing of alkyds and moisture transport through coatings on wood

Citation for published version (APA):

Gezici - Koç, Ö. (2018). *NMR imaging of curing of alkyds and moisture transport through coatings on wood*. [Phd Thesis 1 (Research TU/e / Graduation TU/e), Applied Physics and Science Education]. Technische Universiteit Eindhoven.

Document status and date:

Published: 10/12/2018

Document Version:

Publisher's PDF, also known as Version of Record (includes final page, issue and volume numbers)

Please check the document version of this publication:

- A submitted manuscript is the version of the article upon submission and before peer-review. There can be important differences between the submitted version and the official published version of record. People interested in the research are advised to contact the author for the final version of the publication, or visit the DOI to the publisher's website.
- The final author version and the galley proof are versions of the publication after peer review.
- The final published version features the final layout of the paper including the volume, issue and page numbers.

[Link to publication](#)

General rights

Copyright and moral rights for the publications made accessible in the public portal are retained by the authors and/or other copyright owners and it is a condition of accessing publications that users recognise and abide by the legal requirements associated with these rights.

- Users may download and print one copy of any publication from the public portal for the purpose of private study or research.
- You may not further distribute the material or use it for any profit-making activity or commercial gain
- You may freely distribute the URL identifying the publication in the public portal.

If the publication is distributed under the terms of Article 25fa of the Dutch Copyright Act, indicated by the "Taverne" license above, please follow below link for the End User Agreement:

www.tue.nl/taverne

Take down policy

If you believe that this document breaches copyright please contact us at:

openaccess@tue.nl

providing details and we will investigate your claim.

NMR imaging of curing of alkyds and moisture transport through coatings on wood

PROEFSCHRIFT

ter verkrijging van de graad van doctor aan de Technische Universiteit Eindhoven,
op gezag van de rector magnificus prof.dr.ir. F.P.T. Baaijens, voor een commissie
aangewezen door het College voor Promoties, in het openbaar te verdedigen op
maandag 10 December 2018 om 11:00 uur

door

Özlem Gezici Koç

geboren te İzmir, Turkije

Dit proefschrift is goedgekeurd door de promotoren en de samenstelling van de promotiecommissie is als volgt:

voorzitter:	prof.dr.ir. E.J.E. Cottaar
1 ^e promotor:	prof.dr.ir. O.C.G. Adan
2 ^e promotor:	prof.dr. J.L. Keddie (University of Surrey)
copromotor:	dr.ir. S.J.F. Erich
leden:	prof.dr. S. Stenstrom (Lund University) prof.dr. H. Militz (Georg-August-Universität Göttingen) prof.dr.ir. R. Tuinier
adviseur:	ing. L.G.J. van der Ven

Het onderzoek dat in dit proefschrift wordt beschreven is uitgevoerd in overeenstemming met de TU/e Gedragscode Wetenschapsbeoefening.

To my family

To Ali'm

Aileme

Ali'me

A catalogue record is available from the Eindhoven University of Technology Library
ISBN: 978-90-386-4651-0

Cover photo: İsa&Rengin Yıldız, *Cover design:* Özlem Gezici Koç

Printed by: GildePrint Drukkerijen - Enschede

The research in this thesis has been carried out in the group Transport in Permeable Media at the Eindhoven University of Technology, Department of Applied Physics. This work is supported by TNO, TU/e and AkzoNobel Decorative Paints.

Contents

Chapter 1 - Introduction	1
1.1. The context of coating research and development.....	1
1.2. Stricter environmental legislation as a key driver for coating innovation.....	1
1.2.1. Replacing cobalt-based driers is a major challenge.....	2
1.2.2. Reducing Volatile Organic Compounds (VOCs) impacts coating performance.....	4
1.3. Objectives and outline of the thesis	5
Chapter 2 - In-depth study of drying solvent-borne alkyd coatings in presence of Mn- and Fe- based catalysts as cobalt alternatives	9
2.1. Introduction.....	10
2.2. Experimental section	12
2.2.1. Materials	12
2.2.2. Experimental methods.....	13
2.3. Results and discussion	15
2.3.1. NMR profiles of drying alkyd films.....	15
2.3.2. Measuring the drying time, i.e. the formation of film spanning networks.....	19
2.3.3. Time evolution of chemical changes during drying	20
2.3.4. Glass transition temperatures and crosslink densities of dried films	23
2.3.5. A conceptual model for drying process	25
2.4. Conclusion	26
Chapter 3 - The influence of calcium and zirconium based secondary driers on drying solvent borne alkyd coatings	29
3.1. Introduction.....	30
3.2. Experimental section	31
3.2.1. Materials and coating preparation	31
3.2.2. Experimental methods.....	32
3.3. Results and Discussion.....	35
3.3.1. NMR profiles of drying alkyd coatings	35
3.3.2. The frontlike curing of alkyd coatings using different drier combinations.....	39
3.3.3. Characterization of the observed inhibition period.....	42
3.3.4. Glass transition temperatures and crosslink densities of dried films	45
3.3.5. The effect of secondary driers on crosslink density and front speed	46
3.4. Conclusions.....	47
Chapter 4 - Bound and free water distribution in wood during water uptake and drying as measured by 1D magnetic resonance imaging	49
4.1. Introduction.....	50
4.2. Materials and methods.....	51

4.2.1. Wood types.....	51
4.2.2. NMR imaging and relaxometry.....	53
4.2.3. Relaxation analysis of water in wood.....	55
4.2.4. Sample preparation for calibrating the NMR signal.....	56
4.2.5. Samples and sample holders for water uptake and drying.....	57
4.2.6. Dynamic Vapor Sorption (DVS).....	58
4.3. Results and Discussion.....	58
4.3.1. Equilibrium water sorption and signal calibration.....	58
4.3.2. The state of water in wood during water uptake and drying.....	61
4.3.3. Effective diffusion coefficient.....	65
4.4. Conclusions.....	70
4.5. Appendix.....	71
Chapter 5 - Understanding the influence of wood as a substrate on the permeability of coatings by NMR imaging and wet-cup.....	73
5.1. Introduction.....	74
5.2. Materials and methods.....	75
5.2.1. Wood and coating types.....	75
5.2.2. Coatings on wood.....	76
5.2.3. NMR imaging and relaxometry.....	79
5.2.4. Free films.....	80
5.2.5. Dynamic Vapor Sorption (DVS).....	81
5.2.6. Wet-cup method.....	82
5.3. Results and discussion.....	82
5.3.1. Uncoated wood versus coated wood.....	82
5.3.2. Combinations of wood and coatings types.....	83
5.3.3. Permeability of coatings.....	85
5.4. Conclusions.....	93
Chapter 6 - Moisture content of the coating determines the water permeability as measured by 1D magnetic resonance imaging.....	95
6.1. Introduction.....	96
6.2. Materials and methods.....	97
6.2.1. Wood and coating types.....	97
6.2.2. Coatings on wood.....	98
6.2.3. NMR imaging and relaxometry.....	100
6.3. Results and discussion.....	102
6.3.1. Water uptake.....	102
6.3.2. Drying after water uptake.....	105
6.3.3. Permeability of coatings.....	107
6.4. Conclusions.....	113

Chapter 7 - Conclusions and Outlook	115
7.1. Conclusions.....	115
7.1.1. The influence of cobalt alternatives and secondary driers on curing of alkyds.....	115
7.1.2. The permeability of a coating as a function of wood type and the water activity	116
7.2. Outlook	117
7.2.1. Understanding the relation between oxygen diffusion and crosslinking of alkyds	117
7.2.2. The factors influencing the permeability of a coating	118
7.2.3. Curing of alkyds on wood and moisture transport at wood-coating interface	121
Bibliography	123
Summary	133
Samenvatting	137
List of publications	141
Acknowledgement	143
Curriculum Vitae	147

Chapter 1

Introduction

1. Introduction

1.1. The context of coating research and development

Paints and coatings are applied on substrates for protective, decorative and/or other specific purposes. They can be found everywhere, e.g. on furniture, cars, airplanes, plastics, and buildings. In addition to protecting the underlying substrate, such as metals from corrosion or wood against moisture-related degradation, coatings also provide color and a pleasant decorative finish.

Coatings normally consist of binders, solvents, pigments, and additives. The binder is the polymeric material as a film-forming agent and provides a matrix in which all other components are incorporated. The choice of the binder depends on the substrate, whether it is wood, steel or concrete, and also on whether the coating is for indoor or outdoor use. The most common binders are alkyds, acrylics, polyurethanes, polyesters and epoxies. The continuous phase in a coating dispersion or emulsion is either a volatile organic liquid as solvent or water to provide a proper viscosity during manufacture, application, and film formation. Pigments are used to provide color to the coating, or to act as corrosion inhibitor, or to protect wood from photodegradation. Additives have very specific purposes to add functionality or improve performance, such as thickening agents, surface-active agents, surface modifiers, catalysts, biocides, etc., and are typically added to the coatings in very small amounts.

This thesis focuses on wood coatings. Wood is different than the other substrates (such as metal or plastic), in which it is derived from a *tree*, a living organism. This feature influences the ideal choice of coating, thus the properties of wood coatings are dependent on the combination of specific constituents, and as well as its interaction with the wood substrate. Research on and development of coatings has a long history, which has been directed and dominated by major issues like raw material availability, environmental pressure and end-user demands.

1.2. Stricter environmental legislation as a key driver for coating innovation

The awareness of the environmental risks of several coating ingredients has increased much in the last decades. Therefore, more environmental friendly constituents in the coating formulations have gained interest. One is the tendency to replace cobalt-based alkyd driers with more environmentally friendly alternatives. Another environmental issue concerns the

stricter regulations for usage and emissions of volatile organic compounds (VOCs) in coatings, especially in wood coatings.

The most important environmental legislations that have a major impact on the coating industry are discussed below.

1.2.1. Replacing cobalt-based driers is a major challenge

Alkyd based paints are widely used as air drying coatings. Besides their cost-effectiveness and wide application in different techniques, alkyd resins have a low surface tension that enables the application on a variety of substrates^{1,2}. Without any catalysts, the natural drying time of alkyd based coatings would be weeks or months, which is not desirable from practical point of view. The autoxidation process can be accelerated by adding catalysts, so-called driers. Generally, these driers are transition metals forming a complex with organic ligands.

Cobalt-based driers are commonly used drying catalysts as they lead to highly crosslinked and hard films. However, several environmental studies have indicated potential health implications of cobalt-based alkyd driers^{3,4}. The European Chemicals Agency (ECHA) considers several cobalt compounds for authorization under REACH (Registration, Evaluation, Authorization and Restriction of Chemicals). Cobalt REACH Consortium classified some cobalt compounds including carboxylates under the EU CLP (Classification, Labelling and Packaging) Regulation as CMR 2-Reprotoxic⁵. CMR stands for carcinogenic, mutagenic and reprotoxic (toxic to reproduction). In near future, cobalt-based driers may be reclassified to carcinogenic class 1B. Therefore, there is a clear driver to replace cobalt-based driers by eco-friendlier alternatives.

In order to replace cobalt based driers, understanding the oxidation process by metal catalysts is necessary. Because of the complex nature of alkyd resins, model compounds, such as simple dienes and fatty acid esters, or oils as a precursor to an actual alkyd resin, have been extensively investigated for understanding the mechanism of drying alkyd resins⁶⁻¹³. The drying starts with the solvent evaporation (physical drying) when applied to a substrate. It is followed by autoxidation of the binder forming crosslinks (chemical curing) resulting in an increase of hardness over time. The chemical curing of alkyd resin consists of four main steps^{12,14-19}. These steps include (1) an induction (inhibition) period, (2) hydroperoxide formation, (3) hydroperoxide decomposition, and (4) crosslinking. The induction (inhibition) period is considered a measure for the ability of the catalyst to initiate the hydroperoxide formation by absorbing oxygen from the air^{12,14,15,20}. The presence of driers shortens the induction period and accelerates hydroperoxide formation and their decomposition into radicals resulting in active crosslinking sites.

With reference to the function of driers on the oxidative drying of the alkyd, driers are commonly divided into two main classes: primary and secondary driers. Primary driers

promote oxygen uptake, hydroperoxide formation and decomposition processes², whereas secondary driers are said to enhance the crosslinking of the film. The oxidative drying of alkyds by cobalt alternatives has been mostly studied using manganese (Mn)^{9,11–14,21–24} or iron (Fe)^{10,25–31} as primary driers. As the redox potential of these metal compounds is much lower than that of cobalt, the drying performance of non-cobalt driers needs to be improved by adding organic chelating ligands^{9,11,12,14,23,24}.

Primary driers are used in combination with secondary driers to enhance homogeneous drying of the film. The most commonly used secondary driers are calcium and zirconium. Many statements are made on the working mechanisms of secondary driers, ranging from promotion of oxygen transport, formation of physical links in the network, and keeping the primary driers active^{6,15,32}. However, the working mechanism of secondary driers in combination with the cobalt alternatives (and even for cobalt) has many open questions.

During the search for and development of potential alternative drier systems, model compounds, such as (m)ethyl esters of fatty acids and drying oils, were used^{8–14,23,24}. Although such model systems have added value in rapid screening, results may not be representative for the actual performance of (real) alkyd systems. Studies showed that oxygen transport properties of alkyd coatings have important impact on the oxidative drying of alkyds, and influence the final hardness of the film^{21,22}. There are only a few studies on real alkyd coatings with cobalt alternatives.

These studies can be divided into two research categories. The first category investigates the proposed drier system to evaluate the hardness of the created alkyd film as a function of time, while monitoring the kinetics of oxidative drying in alkyd coatings³⁰ or model systems^{27–29}. The second category investigates the influence of available manganese-based alternatives (as compared to cobalt-based driers) on the film formation process and final network structure of alkyd coatings^{21,22}. Results underline that the curing process of an alkyd coating is strongly influenced by the type of catalyst. While a sharp drying front was observed for cobalt-based catalyst, more homogeneous drying was observed for manganese-based catalysts. The differences can be explained by the changes in the reaction rate and oxygen diffusion constant^{21,22}. In conclusion, an in-depth understanding of the film formation under the influence of cobalt alternatives is lacking.

In order to investigate the influence of the drier on the film formation properties of alkyd coatings, there are many available techniques. However, most of them do not allow measuring the drying (curing) process as a function of depth. Confocal Raman Microscopy (CRM) is used for chemical profiling by following the disappearance of double bonds^{33–35}. Time resolved Attenuated Total Reflectance Fourier Transform Infrared (ATR-FTIR) spectroscopy allows chemical profiling, but only on the substrate side of the alkyd film^{12,13}. Both techniques are only sensitive to oxidation products, and do not give information about

the crosslinking reactions. A technique capable of giving an information about the crosslinking reactions is needed to study the influence of driers on the film formation.

1.2.2. Reducing Volatile Organic Compounds (VOCs) impacts coating performance

Another driver for coating innovation is due to stricter regulations concerning the usage and emission of volatile organic compounds (VOCs). In addition to affecting the environment, VOCs are posing health risks to humans when improperly handled^{36,37}. As a result, the amount of VOCs in wood coatings has been regulated. The European Commission/the Paints Directive 2004/42/EC has permitted 150 g/l for waterborne and 400 g/l for solventborne coatings since January 2007. As from January 2010, it has been reduced to 130 g/l for waterborne and 300 g/l for solventborne wood coatings³⁸.

With the regulations on VOCs and new technical developments, waterborne coatings are becoming more and more common in the wood coatings sector. However, waterborne coatings are more sensitive to water compared to solventborne coatings³⁹. It has led to an increased interest in studying the influence of coatings on the changes of wood moisture content³⁹⁻⁴⁵.

Understanding the changes of wood moisture content is of practical importance, since the mechanical properties or the dimensional stability of wood are influenced by the moisture content. It can be explained by the nature of wood being hygroscopic and porous in which the distribution and interactions with water play a crucial role in wood processing and durability. Moreover, a high moisture content may result in durability loss due to fungal growth and/or delamination of an applied protective coating.

Since protection of the substrate is a main feature of coatings, getting knowledge on how a coating resists and interacts with water is helpful in predicting the service life of the wood substrate and the coating. As a first step, the influencing factors on the coating performance against water should be identified. These factors can be the wood substrate, the type of binder, pigmentation, film thickness, etc. Several approaches have been used to understand mostly the influence of coating type on water transport through coated wood and resulting wood moisture content. For example, water transport properties through coatings have been investigated by measuring the average moisture content in bulk wood³⁹⁻⁴¹. Further, many studies prove the inhomogeneous distribution of water close to the surface⁴²⁻⁴⁵. There is a method required to monitor the moisture content of coated wood with spatial and time resolution. This method is specifically necessary for a thorough understanding the role of each factor on the permeability of coatings.

1.3. Objectives and outline of the thesis

The present thesis deals with film making properties of alkyd coatings under the influence of different driers and moisture transport through coatings on wood.

An in-depth understanding of (i) the film formation under the influence of cobalt alternatives and their combination with secondary driers, and (ii) the influence of each factor - the wood substrate, the type of binder, film thickness, etc. – on the permeability of a wood coating, is necessary.

A schematic drawing of a coated wood and the influencing factors on the moisture transport through coatings on wood is given in Figure 1.1.

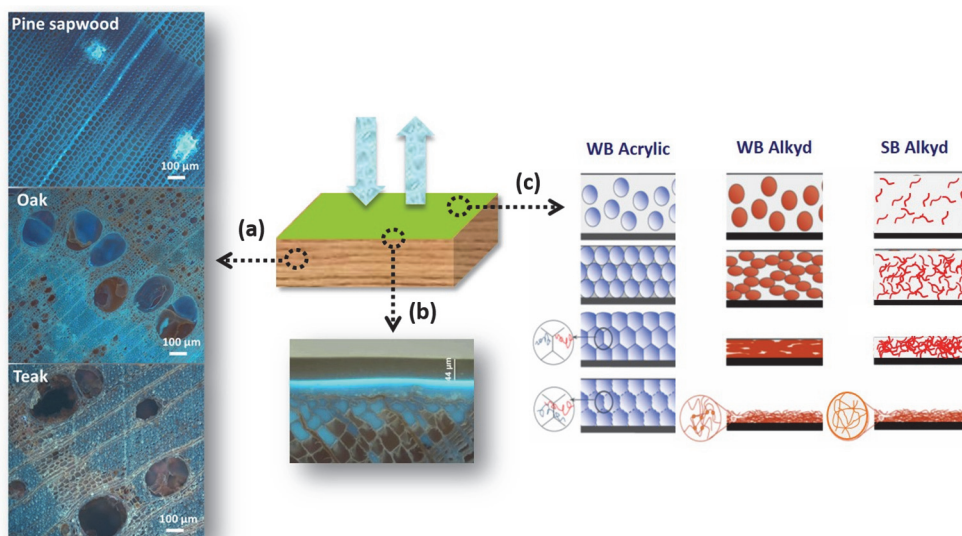


Figure 1.1. Schematic representation of each component in the present study of moisture transport through coatings on wood, covering research questions: wood type, interface effect, coating type. (Microscope images by Paul van de Keer, AkzoNobel).

As illustrated in the figure, the coated wood has mainly three parts that may influence the water transport through coatings on wood. Following the arrows in the figure, these parts are:

The wood substrate. The porous structure of wood samples – pine sapwood, oak and teak – is shown by microscope images.

The wood-coating interface. An example of coating penetration in wood and forming an interface layer is shown by a microscope image.

The coating film. The schematic diagram shows the steps from the moment of application till the final film formation. The binder type influences the film formation, such as coalescing of acrylics or crosslinking of alkyds. This may influence the final film properties.

A technique is needed which is capable of (i) giving an information about the crosslinking reactions to study the influence of driers on the film formation, and (ii) monitoring the moisture content of the coated wood to study the barrier properties of coatings, with spatial and time resolution. Nuclear Magnetic Resonance (NMR) imaging is a non-invasive method that meets these requirements.

High spatial resolution NMR imaging is proved to be an appropriate technique to study crosslinking of alkyd films^{15,20–22,35,46–50}. NMR imaging is employed to probe the density of mobile protons as a function of depth in the drying films. The conventional techniques like the Beck-Koller drying test and König hardness measurements for measuring the drying time and hardness development of the alkyd film can be used in conjunction with NMR imaging in order to provide empirical based interpretation on the drying performance. Additionally, Dynamic Mechanical Analysis (DMA) appears to be an important method to correlate the crosslinked network structure of the films to the mechanical properties⁵¹.

Moreover, NMR imaging is proved to be an excellent tool as well to determine the distribution and the concentration of water in wood/coated wood^{42,44,52–55}. It can be used to study the water transport through coatings on wood, in which it provides temporally and spatially resolved moisture profiles⁵⁶. Another important advantage of NMR imaging over other methods (such as weighing⁵⁷ or X-ray computer tomography (CT)⁵⁸ or neutron radiography⁵⁹) is its ability to distinguish the state of moisture as bound or free water. It allows understanding the transport properties by following the changes in bound and free water.

There are two main objectives in this thesis. The first objective is to have a more in-depth understanding of drying (curing) of alkyd coatings under the influence of cobalt alternatives, and the working mechanism of secondary driers in combination with the cobalt alternatives (and even for cobalt). The second objective is to determine the permeability dependence as a function of the wood type, the binder (coating) type, the wood-coating interface, and the moisture content of the coating.

Accordingly, the themes focused in this thesis can be divided into two parts. The first part consists of Chapter 2 and 3, which investigate the oxidative drying of solventborne alkyd coatings with different primary and secondary driers. The second part consists of Chapters 4 to 6, which result from a comprehensive study on moisture transport through coatings on wood. While Chapter 4 only deals with wood, coated wood has been studied in Chapters 5 and 6. Chapter 7 summarizes the main conclusions of this work and recommendations for future research.

The chapters 2 to 7 are outlined as follows.

In **Chapter 2**, we investigate the influence of cobalt and alternative metals (Mn and Fe) on the oxidative drying of alkyd coating films using a combination of techniques. NMR profiling is used for the first time in conjunction to time-resolved ATR-FTIR and standard methods like Beck-Koller (BK) drying, König hardness test and DMA. High spatial resolution NMR profiles and T_2 (spin-spin relaxation time) analysis as a function of depth and time are discussed. Simultaneously, the drying performance, hardness, and characteristics of the crosslinked film are evaluated.

In **Chapter 3**, we investigate the influence of the presence of secondary driers (Ca and Zr) on the oxidative drying of alkyd coating films using the same primary driers as in Chapter 2. To follow the curing process, NMR profiling is employed. The fully cured films are also characterized with DMA. This allows us to relate the NMR results to the crosslinked network structure of the coating layers and to the final mechanical properties. We investigate the drying profiles, characterization of front-speeds, inhibition periods, and final crosslink densities to unravel the influence of the secondary driers.

In **Chapter 4**, we analyze the water transport through wood itself; pine sapwood, oak and teak. We aim to visualize and quantify bound and free water distribution for the selected wood types during water uptake and drying by using NMR imaging and relaxometry. A calibration is performed to determine the different water states in each different wood type and to convert the NMR signal into moisture content. Experimentally determined diffusion constants are compared with those derived by the diffusion models for conceptual understanding of transport mechanism.

In **Chapter 5**, we elucidate the influence of the wooden substrate on the water permeability of the coating applied on it. NMR imaging is used to measure the moisture content distribution and quantify the changes in bound and free water in wood (pine sapwood, teak and oak) as a function of coating type (SB alkyd, WB alkyd and WB acrylic) during drying of completely water saturated samples. The permeability of free coating films is determined by wet-cup method, followed by comparison with the permeability of wood supported films.

In **Chapter 6**, we investigate the sensitivity of the permeability of coatings on wood against moisture during long term exposure to liquid water and subsequent drying below FSP. The same combinations of wood and coating types in Chapter 5 are studied. The moisture content (MC) distribution in coated wood is measured during liquid water uptake and subsequent drying. Besides the MC profiles, relaxation analysis is used to identify and quantify the state of water during water uptake. The average moisture content in coated wood is found for permeability calculations, followed by the correlation of permeability

results with the average water activity in the coating, and the sorption isotherms of the coatings.

In **Chapter 7**, the thesis concludes with the key conclusions and sketches on path of following research.

Chapter 2

In-depth study of drying solvent-borne alkyd coatings in presence of Mn- and Fe-based catalysts as cobalt alternatives

As a result of potential reclassification of cobalt-based alkyd driers, many studies have been conducted to find suitable alternatives as primary driers in alkyd paints. Some commercial replacements are currently available. A systematic investigation on the oxidative drying of solventborne alkyd coatings with commercial cobalt-free driers has been performed, a cobalt-based drier as a reference and an iron-based drier and two manganese-based driers. This work investigates how these driers influence the molecular network development and mechanical properties of the final films from the moment of application to full drying. High spatial resolution NMR profiling allows tracing the depth-resolved crosslinking during drying, and is used for the first time in conjunction with time-resolved ATR-FTIR and standard methods like the Beck-Koller (BK) drying test, König hardness and DMA. Based on the results from these different techniques, we found correlations between the drying pattern of driers and properties such as the drying rate, the overall and depth-resolved crosslink density and hardness development. This study shows that front drying works best to obtain densely crosslinked hard films. In the case of demanding a fast drying, a drier promoting homogeneous drying without an induction period is preferred, still resulting in a film with a reasonable crosslink density and hardness.

This chapter has been published as

Ö. Gezici-Koç et al., *Materials Today Communications* 7: 22-31 (2016).

2. In-depth study of drying solvent-borne alkyd coatings in presence of Mn- and Fe- based catalysts as cobalt alternatives

2.1. Introduction

Alkyd based paints are widely used as air drying coatings. Besides their cost-effectiveness and wide application in different techniques, alkyd resins have a low surface tension that enables the application on a variety of substrates^{1,2}. The natural drying time of alkyd based coatings would be weeks or months, which is not desirable from the practical point of view. The autoxidation process can be accelerated by adding catalysts, the so-called driers. Generally, these driers are transition metals forming a complex with organic ligands. Cobalt based driers are the most used drying catalysts as they lead to highly crosslinked and hard films. However, several environmental studies have suggested potential reclassification of cobalt-based alkyd driers^{3,4}. Therefore, cobalt based driers are being replaced by its alternatives.

In order to replace cobalt based driers, understanding the oxidation process by metal catalysts is necessary. Because of the complex nature of alkyd resins, model compounds such as simple dienes and fatty acid esters, or oils as a precursor to an actual alkyd resin have been extensively investigated⁶⁻¹³. The drying starts with the solvent evaporation (physical drying) when applied to a substrate. It is followed by autoxidation of the binder forming crosslinks (chemical curing) resulting in an increase of hardness over time. The chemical curing of alkyd resin consists of four main steps^{12,14-19}. These steps include (1) the induction period, (2) hydroperoxide formation, (3) hydroperoxide decomposition, and (4) crosslinking. The induction period is considered as a measure for the ability of the catalyst to initiate the hydroperoxide formation by absorbing oxygen from the air^{12,14,15,20}. The presence of driers shortens the induction period and accelerates hydroperoxide formation and their decomposition into radicals resulting in active crosslinking sites.

Regarding the function of driers on the oxidative drying of the alkyd, they are commonly divided into two main classes: primary and secondary driers. Primary driers promote oxygen uptake, hydroperoxide formation and decomposition processes². Primary driers are used in combination with secondary driers to enhance homogeneous drying of the film. The oxidative drying of alkyds by cobalt alternatives has been mostly studied using manganese (Mn)^{9,11-14,21-24} or iron (Fe)^{10,25-31} as primary driers. As the redox potential of these metal compounds is much lower than that of cobalt, the drying performance of non-cobalt driers needs to be improved by adding organic chelating ligands^{9,11,12,14,23,24}.

During the development of potential alternative drier systems, model compounds, such as (m)ethyl esters of fatty acids and drying oils, were used^{8-14,23,24}. Although such model systems have added value in rapid screening, results may not be representative for the actual performance of (real) alkyd systems. Studies showed that oxygen transport

properties of alkyd coatings have important impact on the oxidative drying of alkyds, and influence the final hardness of the film ^{21,22}. There are only a few studies on real alkyd coatings with cobalt alternatives. These studies can be divided into two research categories. The first category investigates the proposed drier system to assess the hardness of the created alkyd film as a function of time, while monitoring the kinetics of oxidative drying in alkyd coatings ³⁰ or model systems ^{27–29}. The second category investigates the influence of available manganese based alternatives (as compared to cobalt based driers) on the film formation process and final network structure of alkyd coatings ^{21,22}. Results underline that the curing process of an alkyd coating is strongly influenced by the type of catalyst. While a sharp drying front was observed for cobalt based catalyst, more homogeneous drying was observed for manganese based catalysts. The differences can be explained by the changes in the reaction rate and oxygen diffusion constant ^{21,22}. These studies show that it is necessary to have a more in-depth understanding of the film formation under the influence of cobalt alternatives.

There are many techniques allowing to investigate the influence of the drier on the drying process of alkyd films. However, most of them do not allow measuring the curing process as a function of depth. Confocal Raman Microscopy (CRM) and Nuclear Magnetic Resonance (NMR) profiling are the only techniques in this sense. CRM is used for chemical profiling by following the disappearance of double bonds ^{33–35}. Time resolved Attenuated Total Reflectance Fourier Transform Infrared (ATR-FTIR) spectroscopy allows chemical profiling, but only on the substrate side of the alkyd film ^{12,13}. Both techniques are only sensitive to oxidation products, and do not give information about the crosslinking reactions. High spatial resolution NMR profiling proved to be an appropriate noninvasive technique to study crosslinking of alkyd films ^{15,20–22,35,46–50}. NMR profiling is employed to probe the density of mobile protons as a function of depth in the drying films. Initially, the NMR signal decreases as solvent evaporates during the physical drying, because highly mobile protons of the solvent are lost. Further decrease in signal is a result of reduced mobility due to crosslinking ^{15,20–22,35,46–50}. The conventional techniques like the Beck-Koller drying test and König hardness measurements for measuring the drying time and hardness development of the alkyd film can be used in conjunction with the previous techniques in order to provide empirical based interpretation on the drying performance. Moreover, Dynamic Mechanical Analysis (DMA) represents an important method to correlate the crosslinked network structure of the films to the mechanical properties ⁵¹.

In this study, we investigate the influence of cobalt and alternative metals on the oxidative drying of alkyd coating films using a combination of techniques. NMR profiling is used for the first time in conjunction to time-resolved ATR-FTIR and standard methods like Beck-Koller (BK) drying, König hardness test and DMA. Besides a cobalt based drier, alkyd coatings with three commercially available primary drier systems have been studied; an iron based

and two manganese based driers. High spatial resolution NMR profiles and T_2 (spin-spin relaxation time) analysis as a function of depth and time are discussed. Simultaneously, the drying performance, hardness, and characteristics of the crosslinked film are evaluated.

2.2. Experimental section

2.2.1. Materials

The alkyd formulations were prepared by AkzoNobel Decorative Paints, Sassenheim, the Netherlands. Setal 270 SM-70 (obtained from Nuplex resins), a long oil alkyd resin based on soya-bean oil and commercially available aliphatic hydrocarbon solvent (Shellsol D40) were used in the formulations, which had a solid content of 55 wt. % based on the total composition. The curing was accelerated with the following commercially available driers; Nuodex Co 10 NEO (obtained from Huntsman Pigments, former Rockwood Pigments), Borch OXY-Coat (obtained from Borchers OM Group), DriCAT 2700F (obtained from Dura Chemicals) and Nuodex DryCoat (obtained from Huntsman Pigments). The abbreviations for each selected primary driers are given in Table 2.1.

Table 2.1. The abbreviations for selected primary driers.

Primary driers	Abbreviations
Nuodex Co 10 NEO	Co
Borch OXY-Coat	Fe
DriCAT 2700F	Mn1
Nuodex DryCoat	Mn2

Co drier (Nuodex Co 10 NEO) is a solution of cobalt carboxylate based on neodecanoic acids and contains 10 wt. (weight) % cobalt on the solution. Fe drier (Borch OXY-Coat) is a complex of iron dichloride hydrate and a bispidon ligand, that contains 0.09 wt. % iron in solution. Mn1 drier (DriCAT 2700F) is a complex of manganese and an unknown organic ligand, containing 0.1 wt. % manganese in solution. Mn2 drier (Nuodex DryCoat) is a complex of triazanone ligands and manganese carboxylates, consisting of 1 wt. % manganese in solution. The total amount of primary drier on solid content is 0.125 wt. %, 0.001 wt. %, 0.001 wt. % and 0.012 wt. %, for Co, Fe, Mn1 and Mn2, respectively. In addition, the coating compositions contain secondary driers; Nuodex Calcium 5 (Calcium carboxylate with 5 wt. % Ca on solution, obtained from Huntsman Pigments) and Durham Nuodex Zirconium 18 (Zirconium carboxylate with 18 wt. % Zr on solution obtained from Huntsman Pigments) and an anti-skinning agent, methylethylketoxime (2-butanone oxime, obtained as Exkin 2 from Huntsman Pigments). The anti-skinning agent was added 0.5 wt.

% on total composition. The total amount of secondary driers on dry alkyd resin is 0.25 wt. % and 0.90 wt. % for Ca and Zr, respectively.

2.2.2. Experimental methods

NMR imaging and relaxometry: Depth profiling and relaxation measurements were performed with a GARField ⁴⁶ NMR setup, consisting of an electromagnet with specially shaped pole tips, generating a magnetic field of 1.4 T with a gradient of 40 T/m perpendicular to the coating film. We used an Ostroff–Waugh pulse sequence to obtain the hydrogen density profiles and the signal decay, $\alpha_x^\circ - \tau - [\alpha_y^\circ - \tau - \text{echo} - \tau]_n$, wherein α is the flip angle and nominally equals to 90° . n is the number of echoes and equals to 512 in the experiments. The interecho time (2τ) used in the experiments equals $100 \mu\text{s}$ while the recording window to measure the echo has a duration of $90 \mu\text{s}$. The use of these parameters gives the best achievable spatial resolution of $6.5 \mu\text{m}$. The sample orientation is one of the resolution determining factors and is addressed by carefully aligning the sample. The acquisition of each profile took about 13 min, using a repetition time of 3 seconds and 128 signal averages.

The setup uses a surface coil for exciting the spins and measuring the signal. The sample is placed on top of the surface coil. The sensitivity profile of the coil is decreasing with an increase in distance above the coil. In order to correct for the decrease in the sensitivity over the film thickness, the measured signal profiles are divided by signal profile of a homogeneous reference sample allowing the local hydrogen density to be determined. As a reference sample, an aqueous 0.01 M CuSO_4 solution is used.

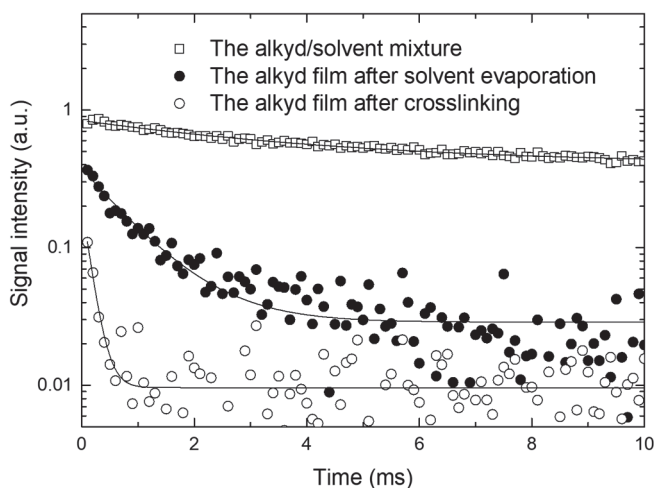


Figure 2.1. NMR signal decays of the alkyd (Setal 270 SM-70)/solvent(Shellsol D40) mixture, the alkyd film after solvent evaporation and after crosslinking. The solid lines represent the mono-exponential fit of each decay.

At every position in the sample, the recorded signal decay has a typical decay constant called T_2 , representing the spin-spin relaxation time^{15,18}. Species with a low molecular mobility, such as fully dried alkyd resins, have a short T_2 , while more mobile species, such as solvents of the paint, have a longer T_2 , as illustrated in Figure 2.1. To determine the local molecular mobility, signal decays at each position of the film were fitted by a single exponential function, $S_0 \exp(-n2\tau/T_2)$, wherein 2τ denotes the inter-echo time and n is the number of the acquired echo¹⁵. Although two T_2 values are observed during the solvent evaporation, belonging to solvent and the alkyd resin, a single exponential was selected with sufficient accuracy ($R^2=0.98$) in order to follow the changes in the mobility and easily compare between systems. During the solvent evaporation, the single T_2 value corresponds to the weighted average for solvent and alkyd resin. After the evaporation, a single T_2 describes the decrease of mobility as a result of crosslinking. All coatings were cast on a 140 μm thin glass slide of 18 x 18 mm with a theoretical wet thickness of 160 μm .

Film drying time: The drying time of our catalytic systems has been determined by BK (Beck Koller) drying recorder. The instrument is equipped with a hemispherical ended needle placed in the center of the freshly applied film of 90 μm wet layer thickness. The needle slowly moves over the coating film applied on a long glass plate during 24 hours. The test was performed at 23°C and 50% relative humidity. The trace left on the film during the drying has been used to measure the drying performance by defining 3 stages of drying. During the first stage (P1), the viscosity of the freshly applied alkyd film is low enough to permit the liquid to flow back. The viscosity of the drying film rises as the physical drying and autoxidation of the alkyd coating progress. In the second stage (P2), the flow back is not observed as a result of an increased viscosity, resulting in a continuous line pattern created by the needle. The network formation is followed in the third stage (P3), where the liquid-like film becomes harder. The resistance to penetration by the needle is much increased so that it gives intermittent penetration of the film surface. At the end of the third stage, the film is not punctured anymore.

Film hardness: The film hardness test has been done using a König type pendulum (BYK pendulum hardness tester). The number of oscillations needed to reduce from an initial deflection of 6° to a deflection of 3° was measured. More oscillations mean that the film is harder. The glass test plate (10 x 30 cm) was coated with a wet film thickness of 90 μm . The film hardness was measured during 14 days, which gives the dependence of film hardness versus time.

Time-resolved ATR-FTIR: The oxidation of alkyd resin was followed by time-resolved ATR-FTIR (Golden Gate, single reflection monolithic diamond) on Bruker Equinox 55 spectrophotometer (16 scans per spectrum, resolution of 4cm^{-1} , in the range of $4000\text{--}600\text{cm}^{-1}$, 2 spectra per hour, 24 hours monitoring). The film is applied over ATR crystal with an applicator giving 90 μm wet layer thickness. ATR-FTIR measures from the bottom side of

the coating. The integration is carried out for the following peaks relative to the height of the peak at 1465 cm^{-1} ; the *cis*-C=C-H (non-conjugated) stretching vibration at 3010 cm^{-1} , the *trans*-C=C-H (conjugated) wagging vibration at 980 cm^{-1} and OH stretching vibration between 3200 and 3600 cm^{-1} .

DMA: The DMA (Dynamic Mechanical Analysis) test was performed by TA Instruments RSA III model to determine the glass transition temperature (T_g) and crosslink density of the films. The measurements were carried out under the film-tension mode in an appropriate range of $-30/+250^\circ\text{C}$ (5°C stepwise) at a frequency of 1.66 Hz and an increasing strain amplitude from 0.03% to the value between $2.6\text{-}4\%$ depending on the sample. The tests were conducted using rectangular films specimen of $15.0 \times 6.0\text{ mm}$. Free-standing films were used, which they were prepared by applying the coating on polypropylene substrate with $90\text{ }\mu\text{m}$ wet layer thickness. The temperature corresponding to peak value of $\tan \delta$ vs temperature has been taken as the glass transition temperature. The overall dry film thickness was measured 35 to $50\text{ }\mu\text{m}$ after two weeks and five months drying.

2.3. Results and discussion

2.3.1. NMR profiles of drying alkyd films

In order to investigate the in-depth drying of alkyd films in the presence of cobalt alternatives, we first measured the coating with the cobalt based drier as a reference. In Figure 2.2, position-dependent hydrogen signal profiles of the coating with cobalt are shown. Two stages can be distinguished from the profiles. In the first stage the solvent evaporates, which takes approximately 1 hour.

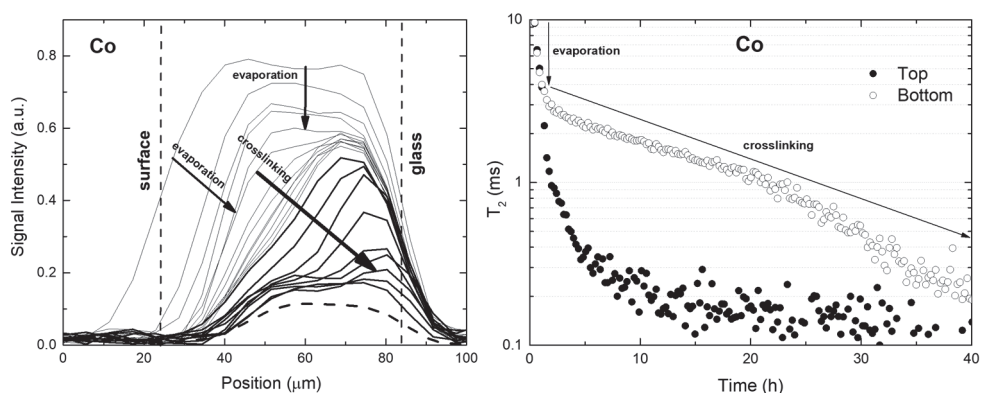


Figure 2.2. Left: The time-dependent NMR signal intensity profiles measured as a function of position inside the coating for the alkyd with Co drier (wet film thickness is $160\text{ }\mu\text{m}$). The air surface of the coating is on the left side and the glass substrate is located on the right side, as indicated in the figure. The first profile is measured directly after casting and the next profiles are measured every 13 minutes during first 3 h of drying. Between 3 h and 40 h, the profiles are given every 4 h (thicker lines). The final dashed profile is measured after 2 weeks of drying. Right: The time evolution of T_2 (in log scale) at the top (at $50\text{ }\mu\text{m}$) and the bottom (at $75\text{ }\mu\text{m}$) parts of the films.

In this stage the film shrinks due to loss of solvent. During the second stage, a front develops at the top of the film that moves towards the bottom of the coating. In previous works, it was shown that this front is a crosslinking front^{15,21,22,35,48–50,60}. It forms due to the hardening at the top, while the bottom part remains mobile. The signal in the top layer of the coating can no longer be detected due to the fast signal relaxation, which is a consequence of a strong decrease in the molecular mobility. Note that the thickness of the film stays constant during the crosslinking stage.

Besides the signal profiles, also the spin-spin relaxation time, T_2 , evolution during 40 hours of drying at the top and the bottom of the film with cobalt is shown in Figure 2.2. The analysis of T_2 in depth is a useful method to follow the crosslinking process, which plays the biggest role in restricting the molecular mobility of the polymer chains. Therefore, the lower T_2 value indicates a more crosslinked alkyd film^{15,21,22,35,46–50,60}. Again, two stages can be observed. In the first stage, wherein the solvent evaporates, the decrease in T_2 is very fast. Although two T_2 values are observed during the solvent evaporation, i.e. belonging to the solvent and the alkyd resin respectively, this period is also fitted with a single exponent ($R^2=0.98$) in order to follow the changes in mobility and compare between the different systems. Therefore, during the solvent evaporation, the single T_2 value corresponds to the weighted average for the solvent and the alkyd resin. In about one hour, the T_2 value drops from 10 ms to 4 ms with a similar rate at each depth of the film. In the second stage, the T_2 evolves differently at the top and the bottom of the film, indicating the differences in the in-depth drying process. Near the air surface (top), the T_2 value drops steeply from 4 ms to 1 ms in about half an hour, whereas it decreases from 1 ms to less than 0.4 ms slowly in the next three hours. This observation indicates the quick formation of the skin layer and its subsequent hardness development. After about 5 hours of drying, T_2 approaches a constant value around 0.2 ms, indicating the curing of the top of the film is almost complete. Beyond this point, it decreases slightly to a value of around 0.15 ms over the next 35 hours. On the other hand, the decrease in T_2 near the glass substrate (bottom) is much slower due to the front formation. There is a steeper decrease in T_2 after about 20 h, since the front reaches the bottom part. It takes almost 40 hours for T_2 to decrease to less than 0.2 ms, i.e. reaching a mobility identical to the top of the coating.

The influence of the catalyst type on the uniformity of crosslinking was also investigated with iron based and two manganese based driers. Position-dependent hydrogen signal profiles and the T_2 evolution at the top and the bottom of the films are shown in Figure 2.3. Regardless of the drier composition, more uniform crosslinking is observed with cobalt-free driers as compared to the cobalt based drier. While the film with Mn1 dries perfect homogeneously, there is some difference in the signal intensities at the top and the bottom of the films with Fe and Mn2.

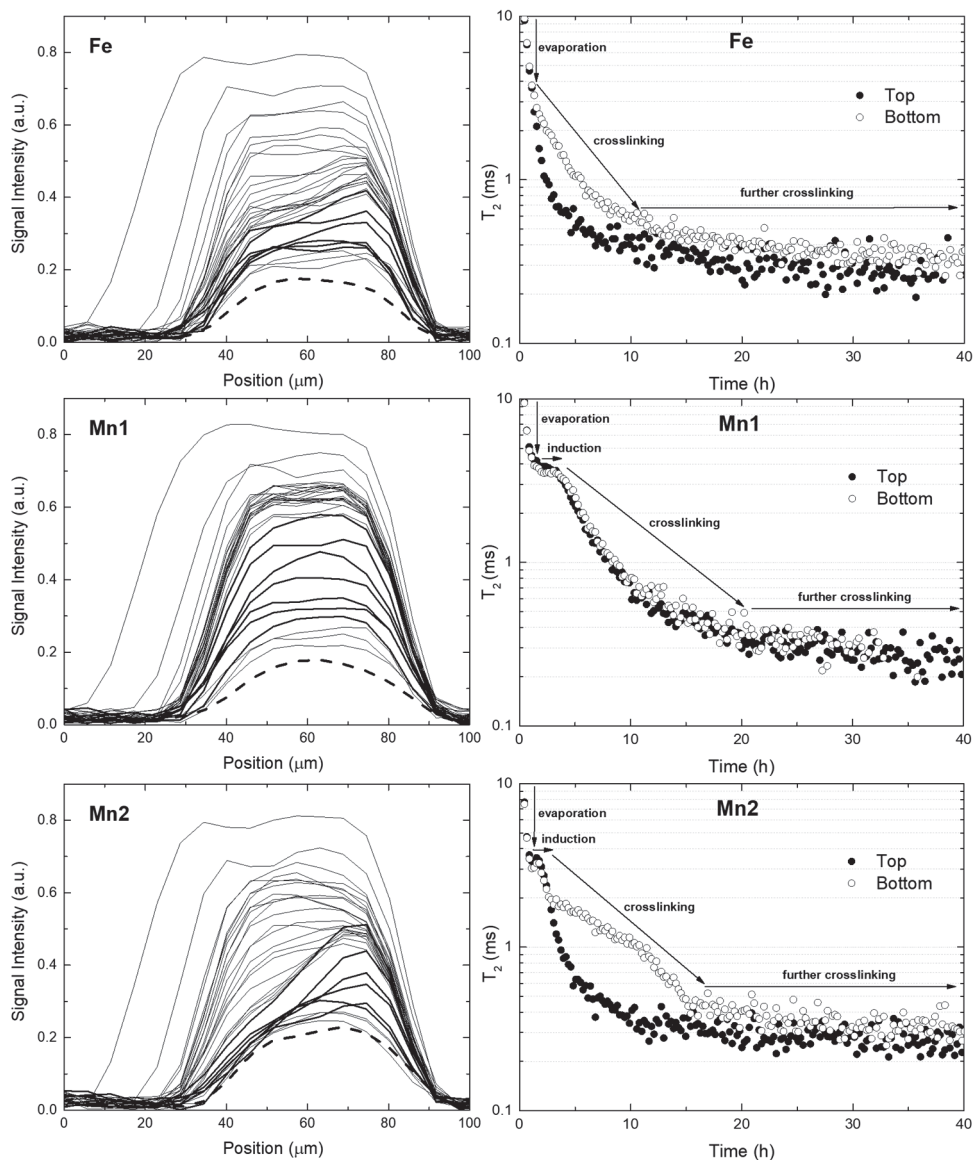


Figure 2.3. Left: The time-dependent NMR signal intensity profiles measured as a function of position inside the coating for the alkyds with Fe, Mn1 and Mn2 driers (wet film thickness is $160\ \mu\text{m}$). The air surface of the coating is on the left side and the glass substrate is located on the right side. The first profile is measured directly after casting and the next profiles are measured every 13 minutes during first 5 h of drying. The profiles are given every 2 h (thicker lines) between 5 h and 15 h and every 8 h between 15 to 40 h. The final dashed profiles are measured after 2 weeks of drying. Right: The time evolution of T_2 (in log scale) at the top (at $50\ \mu\text{m}$) and the bottom (at $75\ \mu\text{m}$) parts of the films.

For each drier composition, in about one hour of solvent evaporation, T_2 drops to about 4 ms at a similar rate at each μm depth of the film. After the evaporation stage, in the film with

Fe drier, T_2 continues to fall approximately at the same rate near the top, while the rate of decrease in T_2 is slower near the bottom. After about 5 hours of drying, T_2 approaches a constant value around 0.4 ms at the top, while being about 1 ms at the bottom, indicating the lower mobility of the top part compared to the bottom part. However, the mobility difference at the top and the bottom parts has disappeared after relatively short time that T_2 falls from 1 ms to about 0.5 ms at the bottom over the next 5 hours of drying. T_2 at both depths decreases slightly to a value of about 0.3 ms over the next 30 hours. In the film with Mn1, the rate of decrease in T_2 is uniform with depth during the time scale of the measurement, indicating its perfect homogeneously drying. After about 13 hours of drying, T_2 approaches a value of around 0.5 ms. Then, it decreases slightly to a value of about 0.25 ms over the next 27 hours. In the film with Mn2, it starts with uniform crosslinking over the first 3 hours of drying where T_2 drops from about 4 ms to 2 ms. Beyond this point, a gradient in T_2 develops. At the top part, T_2 continues to fall approximately at the same rate and approaches a value of around 0.5 ms after 5 hours of drying. On the other hand, at the bottom part, the rate of decrease in T_2 is slower and it reaches the value of around 0.5 ms after the next 10 hours of drying. During this period, the top part of the film has acted as a kind of skin layer, resulting the difference in the in-depth drying process. However, the formation and the acting duration of the skin layer is not much pronounced compared to the drying with Co. T_2 at both depths decreases slightly to a value of about 0.3 ms over the next 25 hours. Note that the final T_2 values of these alternatives (around 0.3 ms) is twice as high than the T_2 value of cobalt (0.15 ms) after 40 hours drying. The relaxation times after two weeks of drying were summarized in Table 2.2.

Table 2.2. The relaxation times after two weeks of drying.

	T_2 (ms)	
	Top	Bottom
Co	0.14 ± 0.01	0.14 ± 0.01
Fe	0.26 ± 0.01	0.30 ± 0.01
Mn1	0.26 ± 0.01	0.24 ± 0.01
Mn2	0.28 ± 0.01	0.34 ± 0.01

There is difference between the initial drying of the films with Mn-based driers (Mn1 and Mn2) and with the Fe drier. In both Mn-based systems, an induction period after the solvent evaporation stage is observed, where both the NMR profiles and T_2 stay constant for some time (Figure 2.3). The induction period for Mn1 is around 2 hours while it is about 1 hour for Mn2. The induction time is a measure for the ability of the drier to initiate the hydroperoxide formation/decomposition reactions leading to crosslinking^{12,15,20}. An induction period for different Mn-based driers during the crosslinking of ethyl linoleate (EL)

in bulk state was also observed by Bouwman *et al*¹² using time-resolved FTIR. They showed the relation between the duration of the induction period and the oxidation state of manganese. The induction period of different manganese based driers, which we observed for real alkyd films, is attributed to the dynamics of the drier itself rather than the transport processes in the alkyd system.

2.3.2. Measuring the drying time, i.e. the formation of film spanning networks

The drying performance of the driers has been determined by a Beck-Koller (BK) drying test, which indicates the formation of a film spanning network. The BK test essentially probes the viscosity build-up during the oxidative drying of the film. The physical parameters obtained by this test are used complementary to NMR profiling to assist in the interpretation of the film formation process. BK drying test relies on the patterns created by the needle, moving through the applied film during the drying process. The various drying stages can be identified from typical patterns as explained in the methods section. The film in the beginning of P3 stage is considered as surface-dry, where the surface of the film has crosslinked sufficiently to form a skin layer¹⁵. At the end of P3 phase, the alkyd film is considered as through-dry, meaning that there is a complete film spanning network giving the film elastic properties. Note that the film may require more time than through-dry time for further crosslinking.

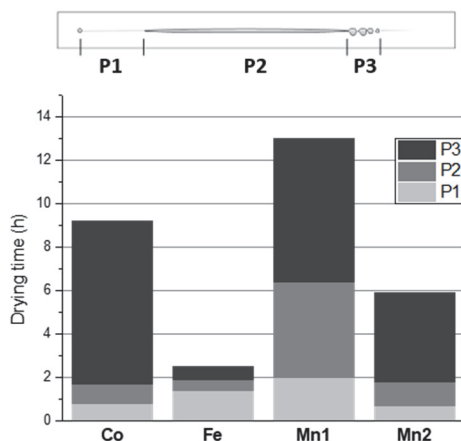


Figure 2.4. BK drying times of coatings (wet film thickness of 90 μm) with Co, Fe, Mn1, and Mn2. P1: Flow back (evaporation), P2: Continuous track, P3: Interrupted track (surface dry), after P3: no trace (through dry).

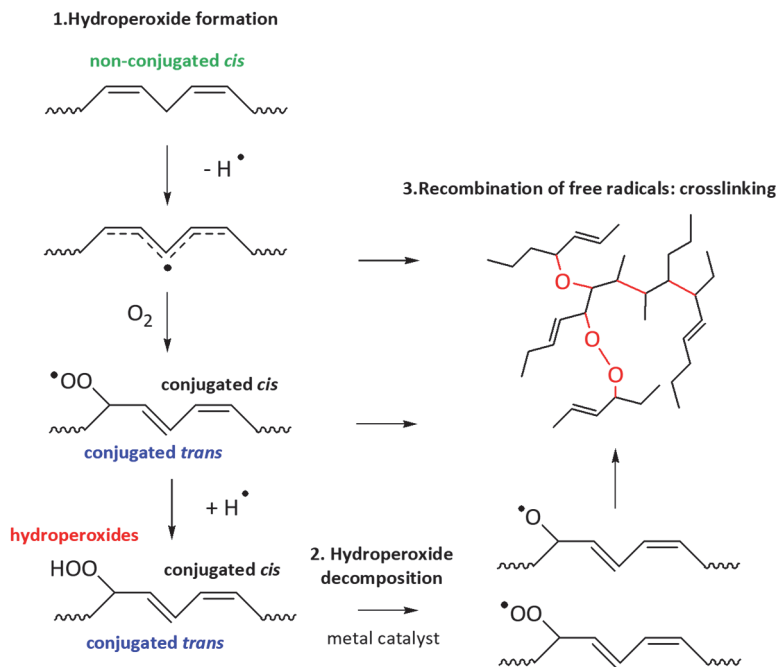
For the alkyds with Co, Fe, Mn1 and Mn2 driers, BK drying times are shown in Figure 2.4. Fe and Mn2 driers give surface-dry film within 2 hours, which is comparable to Co (2 h), while Mn1 has the longest surface-dry time of 6 hours. Fe drier has the shortest through-dry time (2 h), followed by Mn2 (6 h), Co (9 h) and Mn1 (13 h). Based on these results, we can only compare the speed of formation of a film spanning network. It does not give any

explanation for these differences. Actually, BK drying test is not a good measure for the crosslink density, since a film spanning network can be quickly formed even with low crosslink density.

The differences between the results of the BK test and the NMR profiling are considered for further interpretation of the film formation process. In NMR profiling, the through-dry time represents the intersection of the time when the gradient in T_2 at the top and the bottom of the film disappears and the beginning of the observed constant T_2 value at all depths of the film. The full comparison of through-dry time found by NMR and BK drying test is difficult since the wet film thickness for BK drying test is less than the films used for NMR profiling (90 μm versus 160 μm). As discussed before, different degrees of non-uniform crosslinking are observed in case of Co, Fe and Mn2 driers, which depends on the balance between the intrinsic rate of the reactions and the necessary transport process that makes the drying pattern dependent on the film thickness. Moreover, thicker films take longer time for solvent evaporation. Instead of direct comparison of the actual through-dry times, it is reasonable to compare the order found by NMR and BK drying measurement. Fe drier has the shortest BK through-dry time (2.5 h), followed by Mn2 (6 h), Co (9 h) and Mn1 (13 h) (Figure 2.4). The shortest through-dry time found by T_2 analysis is also observed for Fe drier (11 h) due to homogeneous drying, whereas the longest one is observed for Co (40 h) due to front drying (Figure 2.2 and Figure 2.3). The slow drying of Mn1 (20 h) and Mn2 (16 h) driers can be linked to the presence of induction period. It is clearly visible that the film with Fe drier is much faster in forming a film spanning polymer network than films with other drier compositions. However, the judgement on the drying performance of Mn1, Mn2 and Co driers can only be done by considering the thickness of the film. For thinner films (wet thickness of 90 μm) used for BK drying test, the film spanning network formation speed tends to be in the decreasing order of Fe, Mn2, Co and Mn1. For thicker films (wet thickness of 160 μm) used for NMR profiling, it tends to be in the decreasing order of Fe, Mn2, Mn1 and Co.

2.3.3. Time evolution of chemical changes during drying

Time-resolved ATR-FTIR spectroscopy was used to monitor the chemical drying of alkyd coatings with the considered different driers. Simplified schematic representation of the oxidative drying of an alkyd coating is given in Scheme 2.1. In a freshly applied film, there are non-conjugated *cis* double bonds on the fatty acid backbone of the alkyd coating. After the solvent evaporation (physical drying), a hydrogen atom is abstracted from the bis-allylic CH_2 group between $\text{C}=\text{C}$ double bonds. Hydroperoxides are formed after the reaction of the resulting radical with dioxygen and the rearrangement of the double bonds. The hydroperoxide decomposition into alkoxy and peroxy radicals by metal catalysts results in active crosslinking sites. As crosslinking proceeds by the recombination of the free radicals, a three-dimensional network is formed that leads to a hard film ^{1,2,8,11,12,16,17,61}.



Scheme 2.1. Simplified schematic representation of the oxidative drying of an alkyd coating ^{1,2,8,11,12,16,17}.

FTIR spectra of the alkyd coating with Mn1 is given in Figure 2.5. Different band assignments belonging to different chemical groups or bonds allow to follow the curing reactions ^{11,25,61,62}.

As it is shown in Figure 2.5, the oxidative drying of the alkyd coating can be followed by the disappearance of the non-conjugated *cis*-C=C-H (3010 cm^{-1}) and the appearance of the conjugated *trans*-C=C-H (980 cm^{-1}) in time and the hydroperoxide formation (-OH band between 3200 and 3600 cm^{-1}) ^{31,63}. For each spectrum, the integration is carried out for the peak area of non-conjugated *cis* and conjugated *trans* C=C double bonds and OH containing compounds, which is shown in Figure 2.6. In all systems, a significant decrease of the intensity of the non-conjugated *cis*-C=C-H is accompanied by an increase of the intensities of conjugated *trans*-C=C-H and OH-band.

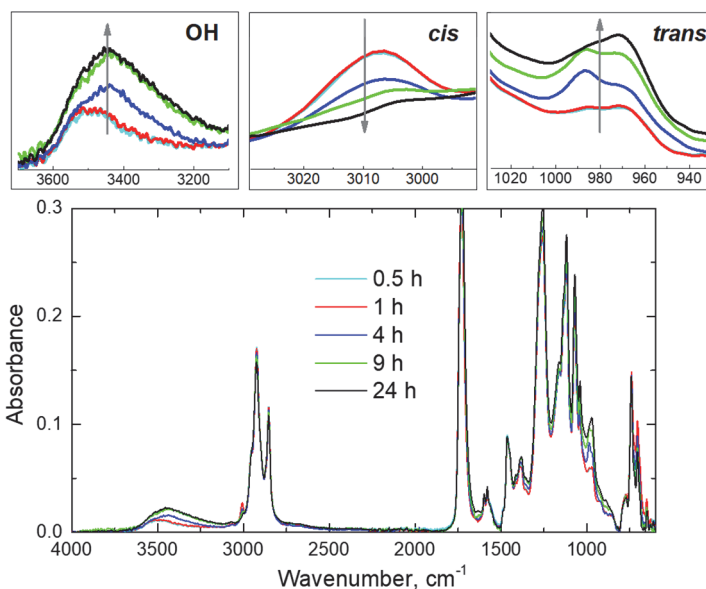


Figure 2.5. The time evolution of FTIR spectra of the alkyd coating with Mn1 drier.

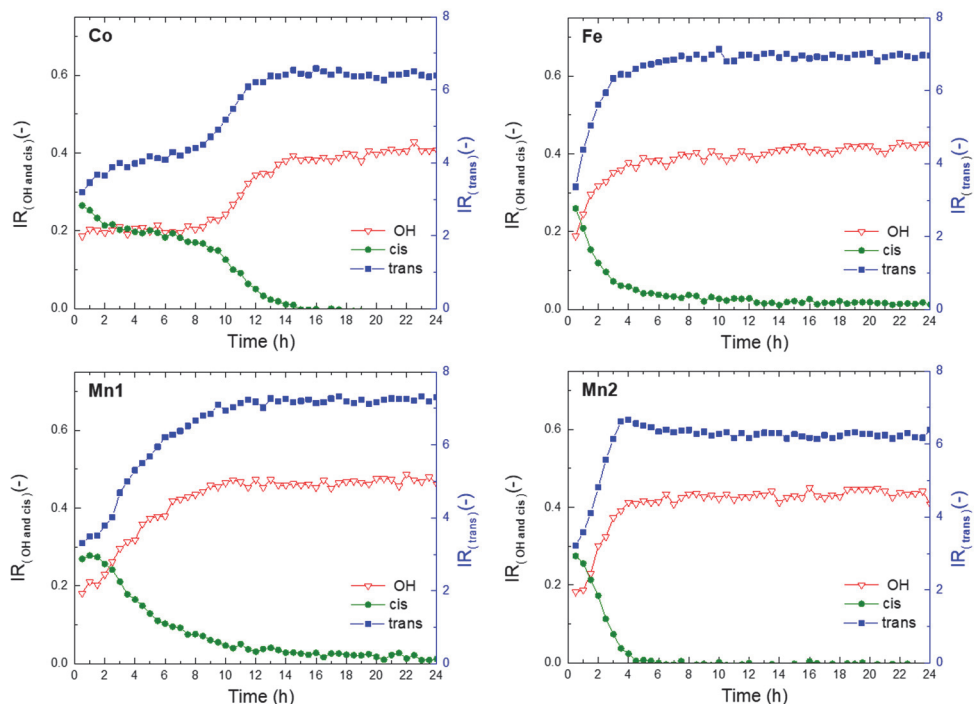


Figure 2.6. Time dependent integral plots of IR bands for the non-conjugated *cis*-C=C-H stretching vibration, the conjugated *trans*-C=C-H wagging vibration and OH stretching of hydroxyl-containing species (alcohol, hydroperoxide, etc.).

The influence of the driers on the alkyd drying was checked by monitoring the changes in the intensity of the non-conjugated *cis*-C=C-H stretching vibration at 3010 cm^{-1} ^{12,13}. In the presence of Co, the intensity of the peak at 3010 cm^{-1} (*cis*) does not significantly change in the first 10 hours. After 10 hours, a sudden change occurs. This observation can be explained by the front formation during drying of the film with Co. Since ATR-FTIR measures the bottom of the sample, the FTIR spectrum is constant until the moment that the front reaches the bottom, which takes about 10 hours for this specific system. The disappearance of non-conjugated *cis* is complete after about 14 hours in the presence of Co, representing the bottom of the coating only. In the presence of other driers (Fe, Mn1 and Mn2), the disappearance of the non-conjugated *cis* is faster. The drying is considered homogeneous for these systems, especially for thinner films (wet thickness of $90\text{ }\mu\text{m}$), so the bottom of the film measured by FT-IR can be regarded representative for the overall drying of the film. The decrease in the intensity of non-conjugated *cis* started immediately after the application in the presence of Fe drier. An induction time of about 2 h is observed for Mn1, during which the intensities of the non-conjugated *cis*, conjugated *trans*-C=C-H and OH-band remain unchanged. The induction time is a period wherein no observable chemical reaction occurs. An induction time is not visible for Mn2 when the intensity of the non-conjugated *cis* is monitored, but the constant OH-band in the beginning of drying for about 1 h can be considered as an induction time. These induction times are comparable with the ones found in NMR measurements. The disappearance of non-conjugated *cis*-C=C-H is complete after about 5 h for Fe, 11 h for Mn1 and 4 h for Mn2 and the final intensity of OH-band is almost same for all the systems. However, this does not imply that the density of crosslinking is the same for all systems. Beside the crosslinking reactions, the alkoxy radicals may generate by-products, such as aldehydes, ketones, epoxides, and carboxylic acids^{6,7,16-19,8-15}. The amount of these by-products varies in the presence of different catalysts. The quantification of the by-products is out of scope of this study.

2.3.4. Glass transition temperatures and crosslink densities of dried films

The influence of different driers on the final alkyd film is also studied by correlating the crosslinked network structure of the films with the resulting mechanical properties. Here, Dynamic Mechanical Analysis (DMA) was carried out to determine the glass transition temperature T_g (max in $\tan \delta$) and crosslink density of the films. Note that the overall T_g and crosslink density of the entire coating film are measured by DMA which gives the average T_g and crosslink density of the entire film. Figure 2.7 compares the T_g values of the coatings with Co, Fe, Mn1 and Mn2 driers after curing for either two weeks or five months. After 2 weeks, the film with Co has the highest T_g at $38 \pm 1\text{ }^\circ\text{C}$, while the others have nearly the same T_g around $30 \pm 2\text{ }^\circ\text{C}$. After a period of 5 months, all coatings show an increase in T_g . However, the film with Co shows the biggest increase from $38\text{ }^\circ\text{C}$ to $48\text{ }^\circ\text{C}$. For the others, the five months T_g values do not significantly differ from the two weeks T_g values.

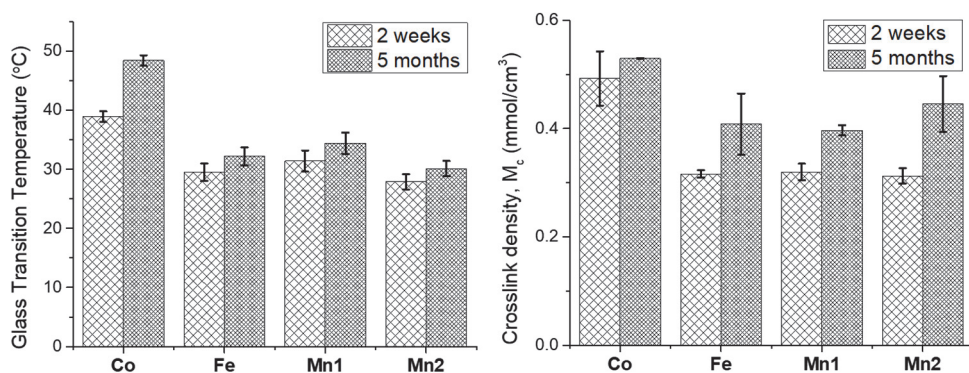


Figure 2.7. Glass transition temperatures (T_g) (left) and crosslink densities (right) of coatings as obtained from DMA.

Figure 2.7 compares the crosslink densities after crosslinking of the films in a 2 weeks and 5 months period, showing the same trend as with the T_g values. After 2 weeks drying, the film with Co has the highest crosslink density of 0.49 mmol/cm³ while all others have a value around 0.32 mmol/cm³. Contrary to the extent of variations in T_g results, further drying over a period of 5 months results in a considerable increase in the crosslink densities for Fe, Mn1 and Mn2 driers to values of 0.41, 0.40 and 0.45 mmol/cm³, respectively. Although these films crosslinked sufficiently to produce relatively harder films, the crosslinking and hardness development continue during a longer period of drying. On the other hand, the crosslink density of the film with Co has increased to 0.53 mmol/cm³ after 5 months, consequently representing the most densely crosslinked film.

In order to correlate DMA results to NMR relaxation analysis, Figure 2.8 is plotted, comparing the inverse T_2 and T_g for 2 weeks dried films. Additionally, the link between these two values and König hardness development is also illustrated in Figure 2.8. As T_g shifts to higher value as a result of crosslinking⁶⁴, the highest T_g stands for the most densely crosslinked network of the studied films with various driers. On the other hand, the lowest T_2 (the highest inverse T_2) stands for the most densely crosslinked film since crosslinking limits the mobility of the chains. Moreover, crosslinking produces harder films. In the König test, the more oscillations are observed, the harder the film is. Therefore, the hardest film should have the highest T_g and lowest T_2 (the highest inverse T_2) which is clearly shown in Figure 2.8, summarizing the results of 2 weeks drying. Keeping in mind that we are looking at systems with the same alkyd binder allowing us to correlate the higher T_g to more crosslinked and harder coating. The film with Co is the hardest followed by the films with Mn1, Fe and Mn2 in the order of decreasing in hardness. Note the increase in the crosslink densities after a longer period of drying for Mn1, Fe and Mn2 driers in which Mn2 has a relatively bigger increase (Figure 2.7). While the film with Mn2 has the lowest hardness after

2 weeks drying, further drying may produce higher or equal hardness compared to the films with Fe and Mn1.

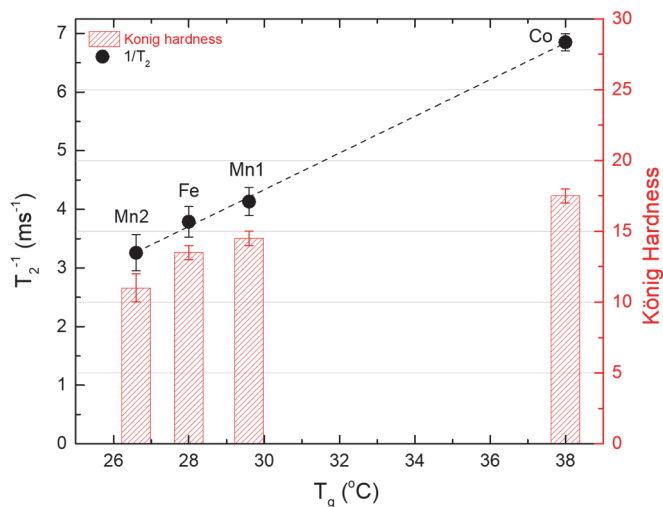


Figure 2.8. The relation between the inverse T_2 measured with NMR, T_g measured with DMA and hardness with König method for two weeks dried samples.

2.3.5. A conceptual model for drying process

To compare the effect of different driers on the oxidative drying pattern in alkyd coatings and the final film properties, we develop a conceptual model of film drying based on all observations discussed until now. The difference in drying patterns is attributed to a concentration gradient in molecular oxygen in depth of the film^{15,21,22,35,48–50,60}. The differences in the oxidative drying of the alkyd films are explained by two models, which are schematically shown in Figure 2.9. They are referred to as front-forming and homogeneous drying.

The film starts to crosslink after the hydroperoxide formation/decomposition steps, which requires oxygen to proceed^{12,15,16}. In case these steps are faster near the surface, a skin layer¹⁵ grows at the top of the film. This situation is defined as front-forming drying, since the skin layer acts as a front and moves towards the bottom of the film. The skin layer is densely crosslinked and limits the oxygen penetration into deeper layers that results in a gradient in crosslink density. As the front moves towards the bottom of the film, the top skin layer becomes thicker as a result of crosslinking with the available alkyd chains in the bottom viscous liquid. Because of the barrier effect of this densely crosslinked layer for oxygen diffusion, the drying of the bottom part is slower. However, the complete film hardening is achieved by this stepwise crosslinking from the top to the bottom of the film, resulting in a highly crosslinked hard film.

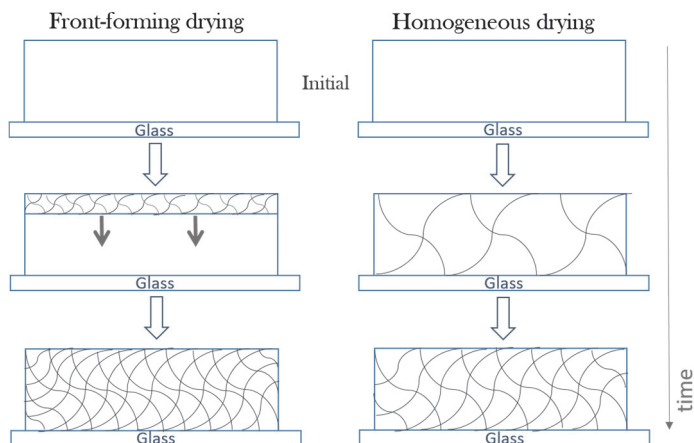


Figure 2.9. A conceptual model for different types of oxidative drying, i.e. front-forming and homogeneous drying.

The balance between the speed of reaction and oxygen diffusion determines the dominating type of drying. In case of homogeneous drying, oxygen diffusion is fast relative to the reactions, causing hydroperoxide formation/decomposition and crosslinks to occur uniformly throughout the film. As a result of uniform crosslinking, the film hardening will be hindered. However, the long-term drying promotes further crosslinking and hardness development, but still exhibits lower values compared to front-forming drying.

With the help of the model, an educated guess on some certain properties, such as the drying rate, the overall and depth-resolved crosslink density and the hardness development, can be made on the basis of the drying pattern of the specific drier composition.

2.4. Conclusion

We achieved to represent different oxidative drying patterns for cobalt-, manganese- and iron-based driers. During the drying in the presence of cobalt, a highly crosslinked skin layer is formed that acts as a front and moves towards the bottom of the film. Cobalt-free driers exhibit more uniform, i.e. homogeneous, crosslinking throughout the film. Compared to homogeneous drying by cobalt-free driers, cobalt gives a lower overall drying rate and significantly higher final crosslink density and hardness development. NMR data and BK drying tests show that the iron-based drier has the highest drying rate, whereas manganese-based driers have an induction period that prolongs the drying time. The induction time is a period wherein no observable chemical reaction occurs. Although the drying rates of cobalt-free driers are significantly different, the final crosslink density and the hardness development are almost similar.

The outcome of this study provides an overall update for the paint industry and the ongoing research of cobalt alternatives. For further optimization of cobalt alternatives, the focus of the research should be on understanding the influence of the driers on drying pattern of the film and the role of induction period on the drying rate. Front drying works best to obtain densely crosslinked hard films. For a fast drying film with a reasonable crosslink density and hardness, a drier promoting homogeneous drying without an induction period should be preferred.

Chapter 3

The influence of calcium and zirconium based secondary driers on drying solvent borne alkyd coatings

Cobalt based driers are the most commonly used primary catalysts in alkyd coatings as they promote fast drying and lead to hard coatings. However, several studies have suggested potential reclassification of cobalt-based alkyd driers. Therefore, cobalt based driers are being replaced by alternatives, e.g. based on iron or manganese. In practice primary driers (Co, Mn, or Fe) are used in combination with secondary driers (e.g. Ca, Zr) to enhance drying of the film. Coating formulators aim for a high drying speed and hardness development. However, each combination of primary and secondary driers leads to a different oxidative drying pattern resulting in variations in the crosslink density and hardness development. In this study we have systematically investigated the effect of two secondary driers, Calcium (Ca) and Zirconium (Zr), on curing behavior when added to different primary driers (Co, Mn, and Fe) using a high spatial resolution NMR set-up. As expected, we observed increased drying speed and higher crosslink densities when adding these secondary driers. While calcium showed to promote the front speed, zirconium showed to increase the measured crosslink density. The behavior seems to be generic as this was seen for all three the primary driers.

This chapter has been published as

Ö. Gezici-Koç *et al.*, *Polymer* 121: 262-273 (2017).

3. The influence of calcium and zirconium based secondary driers on drying solvent borne alkyd coatings

3.1. Introduction

Alkyd based paints are widely used as air drying coatings. For a large part alkyd coatings can be made via renewable resources and the market share of waterborne alkyds is increasing⁶⁵. Coatings typically have very small amount of additives, which have very specific purposes, such as driers, thickening agents, anti-skinning agents, surface-active agents, surface modifiers, fillers, etc., and are typically added to the coatings in very small amounts. Although in small amounts, additives have a considerable influence on the final properties of the coatings. The natural drying time of alkyd resins is of the scale of months, this is why catalysts, or so-called driers, are added. Generally, these driers are transition metals forming a complex with organic ligands. Cobalt based driers are the most commonly used. However, several environmental studies have suggested potential reclassification of cobalt-based alkyd driers^{66,67}. Therefore, cobalt based driers are being replaced by alternatives, such as manganese (Mn)^{68–76} or iron (Fe)^{77–85} based driers.

Recently, we have published research on the curing process of alkyd coatings with alternatives for cobalt⁸⁶. Note that, with “curing” is meant the chemical crosslinking process. The curing only starts after the physical film formation process is completed and the solvent initially present has evaporated. The chemical curing of alkyd resin consists of four main steps^{72,75,87–91}. These steps include (1) the inhibition (induction) period, (2) hydroperoxide formation, (3) hydroperoxide decomposition, and (4) crosslinking. The inhibition (induction) period is the period during which the curing is not progressing, but hydroperoxide formation is initiated^{72,75,87,92}.

In the past, the drying of cobalt was characterized carefully, which in most cases shows a curing process with a front moving from top to bottom. In fact, for front-like drying it has been shown that oxygen transport is the dominating process⁹³. While a sharp drying front was observed for cobalt based catalyst, more homogeneous drying was observed for manganese based catalysts. The differences can be explained by the changes in the reaction rate and oxygen diffusion constant^{68,69}. In fact in a more recent study, the studied alternatives for cobalt generally show a more homogeneous drying and a lower crosslink density as measured with DMA⁸⁶.

Driers used for alkyd curing are commonly divided into two main classes: primary and secondary driers. Primary driers promote oxygen uptake, hydroperoxide formation and decomposition processes⁹⁴. The secondary driers are said to enhance the drying of the film. Secondary driers are sub-classified as through driers (e.g., zirconium, strontium, aluminum) and as auxiliary driers (e.g., calcium, potassium, lithium)⁹⁴. Zr and Ca are the most widely used ones in combination with primary driers^{86,87,94}. In comparison to other through driers,

Zr driers have superior properties in terms of color, yellowing and stability. Ca driers are said to improve hardness and gloss and to reduce skin-formation⁹⁴. Many statements are made on the working mechanisms of secondary driers, ranging from promotion of oxygen transport, formation of physical links in the network, and keeping the primary driers active^{32,87,95}. However, the working mechanism in combination with the cobalt alternatives (and even for cobalt) has many open questions⁹⁶. Consequently, the aim of this study is to identify the role of secondary driers and to investigate if this role depends on the choice of the primary drier.

Many techniques allow for the investigation of the working mechanisms of driers for alkyd curing. However, most of them do not allow measurements as a function of depth. For instance Time resolved Attenuated Total Reflectance Fourier Transform Infrared (ATR-FTIR) spectroscopy allows chemical profiling, but mainly from the substrate side of the alkyd film^{74,75}. Fortunately, Confocal Raman Microscopy (CRM) and Nuclear Magnetic Resonance (NMR) have shown to be able to measure in a spatially resolved manner. CRM may be used for chemical profiling by following the disappearance of double bonds⁹⁷⁻⁹⁹. High spatial resolution NMR profiling proved to be an appropriate noninvasive technique to study crosslinking of alkyd films^{68,69,87,92,93,99-103}.

In this study, we investigate the influence of the presence of secondary driers, based on Calcium (Ca) and Zirconium (Zr), on the oxidative drying of alkyd coating films using manganese and iron based alternatives, next to cobalt as a reference. To follow the curing process, NMR profiling is employed. The fully cured films are then characterized with Dynamic Mechanical Analysis (DMA). This allows us to relate the NMR results to the crosslinked network structure of the coating layers to the final mechanical properties¹⁰⁴. Our approach is to investigate the drying profiles, characterization of front-speeds, inhibition periods, and final cross-link densities to unravel the influence of the secondary driers.

3.2. Experimental section

3.2.1. Materials and coating preparation

The alkyd formulations were prepared by AkzoNobel Decorative Paints, Sassenheim, the Netherlands. The coatings are prepared by mixing, in order of, the alkyd resin, the anti-skinning agent, the solutions of primary and secondary driers, and solvent. Setal 270 SM-70 (obtained from Allnex resins), a long oil alkyd resin based on soya-bean oil and commercially available aliphatic hydrocarbon solvent (Shellsol D40) were used in the formulations, which had a solid content of 55 wt. % based on the total composition. The curing was accelerated with the following commercially available driers; Nuodex Co 10 NEO (obtained from Huntsman Pigments, former Rockwood Pigments), Borchhi OXY-Coat (obtained from Borchers OM Group), DriCAT 2700F (obtained from Dura Chemicals) and

Nuodex DryCoat (obtained from Huntsman Pigments) as primary driers; Nuodex Calcium 5 (obtained from Huntsman Pigments) and Durham Nuodex Zirconium 18 (obtained from Huntsman Pigments) as secondary driers. The abbreviations and concentration for each selected primary and secondary driers are given in Table 3.1.

Table 3.1. The abbreviations for selected primary driers and secondary driers, including the concentrations (wt. % on solid content) in coating samples.

		Coating samples (metal content in wt. % on solid content)															
Drier	Name	Co	Co Ca	Co Zr	Co Ca/Zr	Fe	Fe Ca	Fe Zr	Fe Ca/Zr	Mn1	Mn1 Ca	Mn1 Zr	Mn1 Ca/Zr	Mn2	Mn2 Ca	Mn2 Zr	Mn2 Ca/Zr
Nuodex Co 10 NEO	Co	0.12	0.12	0.12	0.12												
Borchi OXY- Coat	Fe					0.001	0.001	0.001	0.001								
DriCAT 2700F	Mn1									0.001	0.001	0.001	0.001				
Nuodex DryCoat	Mn2													0.012	0.012	0.012	0.012
Nuodex Calcium 5	Ca		0.25		0.25		0.25		0.25		0.25		0.25		0.25		0.25
Durham Nuodex Zirconium 18	Zr			0.9	0.9			0.9	0.9			0.9	0.9			0.9	0.9

Co drier (Nuodex Co 10 NEO) is a solution of cobalt carboxylate based on neodecanoic acids and contains 10 wt. (weight) % cobalt on the solution. Fe drier (Borchi OXY-Coat) is a complex of iron dichloride hydrate and a bispidon ligand that contains 0.09 wt. % iron in solution. Mn1 drier (DriCAT 2700F) is a complex of manganese and an unknown organic ligand, containing 0.1 wt. % manganese in solution. Mn2 drier (Nuodex DryCoat) is a complex of triazanonane ligands and manganese carboxylates, containing 1 wt. % manganese in solution. Ca (Nuodex Calcium 5) is calcium carboxylate with 5 wt. % Ca on solution and Zr (Durham Nuodex Zirconium 18) is zirconium carboxylate with 18 wt. % Zr on solution. In addition, all coating compositions contain an anti-skinning agent, methylethylketoxime (2-butanone oxime, obtained as Exkin 2 from Huntsman Pigments). The anti-skinning agent was added 0.5 wt. % on total composition.

3.2.2. Experimental methods

3.2.2.1. NMR imaging and relaxometry

Depth profiling and relaxation measurements were performed with a GARField¹⁰⁰ NMR setup, consisting of an electromagnet with specially shaped pole tips, generating a magnetic field of 1.4 T with a gradient of 40 T/m perpendicular to the coating film. We used an Ostroff–Waugh pulse sequence to obtain the hydrogen density profiles and the signal decay, $\alpha_x^\circ - \tau - [\alpha_y^\circ - \tau - \text{echo} - \tau]_n$, wherein α is the flip angle and nominally equals to 90°. *n*

is the number of echoes and equals to 512 in the experiments. The interecho time (2τ) used in the experiments equals 100 μs while the recording window to measure the echo has a duration of 90 μs . The use of these parameters gives the best achievable spatial resolution of 6.5 μm . The sample orientation is one of the resolution determining factors and is addressed by carefully aligning the sample. The acquisition of each profile took about 13 min, using a repetition time of 3 seconds and 128 signal averages.

The setup uses a surface coil of a diameter of 5 mm to excite the spins and measuring the signal. The sample is placed on top of the surface coil. The sensitivity profile of the coil is decreasing with an increase in distance above the coil. In order to correct for the decrease in the sensitivity over the film thickness, the measured signal profiles are divided by signal profile of a homogeneous reference sample allowing the local hydrogen density to be determined. As a reference sample, an aqueous 0.01 M CuSO_4 solution is used.

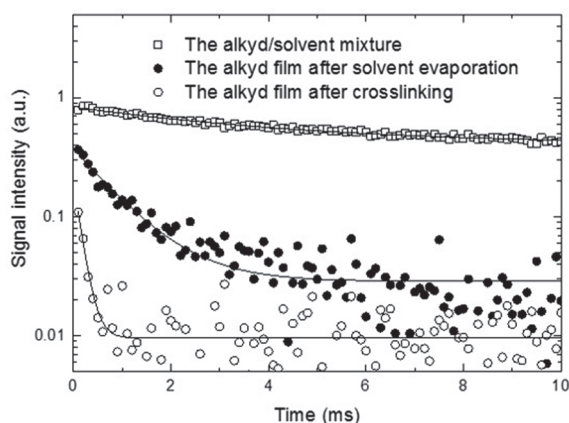


Figure 3.1. NMR signal decays of the alkyd (Setal 270 SM-70)/solvent (Shellsol D40) mixture, the alkyd film after solvent evaporation and after crosslinking. The solid lines represent the mono-exponential fit of each decay.

At every position in the sample, the recorded signal decay has a typical decay constant called T_2 , representing the spin-spin relaxation time^{87,90}. Species with a low molecular mobility, such as fully dried alkyd resins, have a short T_2 , while more mobile species, such as solvents of the paint, have a longer T_2 , as illustrated in Figure 3.1. To determine the local molecular mobility, signal decays at each position of the film were fitted by a single exponential function, $S_0 \exp(-n2\tau/T_2)$, wherein 2τ denotes the inter-echo time and n is the number of the acquired echo⁸⁷. Although two T_2 values are observed during the solvent evaporation, belonging to solvent and the alkyd resin, a single exponential was selected to fit with sufficient accuracy ($R^2=0.98$). During the solvent evaporation, the single T_2 value corresponds to the weighted average for solvent and alkyd resin. After the evaporation, a

single T_2 describes the decrease of mobility as a result of crosslinking. This is the most interesting for our drying studies in this work.

All coatings were cast on a 140 μm thin glass slide of 18 x 18 mm with a wet thickness of 260 μm .

3.2.2.2. DMA

The DMA (Dynamic Mechanical Analysis) test was performed by TA Instruments RSA III model to determine the glass transition temperature (T_g) and crosslink density of the films. The measurements were carried out under the film-tension mode in an appropriate range of -30 to +250 $^{\circ}\text{C}$ (5 $^{\circ}\text{C}$ stepwise) at a frequency of 1.66 Hz and an increasing strain amplitude from 0.03% to the value between 2.6-4% depending on the sample. The tests were conducted using rectangular films specimen of 15.0 x 6.0 mm. Free-standing films were prepared by applying the coating on polypropylene substrate with 90 μm wet layer thickness. The $\tan \delta$ curves obtained from DMA measurements are plotted in Figure 3.2b, in which the temperature corresponding to the peak value of $\tan \delta$ vs temperature has been taken as the glass transition temperature. The crosslink density was evaluated using DMA. The storage modulus E' as a function of temperature is presented in Figure 3.2a. The relation between modulus E' and M_c (the molecular weight between two crosslinks) was given by Wu et al.¹⁰⁵ that M_c can be represented by the following equation:

$$M_c = 3\rho RT/E', \quad (3.1)$$

where ρ is the polymer density (1.1 g/cm^3 is used for all samples in this study), R is the gas constant, and T is the absolute temperature taken at the point with the lowest E' in the rubbery plateau. The lowest E' value above T_g was used to calculate the crosslink density.

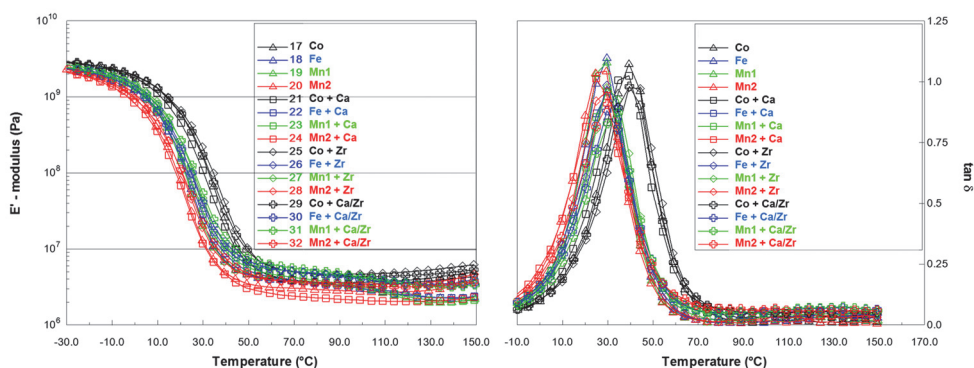


Figure 3.2. a) E' (storage modulus) curves and b) the $\tan \delta$ curves of coating samples as a function temperature as measured by DMA.

The overall dry film thickness was measured to be 35 to 50 μm after two weeks drying, just before the DMA measurements.

3.3. Results and Discussion

The main aim of the research is to investigate the effect of two secondary driers, Calcium and Zirconium, in the presence of the primary driers. The main questions are: What is the role of each secondary drier in combination with different primary driers. Do these secondary driers behave the same for all primary driers? In previous work, we have shown that secondary driers in combination with cobalt influence the front speed¹⁰³. In this study, we wish to investigate front speeds for different primary and secondary drier combinations. Firstly, we show NMR profiles of drying alkyd coatings to illustrate the different drying behaviors. In a next step, the front speeds are analyzed to investigate the effects of the secondary driers. During the analysis of the profiles, inhibition periods were observed. The effect of the secondary driers on the inhibition period was studied. The crosslink density was also determined using DMA on fully crosslinked films. In the last section, the different results were combined to gain a clear insight in the effect of the secondary driers.

3.3.1. NMR profiles of drying alkyd coatings

In order to investigate the in-depth drying of alkyd films, we first measured the coating with the cobalt based drier with and without secondary driers as a reference. In Figure 3.3, position-dependent hydrogen signal profiles of the coatings with cobalt are shown. Two stages can be distinguished in the four figures showing the drying. In the first stage the solvent evaporates, which takes approximately 1 hour. During this stage the film shrinks due to loss of solvent, given by the arrow on the left. During the second stage, a front develops at the top of the film that moves towards the bottom of the coating. In previous works, it was shown that this front is a crosslinking front^{68,69,87,93,99,102,103,106}. It forms due to the formation of chemical crosslinks at the top of the film, while the bottom part remains mobile. The signal in the top layer of the coating can no longer be detected with NMR due to the fast signal relaxation, which is a consequence of a strong decrease in the molecular mobility, which is demonstrated in Figure 3.1. That plot shows the decay in signal intensity as function of the echo time, which shows that in case of a cured film the very short (T_2) relaxation time leads to a lower signal of the first echo (first point in the curve) compared to an uncrosslinked film. Note that the thickness of the film stays constant during the crosslinking stage.

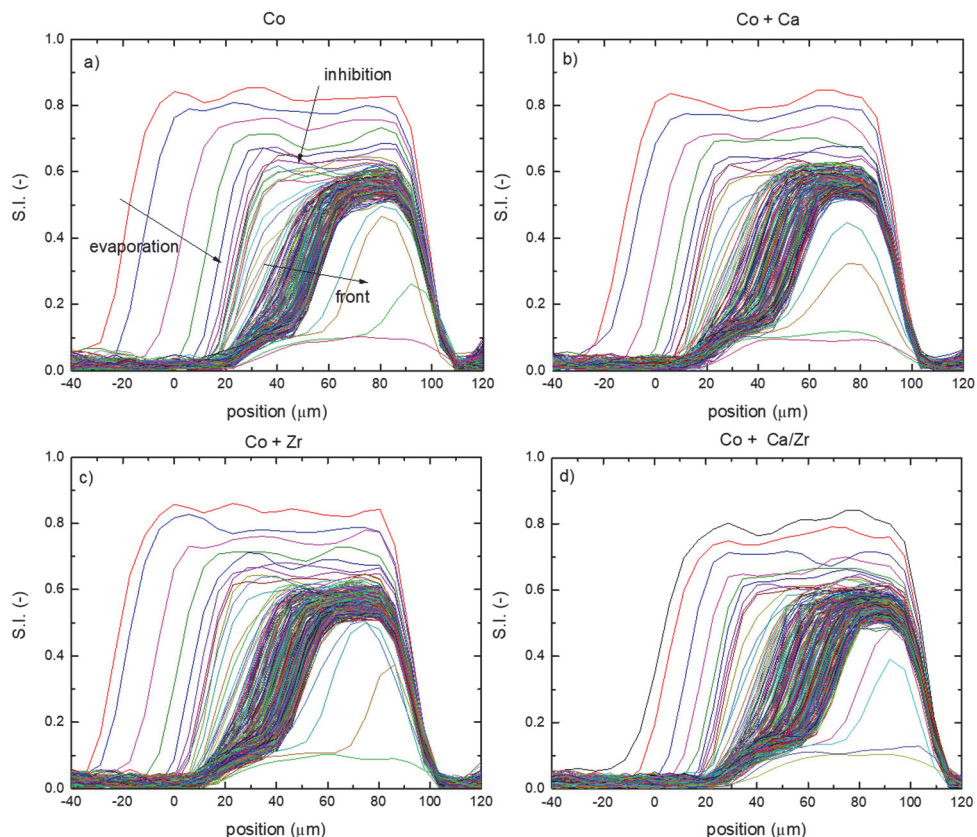


Figure 3.3. NMR profiles of the alkyd coatings with different secondary driers added to cobalt; a) Co; b) Co+Ca; c) Co+Zr; and d) Co+Ca/Zr. The profiles are plotted every 13 minutes during first 2 or 3 days. The last four profiles are plotted after 1, 2, 3 and 4 weeks. All profiles show front like curing.

In Figure 3.3 the profiles are plotted every 13 minutes during the first 2 or 3 days, and the last four profiles after 1, 2, 3 and 4 weeks respectively. In the curing several aspects can be observed. A drying front is formed moving slowly towards the bottom of the profiles. It is a slow process that is largely finished after 4 weeks. Note the final signal level at the end; the lower the final NMR signal level, the lower the polymer mobility. The profiles are all divided by a water reference to correct for signal variations as a result of coil sensitivity variations. During the chemical crosslinking the hydrogen density remains approximately equal, so the signal loss is only the effect of reduction in T_2 . The final level observed can also be used as an indication for the final degree of mobility or T_g ^{69,86}. In many cases this is said to be coupled directly to the degree of crosslinking. This is not straightforward, and only recently shown by Gezici-Koc et al.⁸⁶ that there is a clear link between T_2 , T_g and crosslink density measured by DMA. A densification of profiles may be seen between the evaporation and curing stage, indicated by the arrow, which is most profound in the Co sample without

secondary driers. It seems to be an inhibition period. We will return to that observation later for further analysis. Note that, no clear effects of secondary driers are visible in the profiles as presented here.

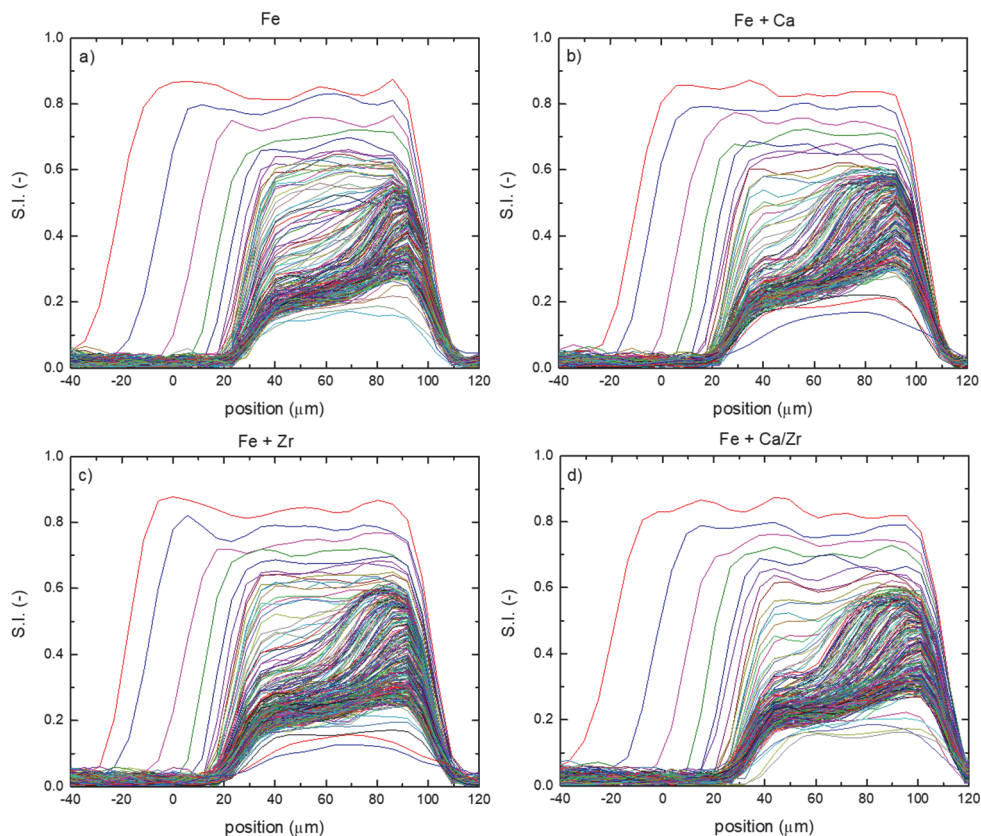


Figure 3.4. NMR profiles of the alkyd coatings; a) Fe; b) Fe+Ca; c) Fe+Zr; and d) Fe+Ca/Zr. The profiles are plotted every 13 minutes during first 2 or 3 days. The last four profiles are plotted after 1, 2, 3 and 4 weeks.

The influence of iron based drier (Fe) on the drying was also investigated. This is shown in Figure 3.4. After the evaporation stage, a densification of profiles is visible, indicating an inhibition period. As with cobalt a drying front is also formed in presence of the iron-based drier, but between the 20 μm and 50 μm position a more homogenous curing is observed compared to cobalt. An explanation may be that oxygen penetrates further into the coating, but when the curing starts at a certain time, a front is formed as a result of top layer curing forming a diffusion barrier. Also note that the final signal level is higher than that of cobalt, and that the sample with Zr has the lowest signal level at the end.

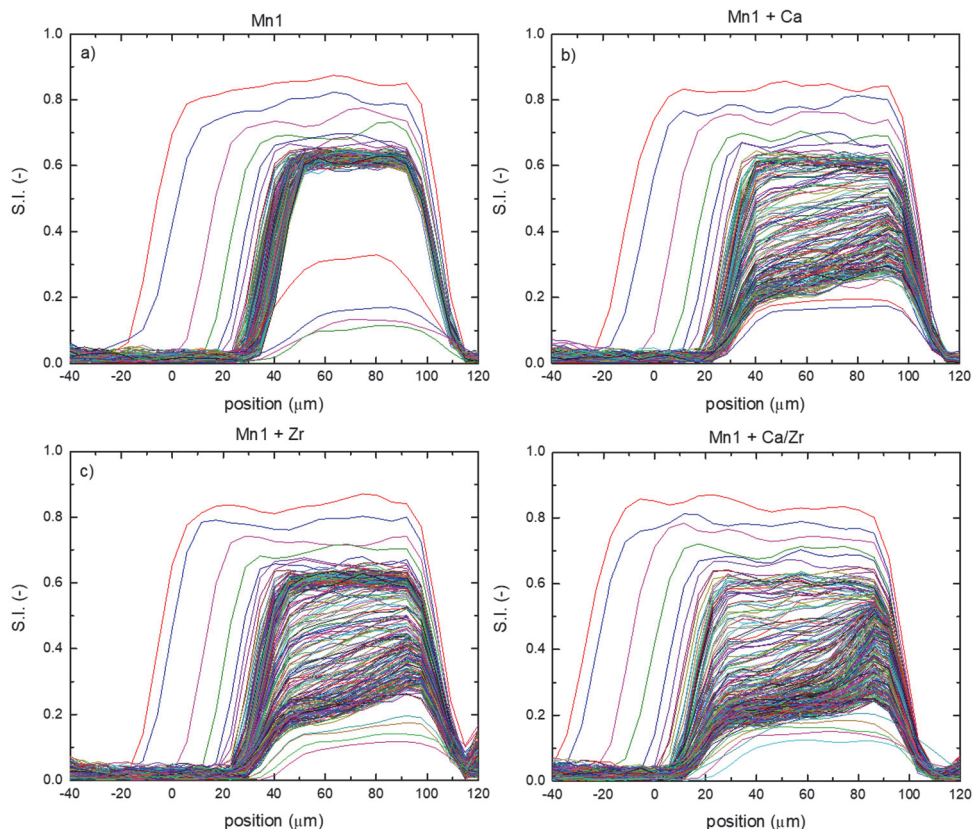


Figure 3.5. NMR profiles of the alkyd coatings; a) Mn1; b) Mn1+Ca; c) Mn1+Zr; and d) Mn1+Ca/Zr. The profiles are plotted every 13 minutes during first 2 or 3 days. The last four profiles are plotted after 1, 2, 3 and 4 weeks.

The influence of manganese based catalyst (Mn1) on the drying process was also investigated. This is shown in Figure 3.5. After the evaporation stage, curing seems to be inhibited in the absence of secondary driers. Only after a week, curing is observed with the decrease in signal intensity indicating a very long inhibition period. After the inhibition period the curing process is nearly homogeneous, which indicates the chemical reaction is the rate limiting processes compared to the oxygen transport process. Note that the final signal level is higher than that of Co and Fe. When adding the secondary driers, the inhibition seems to be reduced, and when both Ca and Zr are added a small front is observed near the bottom of the sample.

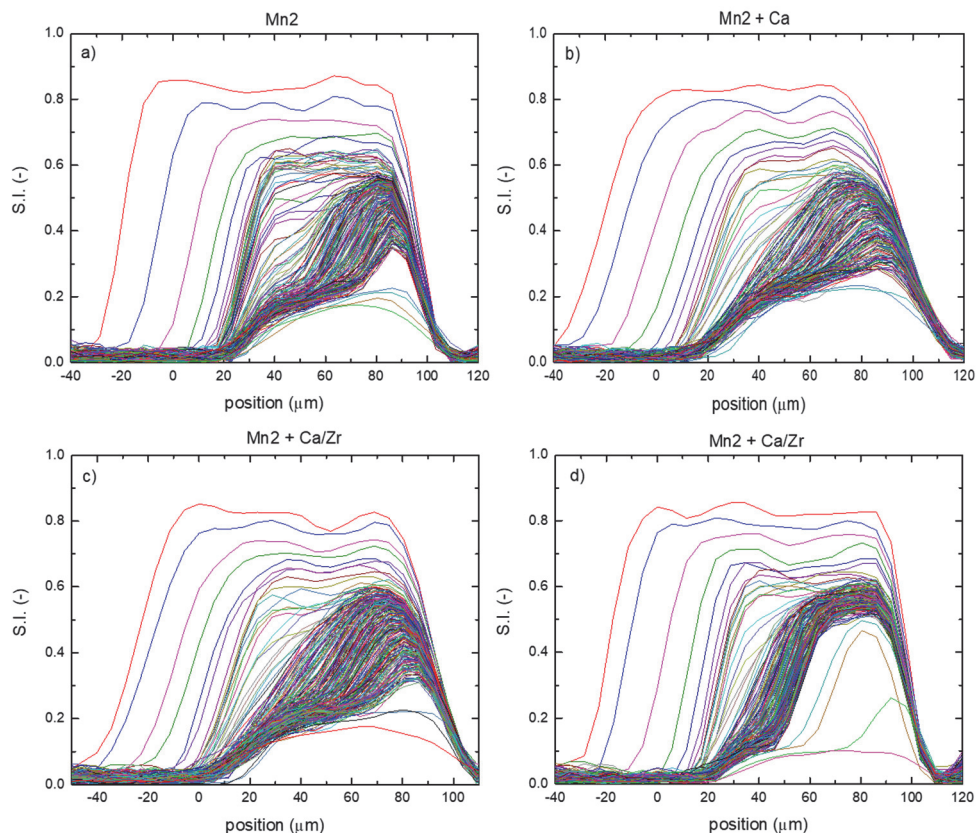


Figure 3.6. NMR profiles of the alkyd coatings; a) Mn₂; b) Mn₂+Ca; c) Mn₂+Zr; and d) Mn₂+Ca/Zr. The profiles are plotted every 13 minutes during first 2 or 3 days. The last four profiles are plotted after 1, 2, 3 and 4 weeks.

The influence of another manganese based catalyst (Mn₂) on the drying was also investigated. This is shown in Figure 3.6. After the evaporation stage, a densification of profiles is visible, indicating an inhibition period. This is reduced in the presence of secondary driers. A front is also formed. Note that the final signal level is higher than that of Co, and that the sample with Zr and Ca has the lowest signal level at the end.

3.3.2. The frontlike curing of alkyd coatings using different drier combinations

As explained in the introduction in case of cobalt based driers a curing front is observed. A typical example is presented in Figure 3.7, showing the front position against time, observed in an alkyd coating using high resolution magnetic resonance imaging. The curing process can be stopped by removing the oxygen atmosphere⁹³.

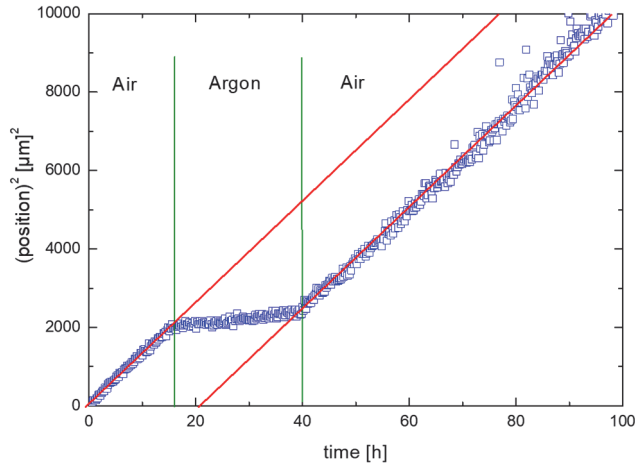


Figure 3.7. Example of front-drying, reproduction of Erich, et al. [93]. A clear $f^2 \sim t$ relationship is shown, which stops when flushing the coating with Argon instead of Air (time between green vertical lines).

The equation describing the progression of the front against time is given by the following equation:

$$f^2 = (n\rho_d)^{-1}\rho_0Dt, \quad (3.2)$$

where ρ_0 [mol/m³] represents the solubility of oxygen at the top of the coating, D [m²/s] the diffusion of oxygen, ρ_d [mol/m³] the density of the double bonds in the alkyd resin, n [mol/mol] the amount of oxygen per double bond. In other words $(n\rho_d)^{-1}$ can be considered the cured volume per mole of oxygen. The speed of the front thus depends on the amount of oxygen solubilized in the top surface, causing a flux towards the front by diffusion. At the front a certain amount of oxygen molecules is reacting to form a network.

In Figure 3.8 the front speeds are plotted for different drier combinations. Note that $x - x_0$ is the actual distance of the front from the top surface, and $t - t_0$ is the time after the evaporation process (t_0). In the case of cobalt, addition of Zr does not seem to affect the front speed, but when Ca is added the front speed is increasing, even more when added in combination with Zr. In case of Mn2 the front speed is much higher than Co without any secondary driers. As Mn1 did not show any crosslinking front a similar analysis could not be executed. The effect of the addition of secondary driers has the same effect as in case of Co; Zr addition does not seem to improve the front speed, but Ca or Ca with Zr does. In case of Fe, the front speed resembles that of Mn2 without any secondary driers. The addition of secondary driers in all cases increases the front speed. From the figures, one can clearly see that from all driers Co has the slowest front speed, and that addition of Ca increases the front speed. The exact mechanism by which Ca is increasing the front speed remains unknown.

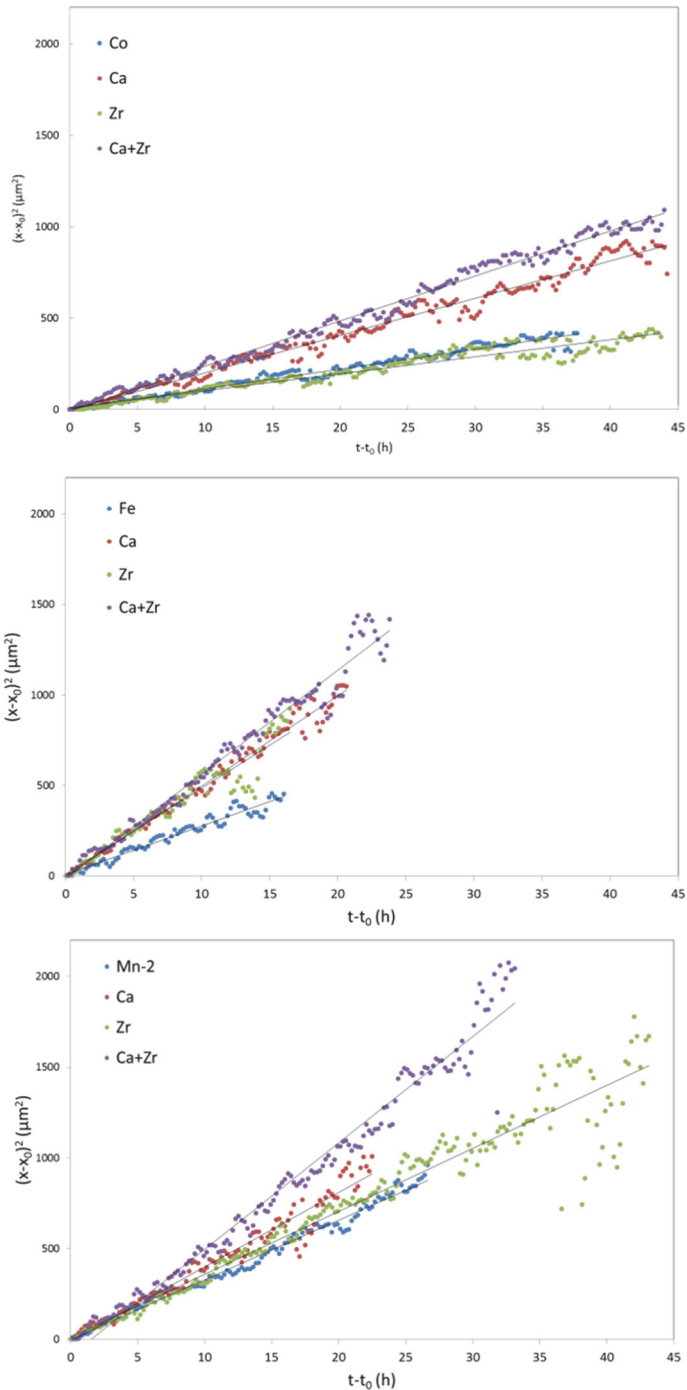


Figure 3.8. Front drying for the three primary driers (Co, Fe, Mn2) investigated. Clear $f^2 \sim t$ relationship is shown, three driers are plotted, each with three variations of secondary drier addition.

3.3.3. Characterization of the observed inhibition period

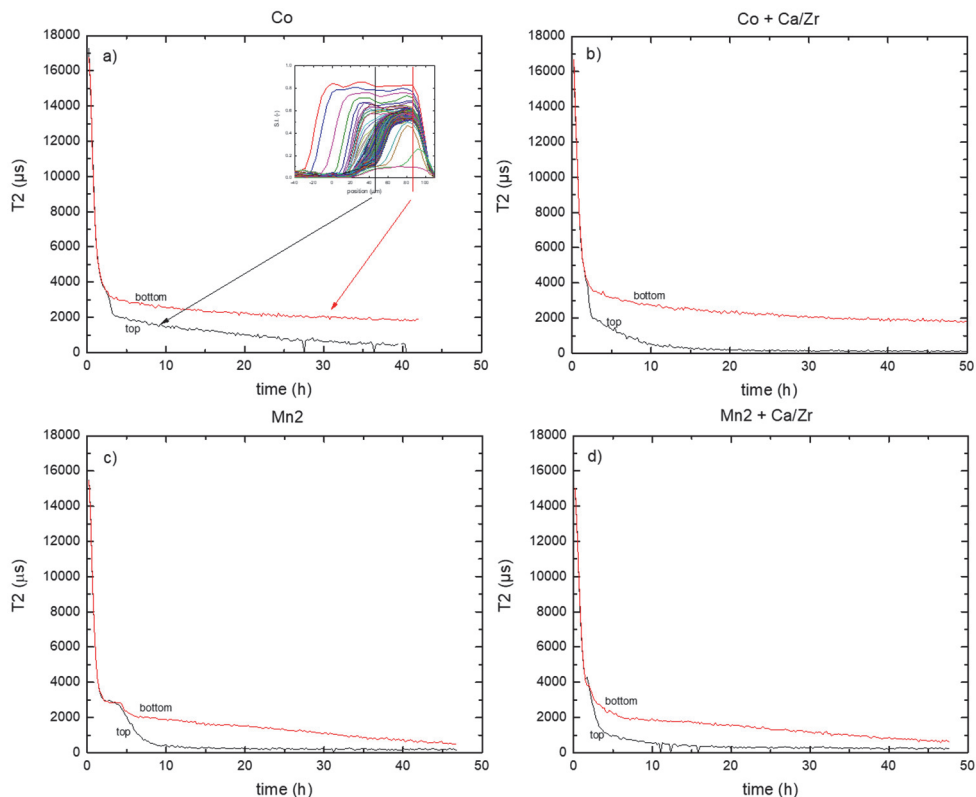


Figure 3.9. The time evolution of T_2 for two locations in the profiles, bottom and top, as indicated in a). a) and b) shows the T_2 for Co; c) and d) for Mn2. a), c) and d) show signs of inhibition, because the T_2 remains constant, just after the evaporation process.

Besides the signal profiles, also the spin-spin relaxation time (T_2) evolution during approximately 40 hours of drying at the top and the bottom are determined and shown in Figure 3.9. The analysis of T_2 in depth is a useful method to follow the crosslinking process. A lower T_2 value indicates a more crosslinked alkyd film^{68,69,87,93,99–103,106}. Two stages can be observed. In the first stage, the solvent evaporates, resulting in a fast decrease in T_2 . Although fitting with two T_2 values is best suited, this period is fitted with a single exponent still with reasonable accuracy ($R^2=0.98$), and allows to follow the more interesting part being the crosslinking process (that only allows fitting with one T_2). In about one hour, the T_2 value drops from 10 ms to 4 ms with a similar rate at each depth of the film. In the second stage, the T_2 evolves differently at the top and the bottom of the film, indicating the differences in the in-depth drying process. This observation indicates the formation of the skin layer (and resulting front ingress), together with hardness development.

Figure 3.9 a, c and d, show a inhibition period just after evaporation, as the T_2 remains constant, which is most clearly visible in Figure 3.9c. The addition of both Ca and Zr reduces this inhibition period. In case of Co+Ca/Zr, the inhibition period is no longer observable (Figure 3.9b).

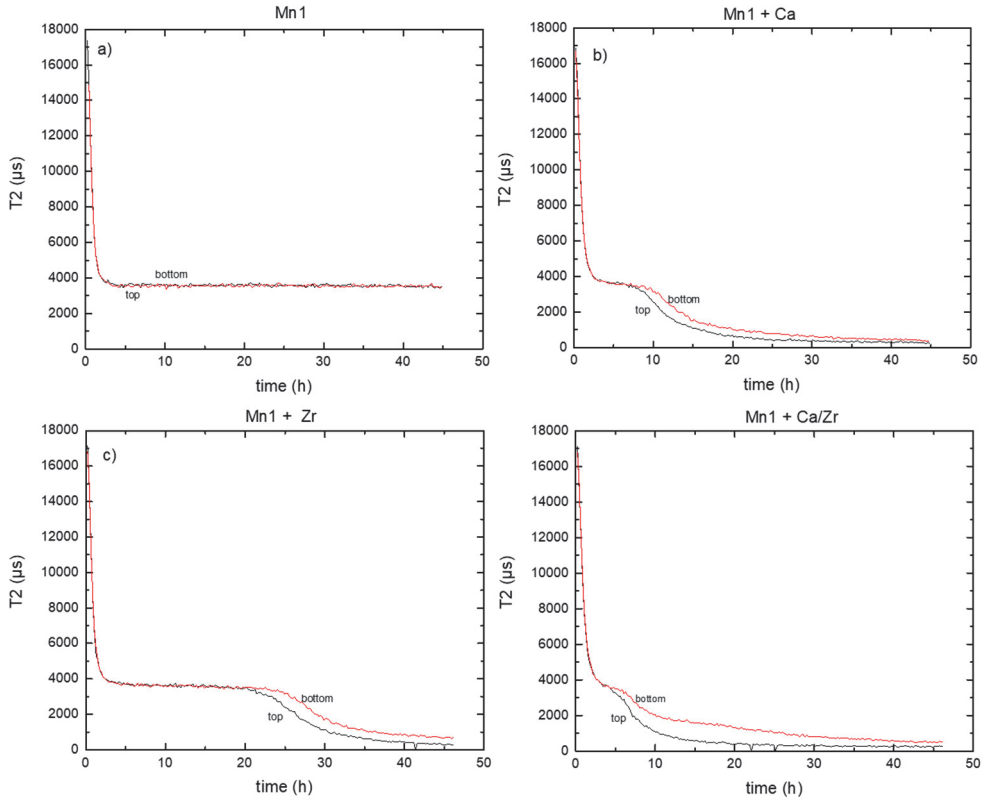


Figure 3.10. The time evolution of T_2 for two locations in the profiles, bottom and top. All figures show a long inhibition period, b) with Ca, c) with Zr, d) with Ca and Zr. When the secondary driers are added the inhibition period will decrease.

In Figure 3.10 the T_2 is plotted for Mn1 with different secondary drier combinations. In absence of secondary driers, the T_2 remains constant for over 40 hours. When Ca and Zr are added the inhibition period reduces considerably. Note that, when both Ca and Zr are added the inhibition period is the shortest. In order to see the effectiveness of each drier, we wish to characterize the inhibition period. To do so, an empirical equation is suggested to fit all our T_2 data. The equation is given by

$$T_2(t) = T_2^1 e^{-t/\tau_1} + T_2^2 \frac{e^{-\frac{(t-t_0)}{\tau_2}}}{1 + e^{-\frac{(t-t_0)}{\tau_2}}} + T_2^0 \quad (3.3)$$

where T_2^1 represents the T_2 for the paint in the pot, τ_1 is the time of evaporation, T_2^2 represents the T_2 for the pure resin in absence of solvent, t_0 is the time of inhibition since application of the paint, τ_2 is a measure of the reaction speed of the system, and T_2^0 is the T_2 of the final crosslinked network. The most complex part of the equation is the second part of the equation describing the inhibition period and reaction kinetics. In fact this part of the equation resembles a modified logistic growth curve, which can be expected after a temporarily inhibited reaction. In fact, we expect that as double bonds disappear and oxygen is reacting, a crosslinked network is formed. The crosslinked network reduces the mobility, and as NMR probes mobility the reaction becomes visible in an indirect way via change in T_2 . Figure 3.11 shows a typical fit of the T_2 data using Equation 3.3. One can see the quality of the fit as the red line is nearly undistinguishable from the data. Using this equation, it is now possible to focus on the typical parameters as a function of drier types and concentrations.

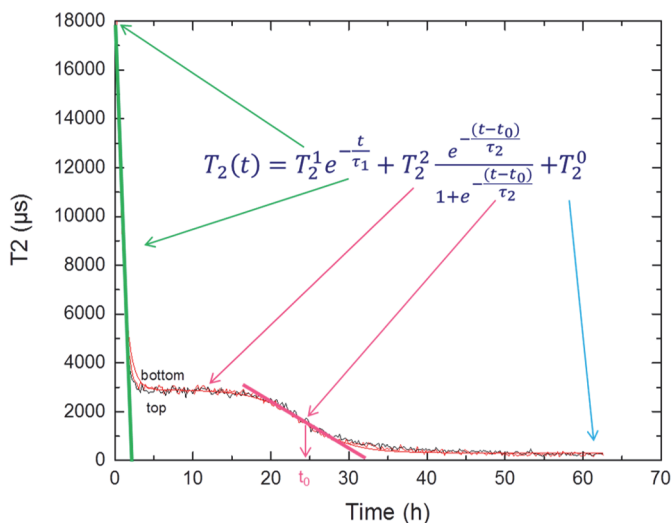


Figure 3.11. Example of T_2 as a function of time, showing a typical inhibition period of about 25 hours. The T_2 is plotted at the top and bottom of the sample. A fit of our empirical equation is fitted through the data. The arrows indicate the different parameters that characterize the different parts of the curve.

In Figure 3.12 the inhibition period is plotted as a function of concentration of secondary drier for Mn1. The concentration was reduced by a factor of 2 and 10, as well as increased by a factor of 2 and 10. The concentration in mmol per kg of catalyst is calculated to be able to investigate the effectiveness of reducing the inhibition period for each drier. The figure shows that Ca is the most effective in reducing the inhibition period, although Zr is also reducing the inhibition period with increasing concentration. It seems that the inhibition period (IP) is reducing with the third power root of the concentration, as the equation is

indicating in Figure 3.12. Consider the driers to be homogeneously reduced, the reduction of the inhibition period seems to be proportional to the distance of two manganese molecules. In short, it says that when the average distance between two drier molecules is reduced, the inhibition period reduces with the same factor. The exact mechanism remains open for discussion, as a more detailed explanation remains absent at this moment. Based on this behaviour it would be possible to predict the inhibition period for a certain concentration of secondary driers, and most probable even for mixtures, although that remains to be proven.

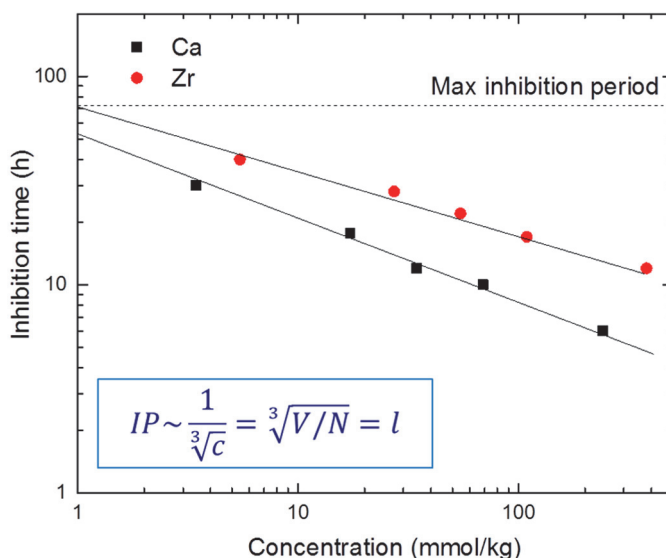


Figure 3.12. Inhibition period for Mn1 (DriCAT 2700F) as a function of concentration of secondary driers.

3.3.4. Glass transition temperatures and crosslink densities of dried films

NMR shows that the coating film cured by Co in presence of secondary driers seems to have the lowest mobility (the lowest T_2) after prolonged curing. To investigate the existence of a relation with the crosslink density Dynamic Mechanical Analysis (DMA) was carried out to determine the glass transition temperature and the crosslink density, see Figure 3.2. DMA provides the average crosslink density of the entire film.

Table 3.2 shows the glass transition temperature, T_g , and crosslink densities after crosslinking of the films after 2 weeks drying. The film with Co has the highest crosslink density of 0.387 mmol/cm³ while all others have a value around 0.230 mmol/cm³. The table shows that the crosslink density is the highest in case of Co and increases, for all driers, when Zr is added to the coating formulation.

Table 3.2. The table below shows the glass transition temperature, T_g , and the crosslink densities for the final films after 2 weeks drying.

Primary drier	Secondary drier	T_g (°C)	Cross.lin.dens. (mmol/cm ³)
Co	-	39.6	0.39
	Ca	37.6	0.37
	Zr	41.6	0.50
	Ca+Zr	39.8	0.46
Mn2	-	26.9	0.28
	Ca	26.5	0.20
	Zr	28.3	0.35
	Ca+Zr	29.2	0.32
Fe	-	28.9	0.22
	Ca	29.7	0.22
	Zr	30.7	0.34
	Ca+Zr	31.0	0.30
Mn1	-	27.6	0.19
	Ca	29.5	0.20
	Zr	31.5	0.32
	Ca+Zr	33.2	0.31

3.3.5. The effect of secondary driers on crosslink density and front speed

Figure 3.13 shows the results of the previous sections for the different primary driers (clustered per color) and the effect on both crosslink density and front speed in case of addition of secondary driers. The diagram shows that the lower the front speed the higher the crosslink density (or vice versa). In addition, it shows that when Ca is added to any of the primary driers the front speed increases (leading to an upwards vector in the diagram). When Zr is added the crosslink density is increased (leading to a vector to the right in the diagram). In case Ca and Zr are both added, the crosslink density as well as the front speed increases (leading to a vector pointing upwards to the right). The behavior as presented in Figure 3.13 can be considered a vector addition. Ca and Zr combination may present a synergistic effect on both crosslink density and front speed ⁹⁶, and it requires further research to prove whether or not it is only an addition effect.

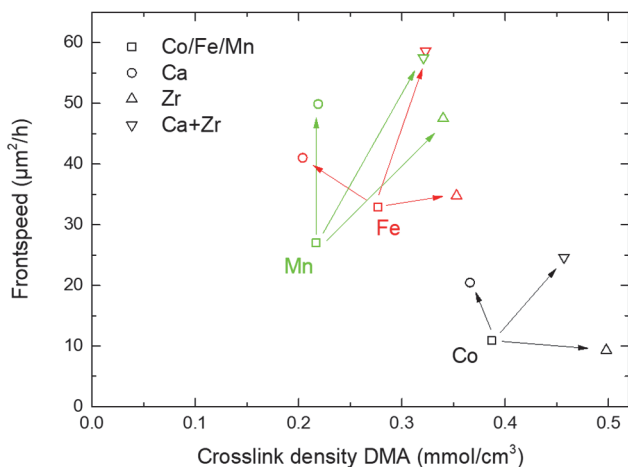


Figure 3.13. Front speed plotted against crosslink density for the different primary driers in combination with the secondary driers. Ca is represented by circles, Zr by triangles and Ca + Zr by inverted triangles. The figure plots the behavior change as a vector addition representation.

We may speculate on the possible mechanism based on the equation of the front speed. It seems that addition of calcium is most likely to increase the permeability of oxygen. Whether the permeability increases through increase of diffusion or solubility is unclear. As the cross-linking is not changed we expect that the other parameters remain unchanged. For the zirconium drier, the process is somewhat more difficult, as it shows that either physical or chemical crosslinks are added. As the front-speed remains the same, the mechanism may point towards physical cross-links, or more cross-links are formed with the same amount of oxygen in the network. The chance that both the oxygen transport and oxygen incorporation is increased in such a way that the front speed is exactly compensated, seems less likely.

3.4. Conclusions

In this study, we investigated the influence of the presence of secondary driers, based on Calcium and Zirconium, on the oxidative drying of alkyd coating films using manganese and iron based alternatives, next to cobalt as a reference. The alkyd films are studied by NMR profiling and Dynamic Mechanical Analysis (DMA).

From the NMR profiles of the curing process we found that an inhibition period is present in the samples. To characterize the inhibition period from the T_2 plots, an equation is suggested that allows to obtain quantitative parameters for comparison, providing a clear definition of a timescale characterizing the inhibition period. The duration of the inhibition period is reduced through the addition of the investigated secondary driers. Calcium seems to be more efficient than Zirconium in reducing the inhibition period. The exact mechanism, however still needs to be unraveled.

Furthermore, we found that cobalt, iron and one of the manganese based driers show a front drying. The addition of the calcium based secondary drier increases the front speed, which is most likely due to increasing the permeability of oxygen. This seems generic for all the primary driers used in this study.

Zirconium increases the crosslink density, according to the DMA results. Zirconium based drier may slightly increase the front speed. In a diagram showing both the crosslink density and front speed, the effect of calcium and zirconium can be described as a vector addition. Further quantification of the vector addition and the effect of the secondary driers as a function of concentration is suggested to be investigated in future work. The observed dependence of the concentration and the finding of the vector addition scheme will help in understanding the mechanisms on a molecular level.

Chapter 4

Bound and free water distribution in wood during water uptake and drying as measured by 1D magnetic resonance imaging

Knowledge on moisture transport in wood is important for understanding its utilization, durability and product quality. Moisture transport processes in wood can be studied by Nuclear Magnetic Resonance (NMR) imaging. By combining NMR imaging with relaxometry, the state of water within wood can be identified, i.e. water bound to the cell wall, and free water in the cell lumen/vessel. This study presents how the transport of water can be monitored and quantified in terms of bound and free water during water uptake and drying. Three types of wood from softwood to hardwood were selected covering a range of low to high density wood; pine sapwood and oak and teak. A calibration is performed to determine the different water states in each different wood type and to convert the NMR signal into moisture content. For all wood types, water transport appeared to be internally limited during both uptake and drying. In case of water uptake, free water was observed only after the cell walls were saturated with bound water. In case of drying, the loss of bound water starts only after vanishing of free water, irrespective of the position. Obviously, there is always a local thermodynamic equilibrium of bound and free water for both uptake and drying. Finally, we determined the effective diffusion coefficient (D_{eff}). Experimentally determined diffusion constants were compared with those derived by the diffusion models for conceptual understanding of transport mechanism. We found that diffusion in the cell wall fibers plays a critical role in the transport process.

This chapter has been published as

Ö. Gezici-Koç *et al.*, *Cellulose* 24 (2): 535-553 (2017).

4. Bound and free water distribution in wood during water uptake and drying as measured by 1D magnetic resonance imaging

4.1. Introduction

Wood is a hygroscopic and porous material in which the distribution and interactions of water play a crucial role in wood processing and durability. In many situations and applications, wood is undergoing fluctuations in moisture content due to periodic water absorption and desorption. Understanding the water absorption and desorption characteristics of wood is of practical importance, since the mechanical properties or the dimensional stability of wood are influenced by the moisture content. Moreover, a high moisture content may result in durability loss due to fungal growth and/or delamination of an applied protective layer.

In wood, water can be present in two states. First, the water can reside in cell walls, which is called bound water. Second, water may exist in liquid pockets located in the cell lumen and other void spaces, called free water. Generally, one can observe a transition from a regime where only bound water is present towards a regime where free and bound water are present together. The point where this transition occurs is called the Fiber Saturation Point (FSP)¹⁰⁷. Understanding the transport properties requires understanding the changes in bound and free water¹⁰⁸. Although many studies have been performed to understand water transport properties, it is not easy to identify the state of water within wood, and especially to determine each state during uptake or drying by experimental techniques, such as weighing⁵⁷ or X-ray computer tomography (CT)⁵⁸ or neutron radiography⁵⁹.

One of the methods to study water in wood is Nuclear Magnetic Resonance (NMR) Imaging. It is a non-invasive method that provides temporally and spatially resolved moisture profiles⁵⁶. The intensity of the NMR signal is proportional to the number of hydrogen nuclei in the sample, i.e. the water content. NMR Imaging has been proven to be an excellent tool to determine the distribution and the concentration of water in wood during drying^{42,52,53}, and during uptake^{44,54,55}. In situ determination of local moisture content has been achieved by portable NMR devices^{109,110}. Another important advantage of NMR over other methods is its ability to distinguish between bound and free water by relaxation analysis (T_2), i.e. the decay of the NMR signal^{111–114}. For detailed information, please see section “Relaxation analysis of water in wood”.

To understand the transport properties, moisture profile determination and water state characterization during water uptake and drying should be carried out. In previous studies with NMR, such determination of moisture profiles and characterization of water states during drying was achieved for yellow poplar¹¹⁵, Douglas fir¹¹², red cedar^{52,112}, Norway spruce¹¹⁶ and Scots pine^{117,118}. These studies provide spatially resolved one dimensional moisture profiles, but no spatially resolved relaxation analysis. The role of the porosity on

water transport was studied by Kekkonen *et al.* ¹¹⁹. They investigated absorption of water in thermally modified wood by applying various NMR methods. Their results show that thermal modification partially blocks the access of water to cell walls. The noticeable decrease in free water for the samples modified above 200 °C indicate that large amount of pits connecting wood cells are closed due to high modification temperature.

In this work, we aim to visualize and quantify bound and free water distribution for pine sapwood, oak and teak during water uptake and drying by using NMR imaging and relaxometry. More specifically, five subsequent steps are taken to answer to this objective. The first step is to discriminate bound and free water in the measured signal, i.e. to calibrate the signal. The second step is to convert the NMR signal into moisture content. In the third step we monitor and quantify the changes in bound and free water, and the order of filling/emptying of each state during uptake and drying, whereas in the fourth step the effective diffusion coefficient, D_{eff} , is determined. Finally, in the fifth step these experimental D_{eff} values are compared with those derived by two diffusion models.

4.2. Materials and methods

4.2.1. Wood types

The selected wood types and their characteristic properties are given in Table 4.1.

Table 4.1. Selected wood types and their general characteristics.

Wood type	Softwood/hardwood	Density (kg/dm ³)	Structure
Pine sapwood (<i>Pinus sylvestris</i>)	Softwood	~ 0.54	No vessels
Oak (<i>Quercus petraea</i>)	Hardwood	~ 0.64	Ring porous
Teak (<i>Tectona grandis</i>)	Hardwood	~ 0.64	Semi-ring porous

Wood has a complex heterogeneous microporous structure. Optical microscope images of pine sapwood, oak and teak are given in Figure 4.1, in which the heterogeneity in the samples are visible. The microscopic cellular structure of wood, including annual growth rings and rays, presents the characteristic patterns in different wood types. For all studied wood types, annual growth rings are visible with earlywood (spring) and latewood (summer) rings. Rays are the radial cells, running perpendicular to growth rings, which provide radial transport. As shown in the inset sketch, the inner cavity of a wood cell is called lumen, and the surrounding structural layer is the cell wall, which consists mainly of cellulose, playing an important role in the wood-water relationship. Wood cells are equipped with pits that serve as passages of transport between neighbouring cells.

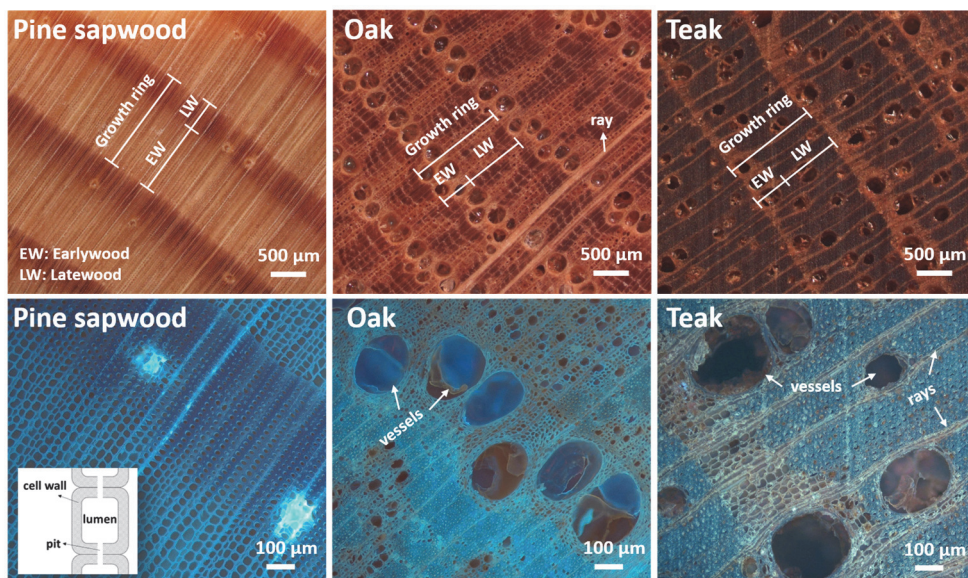


Figure 4.1. Optical microscope images of cross-sections of pine sapwood, oak and teak. The above “overview” images are with incident halogen light, the below “detailed” images are with UV light. The inset presents a simple sketch of a wood cell.

Wood is classified as either a hardwood or softwood, in which they differ in the physical structure. Hardwoods have more complicated anatomical features and greater structural variation compared to softwoods, which results a greater range in permeability and capillary behaviour¹²⁰. Hardwoods have a higher density than most softwoods. In softwoods, such as pine, the water transport throughout the wood is achieved by elongated cells, called tracheids, which are running lengthwise with the trunk. The diameter of tracheids can vary based on being earlywood or latewood tracheid. In pine sapwood, earlywood cells have thinner cell wall and larger lumen, while latewood cells have thicker cell wall and smaller lumen. The primary distinguishing feature between softwoods and hardwoods is that hardwoods, such as oak and teak, have vessels, i.e. pores, that transport water throughout the wood. In some species, such as oak, the earlywood has larger pores compared to the latewood, in which they are characteristically known as “ring-porous” wood. In some other species, such as teak, the pore size gradually decreases from the earlywood to the latewood, but the pores do not form clear rows as observed in ring-porous woods. They are known as “semi-ring porous” wood.

Next to structural differences between the studied wood types, there are differences in the cut directions. In Figure 4.2, the schematic diagram of wood log showing different cut directions is presented.

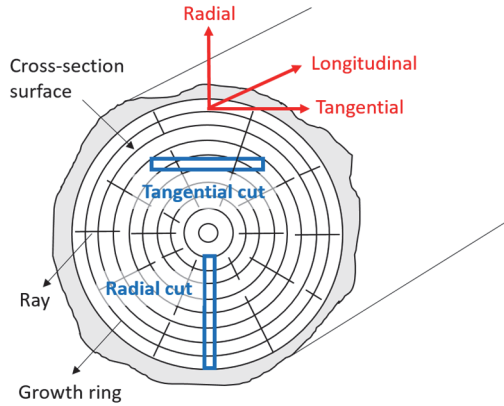


Figure 4.2. The schematic diagram of wood log showing different cut directions.

In this study, the pine panels have a radial cut in which the rays are almost parallel and the growth rings, i.e. longitudinal tracheids, are almost perpendicular to the surface. Teak and oak have a tangential cut where the growth rings and rays are oriented diagonally (about 45° angle) to the surface, but perpendicular to each other.

4.2.2. NMR imaging and relaxometry

Principles

The NMR principle is based on exciting the magnetic nuclei, in our case hydrogen nuclei, placed in a magnetic field by a radio frequency (RF) pulse and detecting the induction in an RF coil. The resonance frequency, f , of the magnetic nuclei depends on the magnitude of the applied magnetic field, \vec{B} , according to $f = \gamma |\vec{B}|$, wherein γ is the gyromagnetic ratio ($\gamma = 42.58$ MHz/T for hydrogen nuclei). In order to obtain spatial information, the resonance frequency is varied with position according to $f = \gamma(B_0 + zG_z)$, wherein G_z represents the linear magnetic field gradient in the z -direction, and \vec{B}_0 is the main magnetic field in the z -direction. The NMR signal gives information on the mobility of the magnetic nuclei, in our case hydrogen nuclei, next to giving the density (concentration) of these nuclei. As the water molecules (i.e. the hydrogen containing molecules) inside the pores are excited by an NMR pulse, diffusion causes random collisions between the water molecules and the pore walls, which in turn causes relaxation, T_2 , which describes the decay of the NMR signal. T_2 is related to local mobility, i.e. T_2 is longer when freely moving water molecules are in bulk water or shorter when their mobility is restricted by a small volume.

Settings

A main magnetic field of 0.75 T was used with a constant gradient of 418 mT/m in the z -direction, i.e. parallel to \vec{B}_0 . In the experiments, the center of the sample was aligned at the

isocenter of the magnet. Slice selection was achieved by turning on linear magnetic field gradient, G_z , while applying an excitation pulse that allows rotating the spins, which are located in a slice through the sample. The sample was kept at a fixed position and multiple slices covering the whole sample were obtained by varying the center frequency, as illustrated in Figure 4.3.

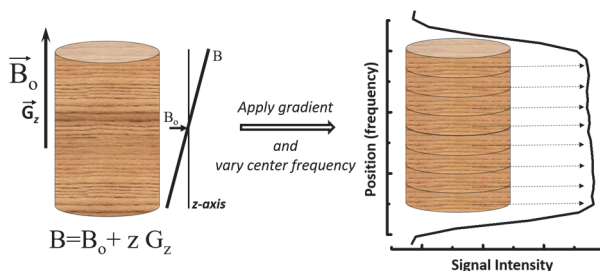


Figure 4.3. Slice selection by NMR.

Hahn Spin Echo (HSE) sequence 121 , $\alpha_x^\circ - \tau - 2\alpha_y^\circ - \tau - \text{echo} - \tau$, was used to obtain the hydrogen density profiles, where α is the flip angle and nominally equals to 90° with a pulse time of $25 \mu\text{s}$. A Carr-Purcell-Meiboom-Gill (CPMG) sequence 122 , $\alpha_x^\circ - \tau - [2\alpha_y^\circ - \tau - \text{echo} - \tau]_n$, was used to measure the relaxation time at several points through the whole sample. n is the number of echoes. The interecho time ($t_e = 2\tau$) used in the experiments equals $200 \mu\text{s}$, while the recording window (t_{ww}) to measure the echo has a duration of $120 \mu\text{s}$. The resulting NMR signal shows an exponential decay, as described by:

$$I(\tau) = \sum_{i=1}^m I_i \exp\left(-n \cdot 2\tau / T_2^i\right), \quad (4.1)$$

where $I(\tau)$ is the observed NMR signal at a time, I_i is the signal from each exponential component, and m is the number of components. The signal intensity of each exponential term is proportional to the pore volume. Therefore, the signal intensity of each term versus T_2 values produces a continuous spectrum of T_2 values, i.e. a map of the volume occupied by each pore size or the pore size distribution.

Note that the height and width of the T_2 peaks are dependent on the quality of the fit. The peak maximum value is taken for the relaxation time determination and the area under the peak is proportional to the volume occupied by each component 123 .

The settings are summarized in Table 4.2. Δx is the theoretical spatial resolution, n_{avg} is the number of signal averages, and t_{RT} is the repetition time between two subsequent pulses.

The measured signal profiles are divided by the signal profile of a homogeneous reference sample (same volume) allowing the local hydrogen density to be determined. As a reference sample, an aqueous 0.01 M CuSO_4 solution was used.

Table 4.2. The measurement settings of HSE and CPMG pulse sequences used during water uptake and drying of all selected wood types.

	t_e (μs)	t_{ww} (μs)	t_{90° (μs)	G_z (mT/m)	Δx (mm)	n	n_{avg}	t_{RT} (s)
HSE	200	120	25	418	0.46	-	4	8
CPMG	200	120	25	418	0.46	1024 (water uptake) 2048 (drying)	32	8

4.2.3. Relaxation analysis of water in wood

Several researchers performed relaxation analysis to distinguish water states in wood, especially softwood species^{112,113,124} as it has a simpler anatomical and more homogeneous structure. In softwood, three relaxation times are observed as related to three different environments for the hydrogen nuclei^{112,113,124}, i.e. the cellulose of solid wood, water in the lumen and water in the cell wall. Figure 4.4 shows a schematic presentation of different states of water present in wood.

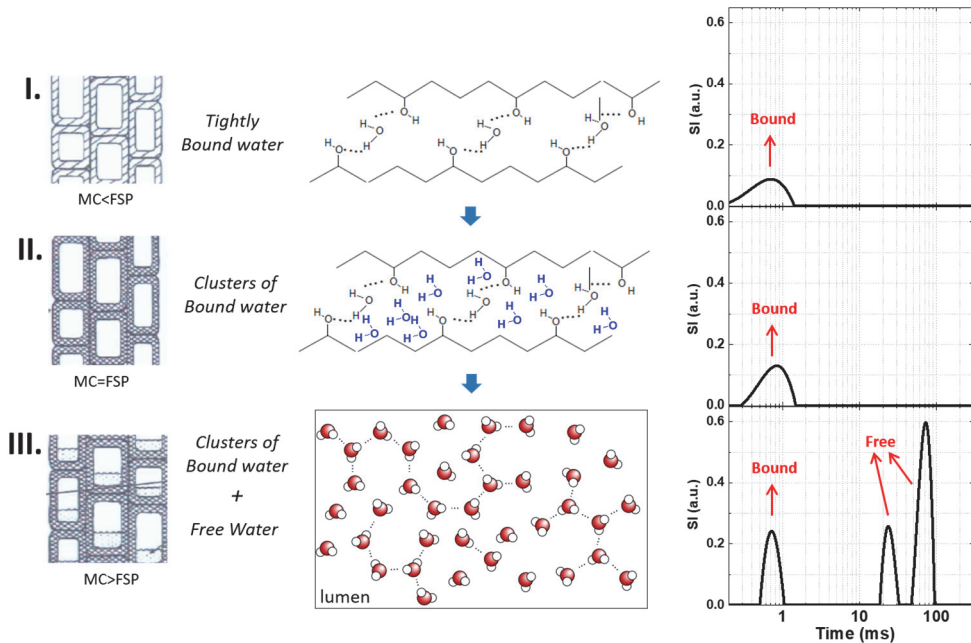


Figure 4.4. The schematic presentation of different states of water present in the cell wall and the lumen, the interactions (hydrogen bonds) between water and the hydroxyl groups of cellulose, and the relaxation time distributions, when (I) $MC < FSP$, (II) $MC = FSP$, and (III) $MC > FSP$.

Cellulose is the main constituent of the cell walls of wood fibres and contributes to the water adsorption of wood through its numerous hydroxyl groups^{120,125}.

As in the case I, when the moisture content (MC) is far below the FSP, the cell wall water is tightly bound to the hydroxyl groups of cellulose by hydrogen bonds along the chains of the amorphous or paracrystalline regions via reversible processes¹²⁰. Note that the water does not penetrate into the crystalline regions of cellulose¹²⁶. It results in a relatively short relaxation time, called bound water. When the MC increases towards the FSP, as in case II, more water molecules with an increased mobility are present in the cell wall, resulting in a small increase in the short relaxation time. In fact, one can consider them as clusters of water that are still bound. It is hard to differentiate these two cases (I and II) by looking at T_2 values, since there may not be a significant difference. On the other hand, a signal increase is observed for case II due to an increase in hydrogen nuclei. When the MC increases above the FSP, as in case III, water will be present within the lumen having a longer relaxation time, called free water. Different T_2 values in the range of free water result from the presence of different sized lumen or other void spaces. For example, earlywood cells have wider lumen, so longer T_2 , compared to latewood cells^{112,119}.

The wood cellulose has very short T_2 around tens of microseconds, which is too short to be observed in the used NMR set-up. The bound water in the cell wall has a T_2 typically ranging from hundreds of microseconds to several milliseconds, whereas the free water in the lumen has a T_2 typically ranging from ten to hundreds of milliseconds. Additionally, later studies showed an extra slow relaxing component in hardwood due the presence of vessel elements^{127,128}. The free water in vessels may have higher T_2 values compared to the water in lumen.

4.2.4. Sample preparation for calibrating the NMR signal

To convert the NMR signal to moisture content, calibration was performed for all three wood types. For each type of wood, twelve samples were prepared by cutting small cylinders with a diameter of 20 mm and height of 10 mm. They were initially at room condition having an ambient relative humidity (RH) of about 40%. Then, they were equilibrated at 12%, 22%, 33%, 43%, 53%, 65%, 75%, 85%, 93%, 97% and 100% RH above saturated salt solutions at room temperature (~ 22 °C). One sample from each type of wood was immersed in distilled water to achieve a fully saturated state. Equilibration took at least four weeks and was checked by monitoring the sample weight. The equilibrium moisture content (EMC) is set when the wood reaches a stable moisture content at a certain RH and temperature. After gravimetric determination of EMC of each sample and performing NMR measurements, they are oven dried at 105 ± 2 °C for 2 days. The MC is determined gravimetrically and expressed as a percentage, from the ratio of the mass of water divided by the oven dried mass of wood samples. The average of oven dried weight of twelve

samples was found as 1.7 ± 0.04 g for pine sapwood, 2.0 ± 0.04 g for oak and 2.0 ± 0.02 g for teak.

4.2.5. Samples and sample holders for water uptake and drying

20 mm diameter cylindrical samples were drilled from 10 mm thick wood panels (radial cut for pine sapwood, and tangential cut for oak and teak). For water uptake and drying measurements, the samples were initially at room condition having an ambient relative humidity (RH) of about 40%. Prior to the water uptake measurements, all samples were equilibrated at 33% RH for at least 4 weeks. Teflon sample holders were used to prevent interference with ^1H NMR signal. The sides of the samples were sealed with Teflon grease and Teflon tape, so the water can only enter the wood from the top side. Distilled water was put on top of wood samples.

Prior to the drying measurements, all samples were saturated until their maximum MC was reached. This was achieved by immersing the specimens in distilled water for at least one month. For saturation, the specimens were exposed to water from all sides, and full saturation was checked before the drying experiments were carried out. Teflon sample holders for drying measurements are illustrated in Figure 4.5.

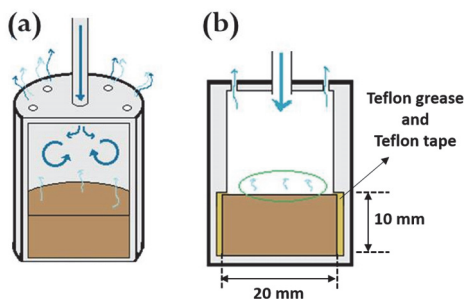


Figure 4.5. (a) An illustration of the sample holder for drying measurements, showing the air flow inside, (b) and the inner structure of the sample holder.

They were designed to seal the sides of the sample, so the water can only leave the wood from the top side. The sample holder has two different diameters inside (Figure 4.5b). The lower part has a diameter ensuring that the sample is tightly fit. The upper part has a smaller diameter preventing the sample to be moved, and simultaneously prevents water escaping from the sides. To ensure closure of the sides, the sides of the wood samples were covered with Teflon grease and Teflon tape before placing in the holder. Furthermore, dry air was blown from the top of the sample holder. The air flow was set at 3 L/min with an RH about 0-5% at room temperature (~ 22 °C).

4.2.6. Dynamic Vapor Sorption (DVS)

The equilibrium moisture sorption of all samples was analysed using a Dynamic Vapor Sorption (DVS) instrument (Q5000 SA from TA Instruments). The measurements were performed at a constant temperature of 25 °C with an initial sample weight of 2.0-4.0 mg. Weight changes were determined with a thermobalance (weight accuracy of 0.1% and signal resolution of 0.01 μg). Samples were initially dried for 10 h at RH of 10%. The RH was then increased from 10% to 98% (in 10% steps from 10% to 90%, and one 8% step from 90% to 98%), and subsequently decreased in similar steps till 0%. For all RH steps, the instrument was run in a dm/dt mode (mass variation over time variation) to detect when equilibrium was reached.

4.3. Results and Discussion

4.3.1. Equilibrium water sorption and signal calibration

For a profound analysis of water transport in wood, a full understanding of water binding to the wood is required. This enables calibration of the NMR signal, as to relate it to the moisture content in pine sapwood, oak and teak.

4.3.1.1. Sorption isotherms

In Figure 4.6, sorption isotherms of pine sapwood, oak, and teak are given quantifying the amount of water in wood at different humidity conditions.

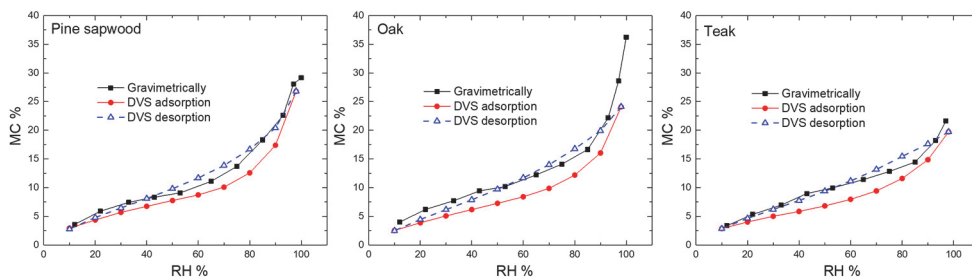


Figure 4.6. Sorption isotherms for pine sapwood, oak and teak, determined gravimetrically at 22 °C and measured by Dynamic Vapor Sorption (DVS) at 25 °C.

Besides gravimetrically determined sorption isotherms, the results of Dynamic Vapor Sorption (DVS) are included. Note that gravimetric determination uses different samples for each RH at 22 °C, whereas DVS concerns one and the unique sample at 25 °C. Although the equilibrium moisture content (EMC) at a certain RH varies for different wood types, the sigmoidal shape of the sorption isotherm is similar for all wood types. The MC increases almost linearly at lower RH region (below 60%), while the MC increases rapidly with humidities above 60% RH. The inflection point is the result of the transition of water in a

bound state to the formation of clusters of bound water (see Figure 4.4). This transition occurs between 60 - 80% RH for the wood species studied.

For pine sapwood, oak and teak, the gravimetrically determined sorption isotherms are similar to the DVS desorption isotherms. However, the gravimetrically determined sorption isotherm is neither desorption nor adsorption, because the samples were initially at about 40% RH. There is difference between the adsorption and desorption isotherms as measured with DVS, which shows hysteresis for all wood types. The wood hysteresis is not taken into account throughout this study.

The FSP is found to be around a MC of 29% for pine sapwood, 30% for oak and 22% for teak.

4.3.1.2. Identifying bound and free water at different humidity conditions

Knowing the sorbed amounts, the question is now in which state water molecules are in wood. Therefore, a relaxation analysis is performed at different humidity conditions, see Figure 4.7. The figure shows the T_2 distribution plot for the studied wood types at various humidity conditions ranging from 12% to 100% RH and fully water saturated condition.

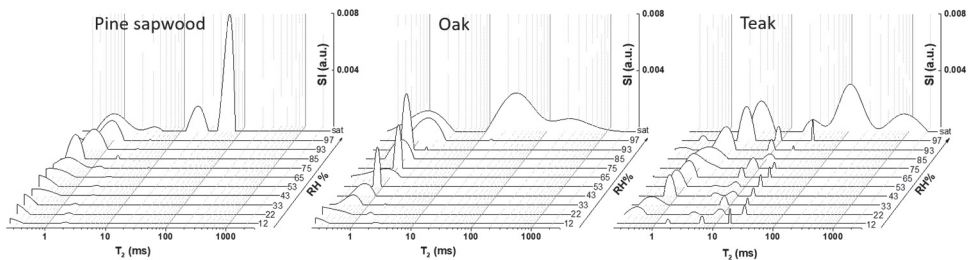


Figure 4.7. Relaxation time (T_2) distributions of the samples equilibrated at different humidity conditions and fully water saturated sample.

Pine sapwood

A relaxation time above 10 ms is observed only in the fully saturated sample. At RH below 100%, only short relaxation time is visible, which decreases from 1 ms to the values below 0.2 ms with decreasing RH. A long T_2 observed in the fully saturated sample corresponds to free water in the lumen or in other void spaces. It shows two well-separated relaxation times around 20 ms and 60 ms due to possible differences in the lumen size. The short $T_2 \leq 1$ ms corresponds to bound water in the cell wall. The decrease in T_2 of bound water with decreasing RH is due to the decrease in the mobility. The water in the bound state below 75% RH has very restricted mobility because of hydrogen bonding with the cellulose of the cell wall. Consequently, it has a very short relaxation time, which is shorter than the echo time used for CPMG measurement, i.e. 200 μ s. Since some of the spins corresponding to tightly bound water already relaxed before they were measured, it results in partly detecting the bound water, which is observable in the T_2 distribution plot.

Oak

Compared to pine sapwood, the main difference is that the long relaxation time observed for the fully saturated sample has a very broad distribution ranging from 10 ms to 300 ms. The broad distribution reflects the polydispersity of the pore sizes. The short T_2 corresponding the bound state is around 1 ms for fully saturated sample, which decreases to lower values around 0.5 ms with decreasing RH till 33%. At 12% and 22 % RH, T_2 is even shorter, being below 0.2 ms.

Teak

Comparing the relaxation times corresponding to bound and free water in pine sapwood and oak, there are additional peaks observed for teak. The relaxation time distribution ranging from 30 ms to 600 ms corresponds to the water in the free state, which is only available in the fully saturated sample. The relaxation time corresponding to bound water is around 3 ms in fully water saturated condition, around 2 ms for high RH (97%), and a shift towards lower values (around 0.5 ms) at relatively dry conditions. The additional peaks are observed between 4 ms and 30 ms, which seems similar at all RH. We separate the total signal intensity (SI) into the sections of the bound water (below 4 ms) and the additional peaks (between 4 ms and 30 ms) based on the relaxation analysis in Figure 4.7, by summing up the signal intensities in the relative sections.

In Figure 4.8, the corresponding signal intensities of these two sections are shown versus RH. The gravimetrically determined sorption isotherm is also included in the graph.

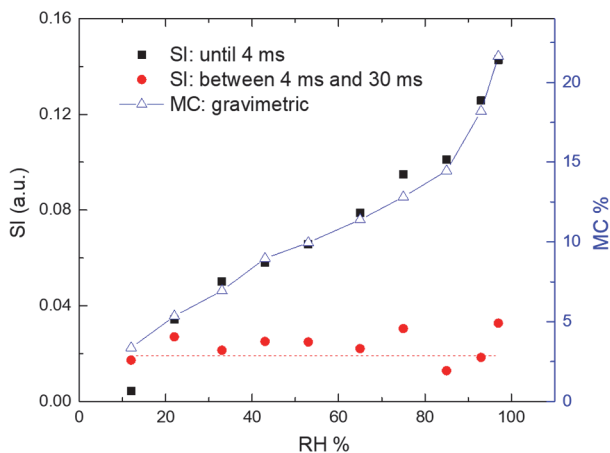


Figure 4.8. NMR signal intensities of the section below 4 ms and the section between 4 ms and 30 ms in the relaxation time distributions of teak at different humidity conditions, and the gravimetrically determined sorption isotherm.

The shape of the measured signal versus RH curve for the section below 4 ms is in agreement with the sorption isotherm. At very low RH (~10%), NMR underestimates the

amount of bound water as the T_2 is shorter than the echo time resulting in signal loss. For the section between 4 ms and 30 ms, the measured signal seems to be around 0.02, irrespective of the RH. This suggests the presence of a component in teak which is not influenced by the water content. It can be low-molecular-weight organic compounds known as extractives^{120,129,130}.

4.3.1.3. Calibrating the NMR signal

The signal intensity (SI) of the first echo of CPMG sequence was calibrated to obtain the total wood moisture content, as shown in Figure 4.9.

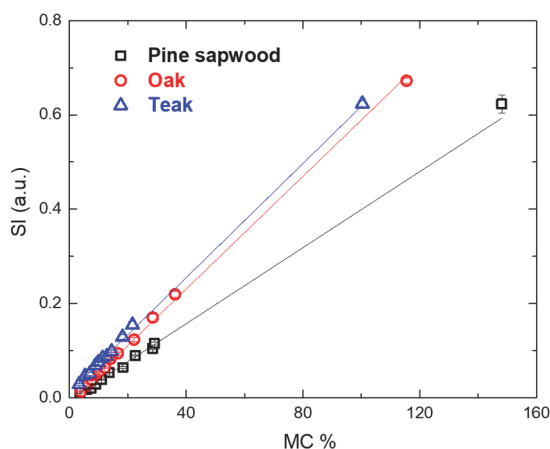


Figure 4.9. The signal intensity of the first echo of CPMG versus moisture content (mass percent) for pine sapwood, oak and teak. The solid lines are the linear fits.

Based on the average SI versus the MC of each of the equilibrated samples in the range of 12% to 100% RH and the fully water saturated sample, there is a linear relationship between the corresponding SI and the moisture content for pine sapwood ($R^2=0.9770$), oak ($R^2=0.9977$) and teak ($R^2=0.9947$). The linear regression equations are found as $y = 0.00404x - 0.00451$ for pine sapwood, $y = 0.00598x - 0.00881$ for oak, and $y = 0.00606x + 0.01211$ for teak, where y is the SI and x is the MC expressed as percentage. The small offset found (<1%) in the equations for pine and oak tells us that a minimum moisture content should be present in order to obtain any signal of water. In case of teak, the contribution from an organic component for teak leads to a small positive offset.

4.3.2. The state of water in wood during water uptake and drying

NMR measurements with temporal and spatial resolution were performed during water uptake and drying of pine sapwood, oak and teak, to understand the moisture transport mechanisms in different wood types from softwood to hardwood. In this section, we focus on the state of water.

Water uptake

Moisture content profiles of pine sapwood during water uptake are given in Figure 4.10a. The surface in contact with the liquid water is located at position $x=0$. The FSP is indicated by horizontal dashed line. The profile prior to water uptake is flat and corresponds for a MC of about 6%, which was equilibrated at 33% RH. During the early phase of the uptake (first 2 days), a front develops indicating that the transport is internally limited. This front occurs until it reaches the bottom, where the MC remains below the FSP. Between 7 and 36 days, there is very little increase in the MC, which still stays around the FSP. After 114 days, the MC significantly exceeds the FSP.

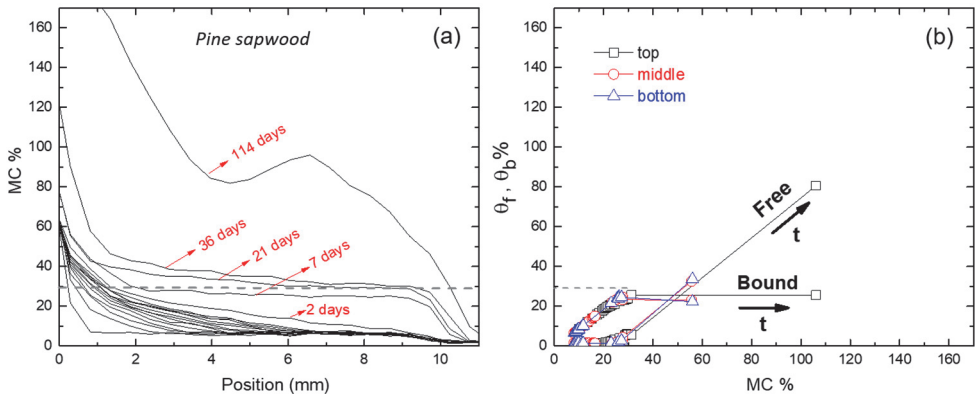


Figure 4.10. (a) The MC profiles of pine sapwood during water uptake for 114 days. The profiles are given every 2 h for the first day and at the indicated times. (b) Moisture fraction of free water, θ_f , and bound water, θ_b , versus total MC at 3 positions: around 2 mm (top), 5 mm (middle) and 8 mm (bottom) below the surface.

Besides the MC profiles, relaxation analysis is used to identify and quantify the state of water during water uptake. The relaxation analysis is performed at three different points, around 2 mm (top), 5 mm (middle) and 8 mm (bottom) below the surface, where it relates to a region of 0.5 mm width at each position. The plot of moisture fractions versus total MC at these three positions is given Figure 4.10b. It shows that there is only bound water at initial stages. First the cell walls are filled with bound water, irrespectively of the position. Only after the saturation of the cell walls, free water is observed.

Moisture content profiles of oak and teak during water uptake are given in Figure 4.11a&c. Similar to pine sapwood, a front immediately develops indicating that the transport is internally limited for both wood types.

Bound and free water distribution in wood during water uptake and drying as measured by 1D magnetic resonance imaging

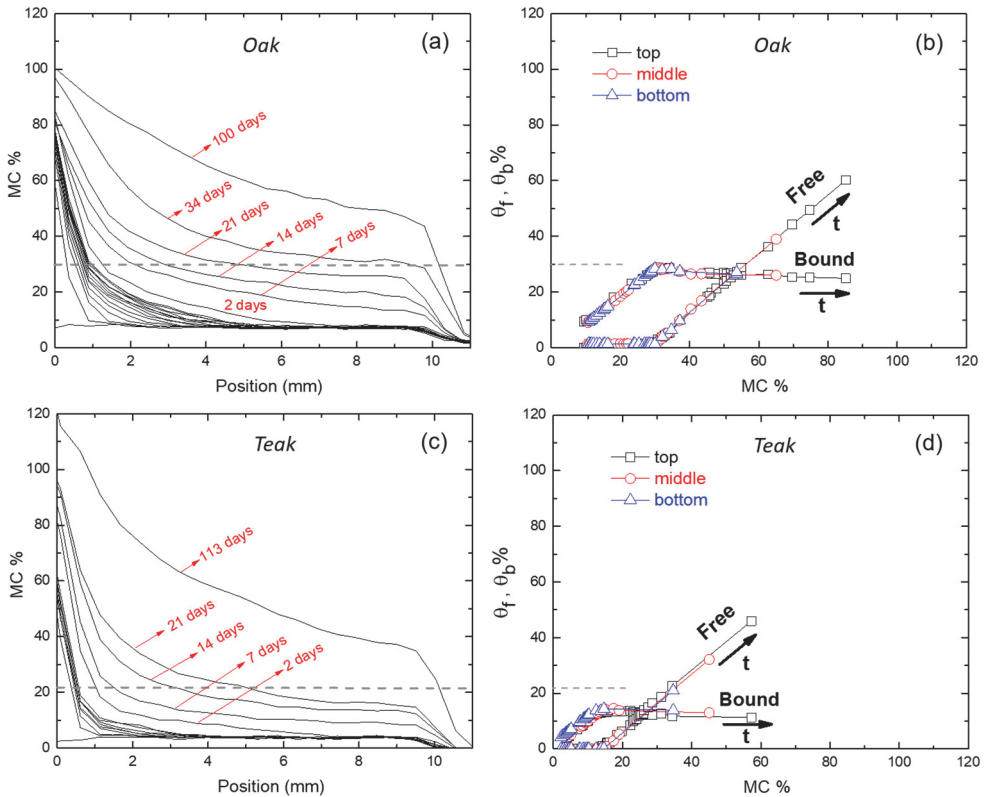


Figure 4.11. The MC profiles during water uptake of (a) oak, and (c) teak. The profiles are given every 2 h for the first day and at the indicated times. Moisture fraction of free water, θ_f , and bound water, θ_b , versus total MC for (b) oak, and (d) teak, at 3 positions: around 2 mm (top), 5 mm (middle) and 8 mm (bottom) below the surface.

The plots of moisture fractions versus total MC at three different positions for both oak and teak are shown in Figure 4.11b&d. At all positions, the bound water is first filled, and then free water is only observed after all the cell walls are saturated. The absence of free water before the cell wall saturation reveals a closed-pore system in all studied wood types. Since the fractions of bound and free water are dependent on the MC, intrinsically a thermodynamic equilibrium is set. Additionally for teak, the moisture fraction of bound water at full saturation of cell walls is around 15%, which is smaller than previously found FSP, 22%. It may result from the difference in the structure of this individual specimen, which differs from the average.

Drying

Moisture content profiles of pine sapwood during drying are given in Figure 4.12a. The surface exposed to dry air is located at position $x=0$. The FSP is indicated by the horizontal

dashed line. Initially, the wood was fully saturated by immersing the specimens in distilled water for at least one month, resulting in a homogeneous initial moisture distribution at about 160% MC. In Figure 4.12a, the time between each profile, Δt , is 7 h and the duration of the drying period, t , is 6 days. The profiles were obtained by time interpolation and smoothing over space and time using profiles measured every 103 min. After a fast initial decrease in the MC to 140%, an evaporation front develops inside the sample. The fast initial decrease in MC throughout the sample can be explained by the existence of continuous liquid paths throughout the wood sample ⁵⁷. When the continuity of the liquid phase is disrupted, liquid flow caused by capillary pressure is no longer possible. After this point, the moisture transport becomes internally limited, which results in the formation of an evaporation front.

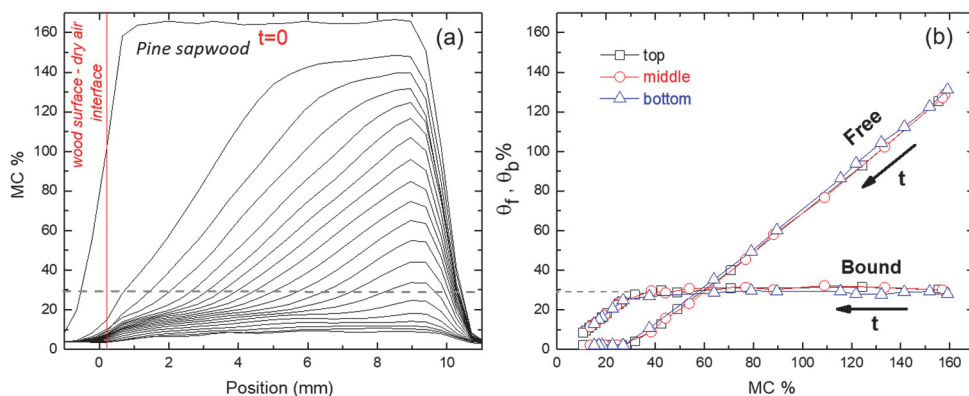


Figure 4.12. (a) The MC profiles of pine sapwood during drying; $\Delta t=7$ h, $t=6$ days. (b) Moisture fraction of free water, θ_f , and bound water, θ_b , versus total MC at 3 positions similar to water uptake, i.e. around 2 mm (top), 5 mm (middle) and 8 mm (bottom) below the surface.

Figure 4.12b shows the relaxation analysis, which is performed at three different points, similar to the water uptake analysis. At each position, the loss of bound water only starts just after all free water has vanished.

Moisture content profiles of oak and teak during drying are given in Figure 4.13a&c. For oak, the profile prior to drying is flat with a 120% MC. A quick initial decrease in the MC to 100% is observed that could be the result of evaporation of liquid water present in ray tracheids. Additionally, more uniform drying rather than a sharp evaporation front is observed. This could be explained by the fast internal redistribution of liquid water via the longitudinal tracheids and wood rays ⁵⁷. For teak, the profile prior to drying is flat with a 110% MC. Note that the time scale between two subsequent profiles is about three times more than that of pine sapwood and oak. Compared to the drying of pine sapwood and oak, the most visible difference is the absence of fast initial decrease in the MC. Immediately, a sharp evaporation front develops indicating internally limited transport.

Bound and free water distribution in wood during water uptake and drying as measured by 1D magnetic resonance imaging

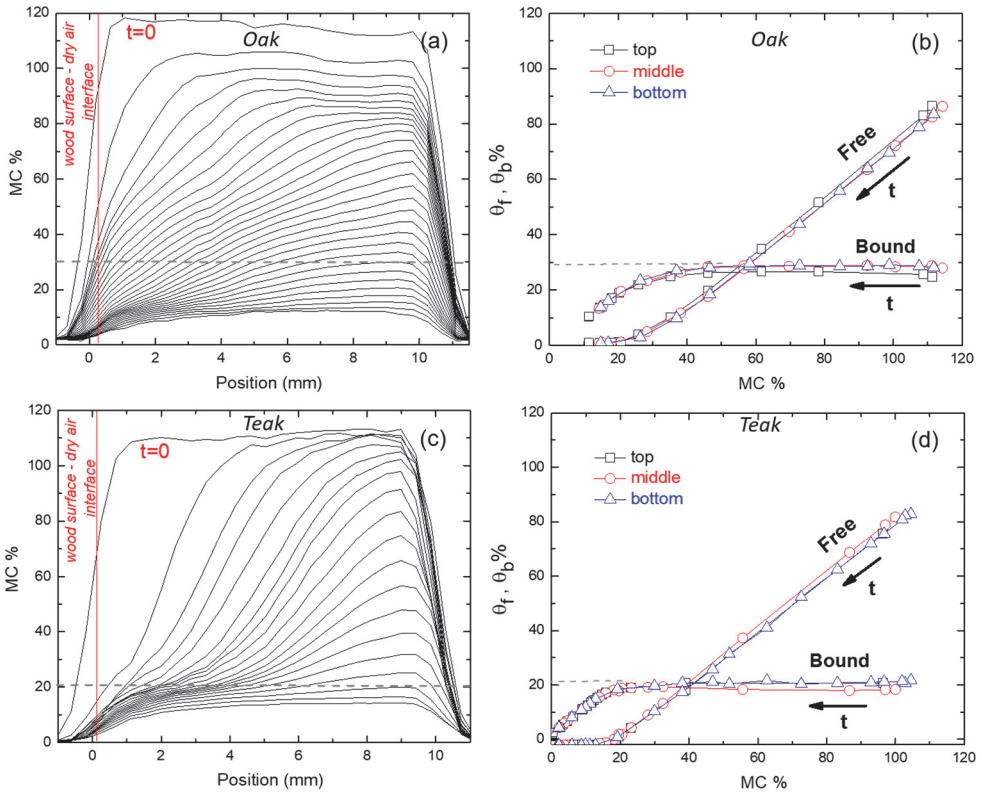


Figure 4.13. The MC profiles during drying of (a) oak; $\Delta t=6.8$ h, $t=8.5$ days, (c) teak; $\Delta t=22.4$ h, $t=18$ days. Moisture fraction of free water, θ_f , and bound water, θ_b , versus total MC for (b) oak, and (d) teak, at 3 positions: around 2 mm (top), 5 mm (middle) and 8 mm (bottom) below the surface.

The relaxation analyses at three different points are shown in Figure 4.13b&d for oak and teak. Similar to pine sapwood, at each position, the loss of bound water starts just after vanishing the free water.

The curves show that in uptake and drying, always the same sequence of filling/emptying is followed. Obviously, there is a unique coupling between the MC and the fractions of bound and free water.

4.3.3. Effective diffusion coefficient

To answer the question how water migrates through wood, we study the effective diffusion coefficient, D_{eff} , found from the uptake and drying experiments. Firstly, the derivation of D_{eff} will be explained. Secondly, the D_{eff} values will be calculated. Thirdly, the D_{eff} values will be interpreted to understand the dominant transport mechanism. Additionally, D_{eff} of the water uptake and drying will be compared.

Theory

The effective diffusivity can be determined directly from moisture profiles. One-dimensional moisture transport can be described by a non-linear equation¹³¹:

$$\frac{\partial \theta}{\partial t} = \frac{\partial}{\partial z} \left(D_{eff} \frac{\partial \theta}{\partial z} \right), \quad (4.2)$$

where θ is the moisture content, z is the position, t is the time and D_{eff} is the effective diffusivity. When the well-known Boltzmann transformation¹³² is applied:

$$\lambda = \frac{z}{\sqrt{t}}, \quad (4.3)$$

the non-linear diffusion equation reduces to a differential equation:

$$2 \frac{d}{d\lambda} \left(D_{eff} \frac{d\theta}{d\lambda} \right) + \lambda \frac{d\theta}{d\lambda} = 0, \quad (4.4)$$

In our case Equation 4.4 has the following initial and boundary conditions:

$$\theta = \theta_{\infty} \text{ for } \lambda \rightarrow \infty \text{ (} z > 0, t = 0 \text{)}, \quad (4.5)$$

$$\theta = \theta_0 \text{ for } \lambda = 0 \text{ (} z = 0, t > 0 \text{)}, \quad (4.6)$$

where θ_{∞} is the initial uniform moisture content of the sample and θ_0 is the boundary moisture content. $\theta_0 > \theta_{\infty}$ for water uptake, while $\theta_0 = 0$ for drying.

If D_{eff} is constant, Equation 4.4 has an analytical solution for the water uptake process given by:

$$\theta = \theta_0 - (\theta_0 - \theta_{\infty}) \operatorname{erf} \left(\frac{\lambda}{\xi} \right), \quad (4.7)$$

where ξ is defined as $\xi \equiv \sqrt{4D_{eff}}$.

In case of drying, $\theta_0 = 0$ in Equation 4.7, which leads to:

$$\theta = \theta_{\infty} \operatorname{erf} \left(\frac{\lambda}{\xi} \right). \quad (4.8)$$

Note that for small $\frac{\lambda}{\xi}$, $\operatorname{erf} \left(\frac{\lambda}{\xi} \right)$ can be approximated by $\frac{2\lambda}{\sqrt{\pi}\xi}$. As such Equation 4.8 can then be rewritten as:

$$\xi = \frac{2\lambda}{\sqrt{\pi}} \frac{\theta_{\infty}}{\theta}, \quad (4.9)$$

$$D_{eff} = \frac{\theta_{\infty}^2}{\pi} \left(\frac{\lambda}{\theta} \right)^2, \quad (4.10)$$

Experimental results

The Boltzmann transformation is applied for the moisture profiles for both uptake and drying experiments (until the front reaches the bottom, Figure 4.10 - Figure 4.13) and shown

in Figure 4.14. All the transformed profiles nicely overlap, except for the profiles of the oak drying experiment.

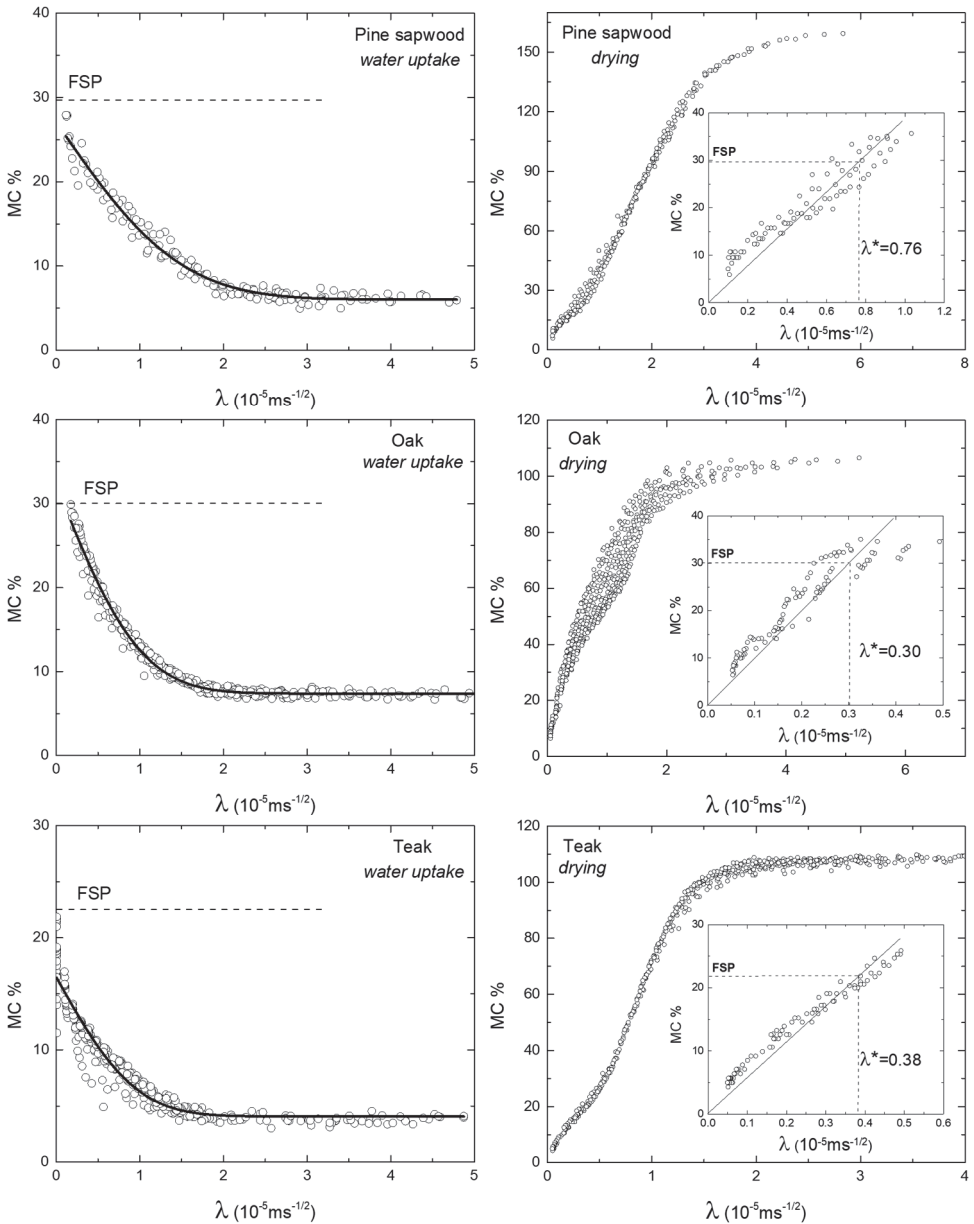


Figure 4.14. The profiles of the uptake and the drying after Boltzmann transformation. The graphs on the left column represents the water uptake, where the solid lines are the fitted error function, Equation 4.7, from which D_{eff} is obtained. The graphs on right column represents drying, where the linear approximation below FSP is given in the inset figures and D_{eff} is obtained by Equation 4.10.

The effective diffusion coefficients (D_{eff}) for the water uptake experiments are determined by fitting the transformed profiles with Equation 4.7. For drying Equation 4.10 is used. We take for λ and θ the values λ^* and θ^* at the moisture content at the FSP, which is shown in the insets on the right column of Figure 4.14. The diffusivity values are given in Table 4.3.

Table 4.3. D_{eff} values for pine sapwood, oak and teak for water uptake and drying as found from the Boltzmann transformed profiles.

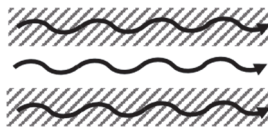
	D_{eff} (10^{-10} m ² /s)	
	Water uptake	Drying
Pine sapwood	0.68	5.2
Oak	0.26	0.35
Teak	0.25	1.2

Table 4.3 shows that drying is faster than the water uptake for all the studied wood types, which is about 8 times faster for pine sapwood, about 1.5 times for oak, and about 5 times for teak.

Interpreting the effective diffusivity

In order to have conceptual understanding of the transport mechanism, we evaluated two extreme diffusion models in terms of transport, and compared our experimental findings with the models. The models are assuming a good transport connectivity, and a poor connectivity, respectively. The derivation of these models is given in Appendix, and the basics of their foundation will be principally explained in the next subsection. A schematic presentation of both concepts is given in Figure 4.15.

Parallel diffusion in vapor phase and in the fibers



Series diffusion in vapor phase and in the fibers



Figure 4.15. Schematic presentation of the considered diffusion concepts for wood. The striped regions represent the cell wall fibers, while the blank regions represent the lumen or other void spaces.

Model 1: Parallel diffusion in vapor phase and in the fibers

In this case, it is assumed that the water vapor concentration in the lumen is in equilibrium with the cell wall moisture content (bound). The effective diffusion coefficient of the parallel model is estimated according to:

$$D_{eff} \text{ (parallel)} \approx D_v \left(\frac{\partial c_v}{\partial c_b} \right), \quad (4.11)$$

where D_v is the water vapor diffusion coefficient. The change in the molar density of water vapor in lumen, c_v , with respect to the change in the molar density of bound water, c_b , is expressed by the inverse slope of the sorption isotherms in Figure 4.6. Note that $D_v = D_{v,air}/\tau$, where τ is the tortuosity of wood for vapor. However, the tortuosity effect is not included in the calculation, since we aim to get an upper limit of D_{eff} by the parallel diffusion model. Additionally, as the lumen are rather straight, τ is not expected to exceed 2. The diffusivity values determined by Equation 4.11 for 12% RH (MC of about 3.5%) and 100% RH (MC of about 22% for teak, 30% for pine sapwood and oak) are given in Table 4.4.

Model 2: Series diffusion in vapor phase and in the fibers

The second model consists of series diffusion from wood cell to wood cell in vapor phase and in the fibers. The schematic representation of the model is given in Figure 4.15. Two points have to be kept in mind; (1) the bound water in the cell wall has a much higher concentration than the water vapor in lumen, (2) the diffusion of water vapor in lumen is much faster than the diffusion in the cell wall. The effective diffusion coefficient of the series model is estimated according to:

$$D_{eff} \text{ (series)} \approx \frac{D_b}{\varphi}, \quad (4.12)$$

where D_b is the bound-water diffusion coefficient and $\varphi \equiv L_b/L$. L_b is the length of the path for bound water, L_v is the length of the path for water vapor and L is the sum of them. φ is estimated based on the ratio of total moisture volume (in a fully saturated sample) per total volume of the sample. It is found as 0.16 for pine sapwood, 0.23 for oak and 0.31 for teak. The bound-water diffusion coefficient is taken from literature that it is aimed to get a lower limit of D_{eff} by the series diffusion model. There is hardly information available, so the bound water diffusion coefficient for *Picea sitchensis* is used, which is $0.4 \cdot 10^{-11}$ m²/s at MC of 8% and $3.2 \cdot 10^{-11}$ m²/s at MC of 28%¹²⁰. This diffusion coefficient is obtained by filling the lumens with a low-melting alloy of bismuth, lead, and tin. Considering these values, the diffusivity values calculated with Equation 4.12 are given in Table 4.4.

Table 4.4. Estimated theoretical diffusivity values for two diffusion models.

	D_{eff} (10^{-10} m ² /s)	
	Parallel	Series
Pine sapwood	8.5 – 34	0.25 – 2.0
Oak	4.0 – 23	0.17 – 1.4
Teak	8.6 – 2.8	0.13 – 2.8

The order of magnitude of theoretically derived diffusivity values from series model (Table 4.4) is closest to the order of magnitude of experimental results (Table 4.3) of both water uptake and drying. Therefore, the transport during water uptake and drying is better represented by the series model indicating that the diffusion in the cell wall fibers plays an important role.

4.4. Conclusions

It has been shown that NMR Imaging is a powerful method to determine the distribution and the concentration of water in wood, especially for understanding the water transport properties. A straightforward relation is obtained between the NMR signal and the moisture content. In contrast to weighing techniques, NMR relaxation analysis allows to identify the state of water within the wood, and to determine its order during wetting or emptied during drying. Based on this study, the following conclusions can be drawn, based on the studied wood types with the selected cut directions, regarding the water state and transport properties in pine sapwood, oak and teak during water uptake and drying:

1. The transport in all studied wood types is internally limited for both water uptake and drying. Internally limited means that the water movement is limited by water transport within the wood.
2. During water uptake, free water is observed only after the cell walls are filled with bound water at FSP. During drying of the water saturated samples, the loss of bound water starts just after free water is vanished, which has a transition point at FSP. Therefore, there is always local thermodynamic equilibrium of bound and free water during uptake and drying, i.e. the ratio between each state can always be found at any period.
3. The drying below FSP is faster than the water uptake for all studied wood types.
4. The transport during water uptake and drying is better represented by the conceptual model consisting of series diffusion from wood cell to wood cell in vapor phase and in the fibers. This indicates that the diffusion in the cell wall fibers plays an important role during both water uptake and drying.

4.5. Appendix

Observations with NMR are done in terms of moisture contents. Via uptake processes, an estimate of the diffusion coefficient is obtained. The appendix describes its interpretation.

Starting point is the non-linear diffusion equation:

$$\frac{\partial \theta}{\partial t} = \frac{\partial}{\partial z} D_{eff}(\theta) \frac{\partial \theta}{\partial z}, \quad (A1)$$

where θ is the moisture content, z is the position, t is the time and D_{eff} is the effective diffusion constant. It can be written also in term of molar densities, c :

$$\frac{\partial c}{\partial t} = \frac{\partial}{\partial z} D_{eff}(c) \frac{\partial c}{\partial z}. \quad (A2)$$

The question is how to come to a conceptual understanding of the effective diffusion coefficient. As water is either in the vapor phase (v) or in the fibers (bound, b):

$$c = c_v + c_b. \quad (A3)$$

Model 1: parallel diffusion in vapor phase and in the fibers

Differential equation for water vapor in lumen:

$$\frac{\partial c_v}{\partial t} = \frac{\partial}{\partial z} D_v \frac{\partial c_v}{\partial z} - i, \quad (A4)$$

Differential equation for bound water in the fibers:

$$\frac{\partial c_b}{\partial t} = \frac{\partial}{\partial z} D_b(c_b) \frac{\partial c_b}{\partial z} + i, \quad (A5)$$

where i is the rate of change between vapor and bound state, D_b is the bound-water diffusion coefficient, and D_v is the water vapor diffusion coefficient. Summation of Equations A4 and A5 result in:

$$\frac{\partial c}{\partial t} = \frac{\partial}{\partial z} \left(\frac{D_v}{1 + \partial c_b / \partial c_v} + \frac{D_b}{1 + \partial c_v / \partial c_b} \right) \frac{\partial c}{\partial z}, \quad (A6)$$

To arrive at Equation A2, we take the effective diffusion coefficient as:

$$D_{eff} = \frac{D_v}{1 + \partial c_b / \partial c_v} + \frac{D_b}{1 + \partial c_v / \partial c_b}. \quad (A7)$$

In case of water in wood: $c_v \ll c_b$ and therefore $\partial c_v / \partial c_b \ll 1$ (the water vapor density is low). As a consequence:

$$D_{eff} \approx D_v \frac{\partial c_v}{\partial c_b} + D_b. \quad (A8)$$

As diffusion in the fibers is much smaller compared to vapor diffusion, further simplification is possible:

$$D_{eff} \approx D_v \left(\frac{\partial c_v}{\partial c_b} \right). \quad (A9)$$

Note that $D_v = D_{v,air}/\tau$ where τ is the tortuosity of wood for vapor, considered to be 2 at most.

$$D_{v,air} = 2.4 \cdot 10^{-5} \text{ m}^2/\text{s at } 20^\circ\text{C}.$$

Model 2: series diffusion in vapor phase and in the fibers

In case of diffusion from wood cell to wood cell, chained in series, we can write the local molar fluxes for bound water in the cell wall fibers and vapor in the lumen as:

Locally the molar fluxes obey:

$$J_b = -D_b \frac{\partial c_b}{\partial z} = -D_b \left(\frac{\partial c_b}{\partial c_v} \right) \frac{\partial c_v}{\partial z}, \quad (A10)$$

$$J_v = -D_v \frac{\partial c_v}{\partial z}. \quad (A11)$$

In a steady-state situation and in case of small gradients, the total flux being the sum of Equations A10 and A11, can be written as:

$$J \equiv -D_{eff} \frac{\Delta c}{L} = -D_{eff} \left(1 + \frac{\partial c_b}{\partial c_v} \right) \frac{\Delta c_v}{L}. \quad (A12)$$

Further it can be derived that:

$$\Delta c_v = -J \left[\frac{L_b}{D_b \partial c_b / \partial c_v} + \frac{L_v}{D_v} \right], \quad (A13)$$

where L_b is the length of the path for bound water, L_v is the length of the path for water vapor and L is the sum. In case we define $\varphi \equiv L_b/L$, the combination leads to:

$$D_{eff} \left(1 + \frac{\partial c_b}{\partial c_v} \right) = \frac{1}{\varphi / D_b (\partial c_b / \partial c_v) + (1 - \varphi) / D_v}. \quad (A14)$$

As diffusion in the fibers is much smaller compared to vapor diffusion, $D_b \ll D_v$, and in case of low vapor density, $c_v \ll c_b$:

$$D_{eff} = \frac{D_b}{\varphi}. \quad (A15)$$

Chapter 5

Understanding the influence of wood as a substrate on the permeability of coatings by NMR imaging and wet-cup

An important reason to apply coatings on wood is to protect wood against moisture. As a result of regulations and ecological concerns, there has been a shift towards waterborne coatings, which make coatings intrinsically more sensitive to water. As a consequence of the higher sensitivity to water, the durability of both wood and coatings can be negatively affected. In order to use waterborne coatings for woodcare, the main factors influencing transport through these coatings have to be understood. The aim of this study is to elucidate the influence of the wooden substrate on the water permeability of the coating applied to it. Pine sapwood, oak and teak were selected as the wood types, covering a whole range of low to high density wood. Three types of coatings were formulated: a solventborne alkyd, a waterborne alkyd and a waterborne acrylic. NMR imaging was used to measure the moisture distribution and quantify the changes in bound and free water in coated wood during drying. For all wood-coating combinations that were investigated, water transport appeared to be externally (i.e. coating) limited. The loss of bound water started only after evacuation of free water, which showed a local thermodynamic equilibrium associated with bound and free water. We furthermore compared water permeability of free films and wood supported films to understand the influence of the wood-coating interactions. The permeability of free coating films has been determined by the wet-cup method, followed by investigating the solubility and diffusion of water in order to understand the differences in the permeability. We found that the interaction of the coating with the wood has no influence on the water permeability for the considered combinations. Furthermore, the permeability is largely determined by the water solubility.

This chapter has been published as

Ö. Gezici-Koç et al., *Progress in Organic Coatings* 114: 135-144 (2018).

5. Understanding the influence of wood as a substrate on the permeability of coatings by NMR imaging and wet-cup

5.1. Introduction

Wooden products are found everywhere, e.g. furniture, cladding on houses or floors. Wood is a hygroscopic and porous material, which in many situations undergoes fluctuations in moisture content due to periodic water absorption and desorption. A high moisture content, such as in condensing environments, may result in durability loss due to fungal growth. Consequently, coatings are widely applied on wooden substrates for protective and decorative reasons, and to prolong the service life if they are maintained correctly. Poorly maintained coatings can even decrease the service life. The regulations on volatile organic compounds (VOCs) have led to increased use of waterborne (WB) coatings, which are more sensitive to water compared to solventborne (SB) coatings³⁹. Since protection is one of the main properties claimed for coatings, obtaining knowledge on how a coating resists water is helpful in predicting the service life of the substrate and the coating.

Previously, water transport properties through coatings have been investigated by measuring the average moisture content in bulk wood^{39–41}. Many studies have demonstrated the inhomogeneous distribution of water close to the surface^{42–45}. Therefore, the barrier properties of coatings should be re-evaluated by monitoring the moisture content with spatial and time resolution. The influence of two coating systems and their barrier effect against water diffusion in spruce wood have been investigated by Sonderegger et al.¹³³ with the neutron imaging method, where the moisture gradient through the wood specimens was determined at different times during water uptake. However, the neutron imaging method does not give information on the state of moisture as bound (in cell wall) or free (in lumen or other void spaces) water. It is recognised that such identification of the state of water within wood^{108,134}, during uptake or drying by common experimental techniques like weighing^{57,135}, X-ray computer tomography (CT)⁵⁸ or neutron radiography⁵⁹ remains a challenge.

Nuclear Magnetic Resonance (NMR) imaging has proven to be an excellent tool for determining the moisture content of wood samples during water sorption^{134,136}. Combining NMR imaging with relaxometry allows for characterizing the state of moisture as bound or free water¹³⁴. It is a non-invasive method that provides temporally and spatially resolved moisture profiles⁵⁶. NMR imaging was also applied to study the distribution and penetration of oil in wood, in which the oil was used as water repellent for wood preservation¹³⁷. It has been used to determine the distribution of water in coated wood mostly during absorption/uptake^{44,45,55}. Van Meel et al.⁴⁴ showed that the moisture permeability depends on the specific combination of wood and coating, since the coating influences the moisture sorption of wood in different ways. They found that the water absorption of a hardwood dark red meranti only occurs via diffusion through the solid matrix. In their study,

application of a WB acrylic coating had no influence on this absorption process, which was attributed to the large water uptake of the coating. On the other hand, a WB coating does reduce the water uptake of pine by preventing capillary water uptake where pine - in contrast to meranti⁴⁴ - contains relatively large and highly permeable pores. A coating may also reduce the drying rate of wood, but there is very limited work done on coated wood during desorption/drying by NMR⁴². In situ determination of local moisture content for uncoated wood has been achieved by portable NMR devices^{109,110}. Moreover, the protective properties of wood coatings against moisture migration were evaluated and compared with the use of a portable NMR sensor⁴³. However, the penetration depth with portable NMR devices is limited up to few millimetres.

The performance of coatings depends on many factors, of which the wood-coating interface is a crucial one. Microscopic tools, which differ in imaging capabilities, have been most widely applied to examine wood-coating interfaces^{138,139}. A comparative study on confocal laser scanning microscopy (CLSM) and light microscopy (LM) to image the interface between *P. radiata* wood and clear coating showed that CLSM is superior to LM¹⁴⁰. CLSM can resolve wood-coating interfaces more clearly and provides more information on the physical nature of interaction between the coating and the wood surface¹⁴⁰. In this work, we used LM to determine the effective thickness of the dried coating layer, and get information on which depths the applied coatings penetrated the wood samples. Instead of focusing on the physical aspects of wood-coating interactions, we will investigate the influence of wood-coating interactions on the permeability of coatings by comparing the free films and wood supported films.

The aim of this study is to elucidate the influence of the wooden substrate on the water permeability of the coating applied to it. NMR imaging was used to measure the moisture content distribution and quantify the changes in bound and free water in wood (pine sapwood, teak and oak) as a function of coating permeability (SB alkyd, WB alkyd and WB acrylic) during drying of completely water saturated samples. NMR moisture profiles were used to calculate the decrease in average moisture content in order to determine the permeability of coatings on wood. The permeability of free coating films was determined by the wet-cup method, followed by comparison with the permeability of wood supported films.

5.2. Materials and methods

5.2.1. Wood and coating types

Three types of wood were studied: pine sapwood, oak and teak, which are commonly used in Central Europe for outdoor applications, such as furniture, cladding on houses or floors. The properties of these wood types were given in detail in a previous study¹³⁴ (Chapter 4) and summarized in Table 5.1.

Table 5.1. Selected wood types and their general characteristics.

Wood type	Softwood/hardwood	Density (kg/dm ³)	Structure	Ring width (mm)
Pine sapwood (<i>Pinus</i>)	Softwood	~ 0.54	No vessels	~ 1.4
Oak (<i>Quercus petraea</i>)	Hardwood	~ 0.64	Ring porous	~ 1.4
Teak (<i>Tectona grandis</i>)	Hardwood	~ 0.64	Semi-ring	~ 1.2

Due to increased use of WB coatings, as a result of the regulations on volatile organic compounds, two types of waterborne (WB) coating and one solventborne (SB) coating as a reference were studied to gain knowledge of how coatings resist water. Three transparent coating formulations, WB acrylic, WB alkyd, and SB alkyd, were prepared by AkzoNobel Decorative Paints, Sassenheim, the Netherlands, specifically for this work. The WB acrylic dispersion was based on butyl acrylate and methyl methacrylate, with a glass transition temperature (T_g) of 2.4 °C and a minimum film formation temperature of 7 °C. The final WB acrylic composition had a solid content of 35 wt. (weight) %, and the surfactant amount of 6.9 wt.% on solid content. The alkyd binder for both WB and SB compositions was based on tall-oil fatty acids with a long oil length and low molecular weight. The WB alkyd emulsion was prepared using a 2% load of non-ionic surfactant to obtain an average particle size of 200 nm. The final WB alkyd composition had a solid content of 35 wt.%, and the surfactant amount of 5.1 wt.% on solid content. The final SB alkyd formulation had a solid content of 65 wt.%. As addition of driers, the alkyd formulations (both WB and SB) contain Co alternatives. Mn-based drier is used in SB alkyd, and Fe-based drier is used in WB alkyd. Although the same alkyd binder used in both formulations, selecting different drier depends on achieving a stable formulation and a proper drying after careful optimization. For example, Mn gives separation problems if it is used in WB alkyd emulsion. When Fe is used in SB alkyd, it does not give a proper drying, which results in wrinkling.

5.2.2. Coatings on wood

The coatings (WB Acrylic, WB alkyd, SB alkyd) were applied by brush on wood (pine sapwood, oak, and teak). The overview of studied wood-coating combinations is given in Table 5.2.

In all combinations, three layers were applied to achieve a final effective thickness of around 50 µm on wood. The first layer was sanded to eliminate surface roughness. Two more subsequent layers were applied. The time between the applications of consecutive layers was one day. The coated wood samples were dried at room condition, i.e. 21 °C and 40%

relative humidity, for at least four months before the measurements were performed. Note that the effect of aging the coated wood samples on the water transport properties was not studied, which is beyond the scope of this study. All measurements were performed on unaged coatings.

Table 5.2. Overview of studied wood-coating combinations.

Wood type	Coating type	Coating properties	Applied on
Pine sapwood (<i>Pinus sylvestris</i>)	SB alkyd	Solid Content: 65 wt.%	Radial plane: the rays are parallel and the growth rings are perpendicular to the coated surface
	WB alkyd	Solid Content: 35 wt.% Surfactant: 5.1 wt.% on solids	
	WB Acrylic	Solid Content: 35 wt.% Surfactant: 6.9 wt.% on solids	
Teak (<i>Tectona grandis</i>)	SB alkyd	Solid Content: 65 wt.%	Tangential plane: the growth rings and rays are oriented diagonally (about 45 ° angle) to the coated surface
	WB alkyd	Solid Content: 35 wt.% Surfactant: 5.1 wt.% on solids	
	WB Acrylic	Solid Content: 35 wt.% Surfactant: 6.9 wt.% on solids	
Oak (<i>Quercus petraea</i>)	SB alkyd	Solid Content: 65 wt.%	Tangential plane: the growth rings and rays are oriented diagonally (about 45 ° angle) to the coated surface
	WB alkyd	Solid Content: 35 wt.% Surfactant: 5.1 wt.% on solids	Tangential plane: the rays are perpendicular and the growth rings are parallel to the coated surface
	WB Acrylic	Solid Content: 35 wt.% Surfactant: 6.9 wt.% on solids	

In all combinations, three layers were applied to achieve a final effective thickness of around 50 µm on wood. The first layer was sanded to eliminate surface roughness. Two more subsequent layers were applied. The time between the applications of consecutive layers was one day. The coated wood samples were dried at room condition, i.e. 21 °C and 40% relative humidity, for at least four months before the measurements were performed. Note that the effect of aging the coated wood samples on the water transport properties was not

studied, which is beyond the scope of this study. All measurements were performed on unaged coatings.

The coatings were applied on the radial plane for pine sapwood and on the tangential plane for oak and teak. The direction influences the coating penetration characteristics¹³⁸. In the case of coated pine sapwood for all 3 types of coating, the rays are parallel and the growth rings are perpendicular to the coated surface. In the case of coated teak for all 3 types of coating, the growth rings and rays are oriented diagonally (about 45 ° angle) to the coated surface, but perpendicular to each other. In the case of coated oak, the orientation of the growth rings and rays is different between samples. In the early-wood rings of oak, there are big pores, i.e. vessels (~300 μm), which is shown with the CT image in Figure 5.1, as also explained in a previous study¹³⁴ (Chapter 4).

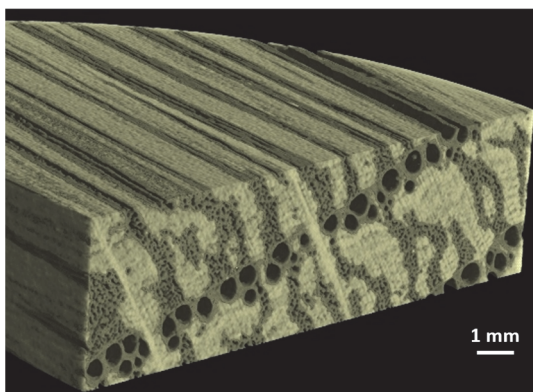


Figure 5.1. The computed tomography (CT) image of oak wood.

For SB alkyd coated oak, the growth rings and rays are oriented diagonally (about 45 ° angle) to the coated surface, i.e. there are vessels on the surface aligning into the wood with about 45 ° angle. For WB acrylic and WB alkyd coated oak, the rays are perpendicular and the growth rings are parallel to the coated surface, i.e. vessels are oriented parallel to the surface.

The dry film thickness of coatings on wood was determined from the cross-sections of the samples by using light microscope (Leica DMRX) according to ISO 2808:2007¹⁴¹ and ISO 1463:2003¹⁴². Firstly, 20 mm diameter cylindrical samples were drilled from 10 mm thick coated wood panels. The samples were fixed on a small piece of wood with epoxy glue for better handling. The cross-sections were made with a sledge microtome by cross cutting them with a sharp microtome knife. The cross-sections were examined with a light microscope using UV-light, where the investigated length was approximately 12 mm. The thickness analysis was based on measuring 10 different points for each sample.

5.2.3. NMR imaging and relaxometry

5.2.3.1. Principles and settings

NMR imaging and relaxometry was used to measure the moisture content distribution and to quantify the changes in bound and free water in coated wood.

The NMR principle is based on exciting the magnetic nuclei, in our case hydrogen nuclei, placed in a magnetic field by a radio frequency (RF) pulse and detecting the induction in an RF coil. The resonance frequency, f , of the magnetic nuclei depends on the magnitude of the applied magnetic field, \vec{B} , according to $f = \gamma |\vec{B}|$, wherein γ is the gyromagnetic ratio ($\gamma = 42.58$ MHz/T for hydrogen nuclei). In order to obtain spatial information, the resonance frequency is varied with position according to $f = \gamma(B_0 + zG_z)$, wherein G_z represents the linear magnetic field gradient in the z -direction, and \vec{B}_0 is the main magnetic field in the z -direction. The NMR signal gives information on the mobility of the magnetic nuclei, in our case hydrogen nuclei, next to giving the density (concentration) of these nuclei. As the water molecules (i.e. the hydrogen containing molecules) inside the pores are excited by an NMR pulse, diffusion causes random collisions between the water molecules and the pore walls, which in turn causes relaxation, T_2 , which describes the decay of the NMR signal. T_2 is related to local mobility, i.e. T_2 is longer when freely moving water molecules are in bulk water or shorter when their mobility is restricted by a small volume¹³⁴.

The experiments were performed with a home-built NMR set-up. It was designed with an electromagnet from GMW (Model 3473-70) and RadioProcessor™ (USB board) from SpinCore as a digital system for RF signal acquisition, detection and processing. We developed programs in MATLAB to record NMR data and to handle a gross amount of data for fitting and extracting parameters.

A main magnetic field of 0.75 T was used with a constant gradient of 418 mT/m in the z -direction, i.e. parallel to \vec{B}_0 . In the experiments, the center of the sample was aligned at the isocenter of the magnet. Slice selection was achieved by turning on a linear magnetic field gradient, G_z , while applying an excitation pulse that allows rotating the spins which are located in a slice within the sample. A Hahn Spin Echo (HSE) sequence, $\alpha_x^\circ - \tau - 2\alpha_y^\circ - \tau - \text{echo} - \tau$, was used to obtain the hydrogen density profiles where α is the flip angle and nominally equals 90° with a pulse time of 25 μs . A Carr-Purcell-Meiboom-Gill (CPMG) sequence, $\alpha_x^\circ - \tau - [2\alpha_y^\circ - \tau - \text{echo} - \tau]_n$, was used to measure the relaxation time at several points through the whole sample. n is the number of echoes. The interecho time ($t_e = 2\tau$) used in the experiments equals 200 μs while the recording window (t_{ww}) to measure the echo has a duration of 120 μs . The resulting NMR signal displays an exponential decay, as described by:

$$I(\tau) = \sum_{i=1}^m I_i \exp\left(-n \cdot 2\tau / T_2^i\right), \quad (5.1)$$

where $I(\tau)$ is the observed NMR signal at a time, I_i is the signal from each exponential component, and m is the number of components. The signal intensity of each exponential term is proportional to the pore volume^{123,143}. Therefore, the signal intensity of each term versus T_2 values produces a continuous spectrum of T_2 values, i.e. a map of the volume occupied by each pore size or the pore size distribution.

The peak maximum value is taken for the relaxation time determination¹³⁴.

The settings are summarized in Table 5.3. Δx is the theoretical spatial resolution, n_{avg} is the number of signal averages, and t_{RT} is the repetition time between two subsequent pulses.

Table 5.3. The measurement settings of Hahn Spin Echo (HSE) and Carr-Purcell-Meiboom-Gill (CPMG) pulse sequences used for drying of coated wood for all studied wood-coating combinations.

	t_e (μ s)	t_{ww} (μ s)	t_{90° (μ s)	G_z (mT/m)	Δx (mm)	n	n_{avg}	t_{RT} (s)
HSE	200	120	25	418	0.46	-	4	8
CPMG	200	120	25	418	0.46	2048	32	8

The measured signal profiles are divided by the signal profile of a homogeneous reference sample (same volume) allowing the local hydrogen density to be determined. As a reference sample, an aqueous 0.01 M CuSO₄ solution was used.

5.2.3.2. Samples and sample holder for drying of coated wood

20 mm diameter cylindrical samples were drilled from 10 mm thick coated wood panels. Prior to the drying measurements, all samples were saturated until their maximum MC - about 160% MC for pine sapwood, and about 110% MC for teak and oak - was reached. This was achieved by immersing the specimens in distilled water for at least one month. For saturation, the specimens were exposed to water from all sides, and full saturation was checked for (resulting in a homogeneous moisture distribution at the maximum MC) before the drying experiments were carried out. Teflon sample holders were used, which were described in our previous work¹³⁴ in Chapter 4. These holders were designed to seal the sides of the sample, to secure that water can only leave the wood through the coating. Dry air was blown over the top of the sample holder. The air flow was set at 3 L/min with an RH of about 0-5% at room temperature (~22 °C).

5.2.4. Free films

Free films were prepared by applying the coatings on polypropylene substrates (ASTM D4708-12¹⁴⁴). Application was performed in laminar flow cabinet to minimize the presence of dust and fibers in the film. For WB and SB alkyd coatings, two layers were applied with a wet layer thickness of 130 μ m for WB alkyd and 80 μ m for SB alkyd for each layer,

respectively. The time between the applications of consecutive layers was one day. For WB acrylic, one layer was applied with a wet layer thickness of 200 μm .

Similar to coated wood, free films were also dried at room condition, i.e. 21 $^{\circ}\text{C}$ and 40% relative humidity, for at least four months before the measurements were performed. Note all measurements are done on unaged coatings. Final properties of free films, i.e. dry film thickness, T_g and crosslink density, were measured by Differential Scanning Calorimetry (DSC) and Dynamic Mechanical Analysis (DMA) on 5-month dried samples, which are summarized in Table 5.4. The presented results are based on one sample measurement for each type.

Table 5.4. Typical characteristics of 5-month dried coating films.

		DSC	DMA	
	Dry film thickness (μm)	T_g ($^{\circ}\text{C}$)	T_g ($^{\circ}\text{C}$)	Crosslink density (mmol/cm^3)
WB acrylic	53	0.45	21.8	No crosslinking
WB alkyd	56	-18.7	5.7	0.18
SB alkyd	76	-8.6	17.2	0.33

DSC was performed by TA Instruments Q2000 model. The samples were placed in aluminium DSC pans with an initial weight of 4.5-7.5 mg. Spectra were recorded from -60 to +90 $^{\circ}\text{C}$ with a rate of 5 $^{\circ}\text{C}/\text{min}$. DMA was performed by TA Instruments RSA III model. The measurements were carried out under the film-tension mode in an appropriate range of -30 to +150 $^{\circ}\text{C}$ (5 $^{\circ}\text{C}$ stepwise) at a frequency of 1.66 Hz and an increasing strain amplitude from 0.03% to the value between 0.9-4 % depending on the sample. The tests were conducted using rectangular films specimen of 15.0 x 6.0 mm. The temperature corresponding to the peak value of $\tan \delta$ vs temperature curve has been taken as the glass transition temperature. From the storage modulus E' vs temperature curve, the lowest E' value above T_g was used to calculate the crosslink density¹⁴³.

5.2.5. Dynamic Vapor Sorption (DVS)

The equilibrium moisture sorption of all free films were analysed using a Dynamic Vapor Sorption (DVS) instrument (Q5000 SA from TA Instruments). The measurements were performed at a constant temperature of 25 $^{\circ}\text{C}$ with an initial sample weight of 1.5-3.0 mg. Weight changes were determined with a thermobalance (weight accuracy of 0.1% and signal resolution of 0.01 μg). Samples were initially dried for 10 h at RH of 10%. The RH was then increased from 10% to 98% (in 10% steps from 10% to 90%, and 4% steps from 90% to

98%), and subsequently decreased in similar steps until 0%. For all RH steps, the instrument was run in a dm/dt mode (mass variation over time variation) to detect when equilibrium was reached.

5.2.6. Wet-cup method

The water permeability of transparent wood coatings were determined by wet-cup measurements (ASTM E96 / E96M-16¹⁴⁵) on the free films. Glass cups with an area of 1.3 cm² were filled with distilled water to the half of the cup and sealed with free films. Note that the relative humidity inside the cups was 100%. The cups were put into the desiccators with various humidity conditions (33%, 43%, 53%, 65%, 75%, 85%, 93% and 97%) at room temperature (~ 22 °C). Saturated aqueous solutions of various salts were used to create the proper relative humidity in each desiccator. Thickness measurements were obtained with a digital gauge at a minimum of three positions on each film. The standard deviation of thickness for each film was typically less than 10%. The mass of water lost from the cup was monitored as a function of time.

5.3. Results and discussion

5.3.1. Uncoated wood versus coated wood

In order to understand the barrier properties of coatings against moisture, we first compare uncoated and coated wood. Uncoated and SB alkyd coated teak were chosen as an example of comparison, for which the moisture content (MC) profiles during drying are given in Figure 5.2.

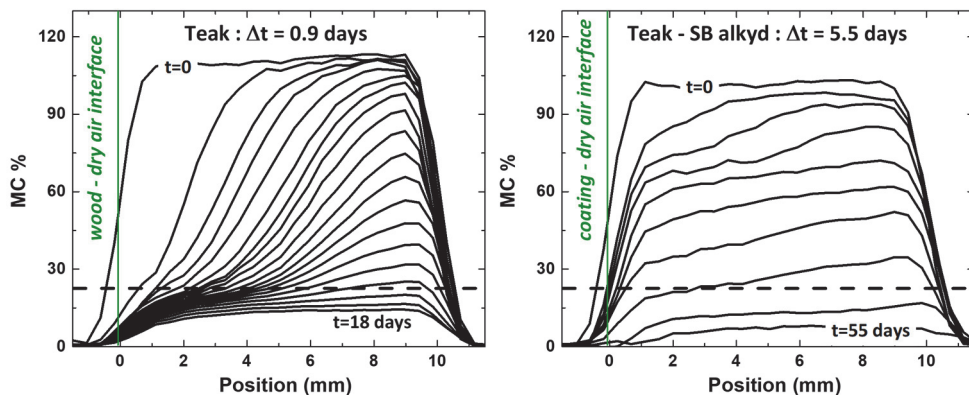


Figure 5.2. The moisture content (MC) profiles during drying of uncoated and SB alkyd coated teak. The data for uncoated teak is obtained from our previous study¹³⁴ in Chapter 4. The time between each profile is given by Δt and the duration of the drying by t .

The MC is determined by the measured NMR signal based on calibration done in our previous study¹³⁴ (Chapter 4) and expressed as a percentage of the mass of water over the mass of dry wood. In Chapter 4, we discussed the water transport properties in uncoated

wood during drying ¹³⁴, which we will use as a reference in this study. The surface exposed to dry air is located at position $x=0$. Note that the sample thickness is about 10 mm which can be read from the full width of the curve at half maximum. The Fiber Saturation Point (FSP) is indicated by the/a horizontal dashed line. In our previous study in Chapter 4, the FSP was found to be around a MC of 29% for pine sapwood, 30% for oak and 22% for teak with DVS, which were confirmed by gravimetrically determined sorption isotherms ¹³⁴. Initially, both uncoated and coated wood were completely water saturated. The profiles were obtained by interpolating in time and smoothing over space and time using profiles measured every 103 min.

Firstly, a sharp evaporation front develops for uncoated wood, while the water remains homogeneously distributed in coated wood. The transport in uncoated wood is internally (i.e. wood) limited ¹³⁴, while it is externally (i.e. coating) limited in coated wood. Secondly, the total drying time to reach a MC below 15% is around 18 days for uncoated teak, while it is around 55 days for SB alkyd coated teak. The total drying time is increased 3 times when it is coated.

5.3.2. Combinations of wood and coatings types

The barrier properties of wood coatings against moisture are investigated by studying various combinations of wood and coating types during drying, of which the moisture content profiles are given in Figure 5.3. The results are based on the measurements on one sample for each combination, which represent the typical plots for the studied wood-coating combinations.

For the combinations of 3 different wood types (pine sapwood, teak and oak) and 3 different coating types (SB alkyd, WB alkyd and WB acrylic), we observe homogeneous profiles during drying. It reveals coating limited transport regardless of any combination. In Chapter 4, we demonstrated the wood limited transport for these studied wood types during drying when they were uncoated ¹³⁴.

For coated pine sapwood, moisture peaks – each covering a region about 1 mm – are observed just below the wood-coating interface and at the bottom of the samples. During the preparation of wood panels from wood logs, cutting may destroy the cells on the surface, which may result in a different free water capacity for surface cells as compared to the inner part of the wood samples. Since pine sapwood is a low density wood compared to oak and teak, it may have the aforementioned damage on the surface cells, while the others do not.

For oak, a uniform distribution of moisture is observed for SB alkyd, whereas non-uniform (wave-like) moisture distribution is observed for WB alkyd and WB acrylic. This is because of the orientation of the vessels to the surface ¹⁴⁶. The vessels in the early wood rings have a different water capacity compared to the cells in the latewood rings. When these vessels

are oriented diagonally to the surface, such as in the case of SB alkyd, the influence of these regions with different water content is averaged, and uniform MC distribution is observed. When these vessels are oriented parallel to the surface, such as in the case of WB alkyd and WB acrylic, lower MC is observed in these regions, which leads to a non-uniform MC distribution through the wood samples.

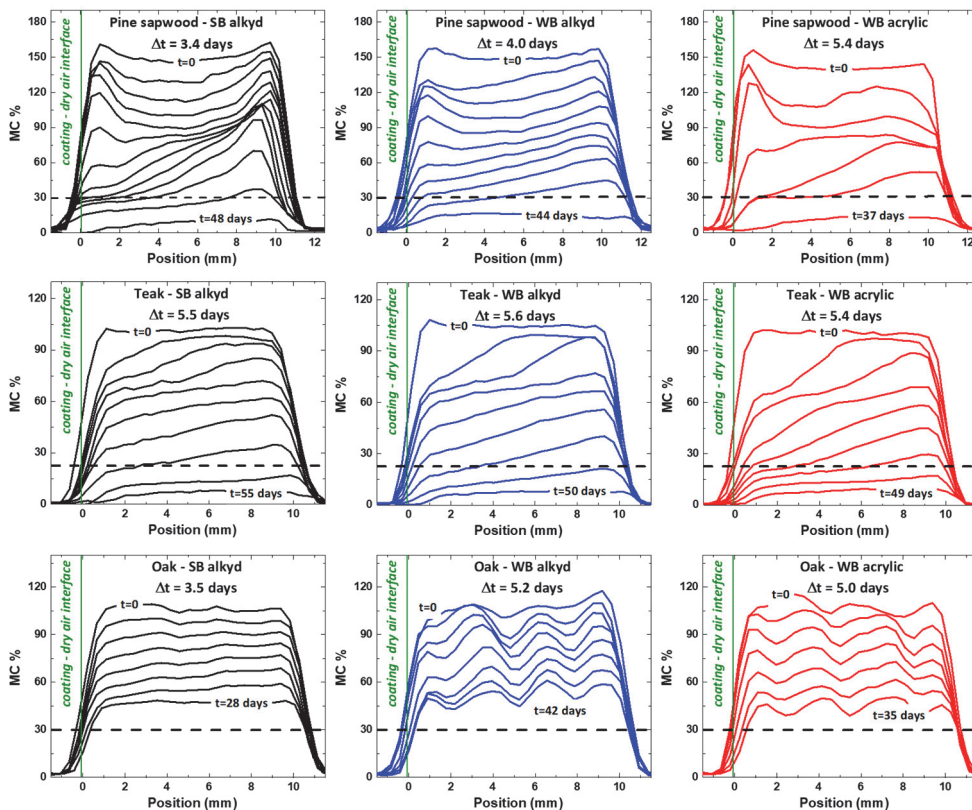


Figure 5.3. The moisture content (MC) profiles of various combinations of wood (pine sapwood, teak and oak) and coating (SB alkyd, WB alkyd and WB acrylic) types during drying. The time between each profile is given by Δt and the duration of the drying by t .

Besides the MC profiles, relaxation analysis is used to identify and quantify the state of water during drying, shown in Figure 5.4. From the continuous spectrum of T_2 values, the peak maximum value is taken for the relaxation time determination. The area under the peak is proportional to the volume occupied by each component, which is then used to calculate moisture fractions (θ) of bound and free water¹³⁴. The relaxation analysis is performed at three different points, around 2 mm (top), 5 mm (middle) and 8 mm (bottom) below the surface, where it relates to a region of 0.5 mm width at each position.

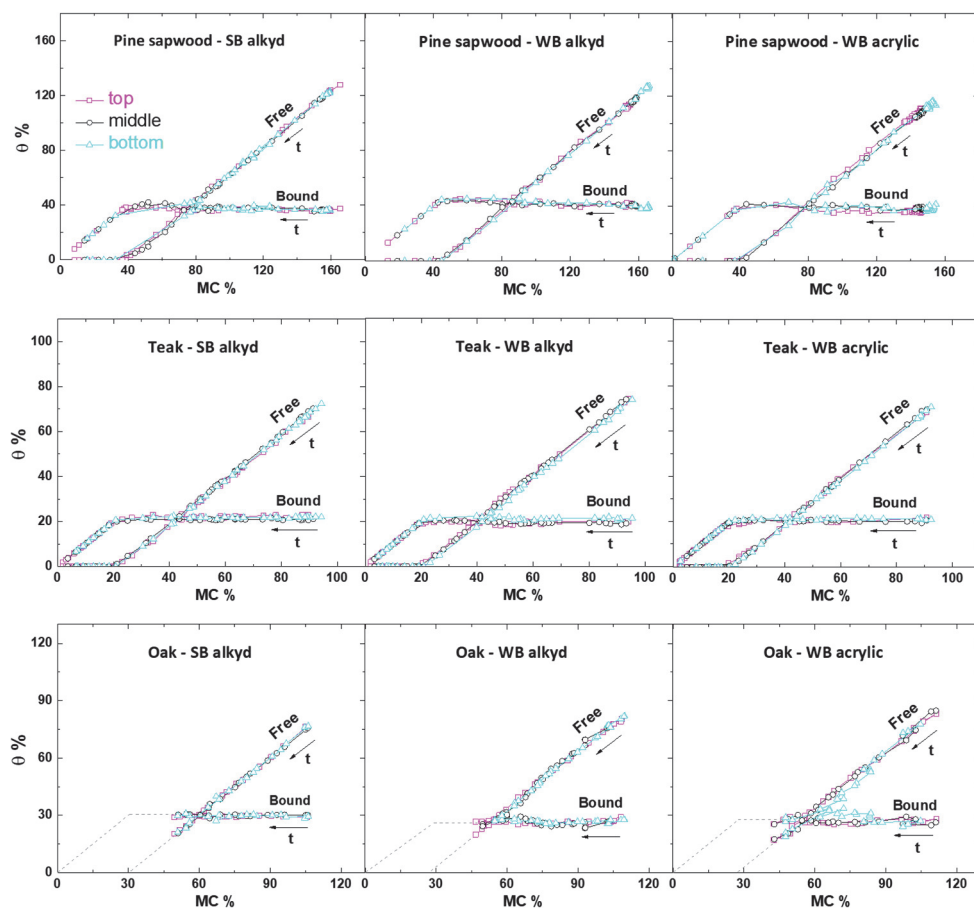


Figure 5.4. Moisture fractions (θ) of free and bound water versus total MC at 3 positions; around 2 mm (top), 5 mm (middle) and 8 mm (bottom) below the surface. For coated oak, the dashed lines are estimated paths for free and bound water.

Like uncoated wood, at each position, the loss of bound water starts just after the free water vanishes. Regardless of any combination, there is always a local thermodynamic equilibrium of bound and free water, i.e. the ratio between each state can always be found at any period.

5.3.3. Permeability of coatings

We investigate the influence of wood-coating interactions on the permeability of coatings by comparing the free films with each other as well as with wood supported films. The water permeability of transparent coatings on wood has been determined using the NMR profiles, which is illustrated in Figure 5.5, left side. The permeability of free films has been determined by the wet-cup method, which is illustrated in Figure 5.5, right side. These illustrations will be explained in the next sections.

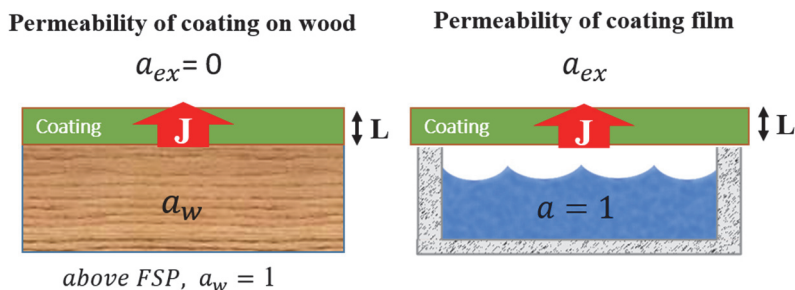


Figure 5.5. Schematic representation of the permeability measurements of coatings on wood by NMR moisture profiles (left) and free films by the wet-cup method (right).

5.3.3.1. Coatings on wood

The NMR moisture profiles were used to determine the water permeability of coatings on wood. The decrease in total MC in time was determined by integrating the drying profiles, and shown in Figure 5.6. Compared to uncoated wood, the applied coating increases the total drying time for all wood-coating combinations. The most significant increase of drying time is observed for pine sapwood, which is about 7 times, whereas about 3 times and more than 4 times for coated teak and coated oak, respectively.

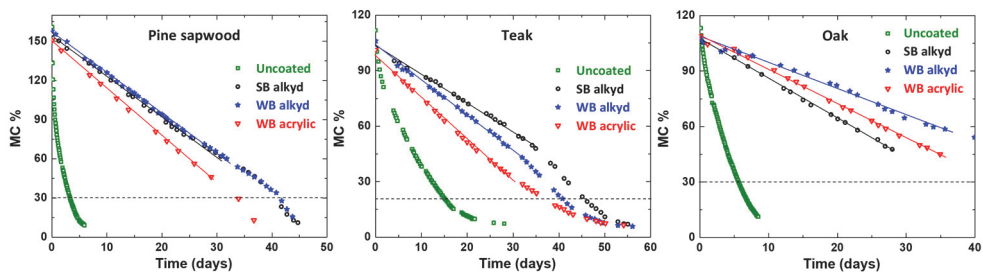


Figure 5.6. The decrease of total MC as a function of time during drying. The data of uncoated wood is obtained from our previous study¹³⁴ in Chapter 4. The solid lines represent the linear fits above FSP.

The MC versus time graphs provides the mass change over time, $\Delta m / \Delta t$. Note that MC is represented as the mass of water over the mass of dry wood; we multiplied the MC by the mass of dry wood to obtain the mass of water only. The flux, the rate of moisture flow per unit area, was calculated via:

$$J = \frac{1}{A \cdot M} \frac{\Delta m}{\Delta t}, \quad (5.2)$$

where $A = 3.1 \text{ cm}^2$ is the area of the coated surface exposed to dry air, and $M = 18 \text{ g/mol}$ is the molar mass of water.

For the points above FSP, a linear relationship confirms Fickian diffusion with a constant diffusion coefficient, D . This allows us to calculate the permeability via:

$$J = D\rho \frac{\Delta a}{L}, \quad (5.3)$$

where ρ is the solubility, $D\rho$ is the permeability of the film, Δa is the water activity difference, and L is the thickness of the film.

Above FSP, the water activity inside the coated wood sample is 1, whereas the external water activity is about 0. This results in constant $\Delta a = 1$, see the left image in Figure 5.5.

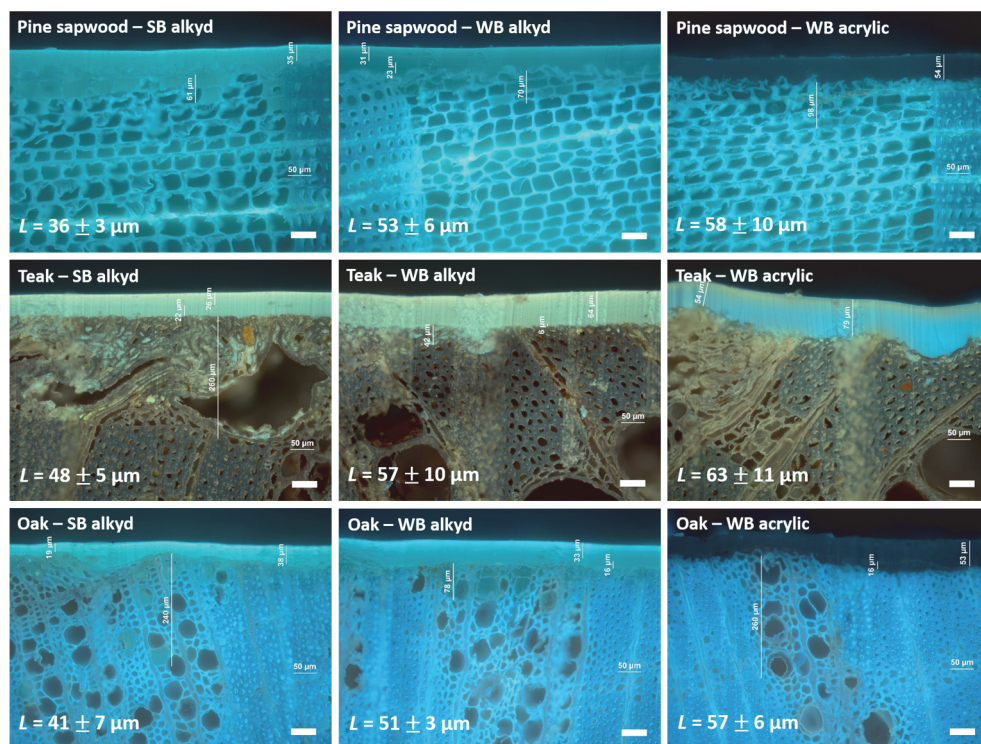


Figure 5.7. The light microscope images of the cross-sections of coated wood using UV-light. The scale bar in the corners represent 50 μm . The thickness analysis is based on 10 different points. The average values (AV) and the standard deviation (SD), $L = AV \pm SD$, are given in the corners of each cross section image.

The thickness of coating films on wood was determined from the cross sections of the samples by using a light microscope, shown in Figure 5.7. Thickness analyses were done on the same samples which were used for the NMR experiments.

The calculated permeability results for coatings on wood will be given in section “Coatings on wood versus free films”.

5.3.3.2. Permeability of free films by wet-cup method

We studied free films in two pre-conditioned states: with and without water treatment. The water treatment was achieved by immersing the films in distilled water for three days, and subsequently drying at room temperature. We call the free films with water treatment as leached and without water treatment as non-leached.

The water permeability of transparent wood coatings was determined by wet-cup measurements on the free films with and without prior water treatment. Glass cups with an area $A = 1.3 \text{ cm}^2$ were filled with water to the half of the cup and sealed with free films having a thickness of L . The cups were put into the desiccators with various humidity conditions, i.e. water activities a_{ex} ranging from 0.33 to 0.97. Saturated aqueous solutions of various salts were used to create the proper relative humidity in each desiccator. Note that the water activity inside the cups was 1. The mass change Δm was measured after keeping the cups in the desiccators with a duration of Δt , which was around two days. The flux, the rate of moisture flow per unit area, was calculated via Equation 5.2. As discussed before, in the case of Fickian permeation through the coating film with a constant diffusion coefficient, the flux is represented by Equation 5.3. Figure 5.8 shows the measured fluxes multiplied by the film thickness through the leached and non-leached films as a function of the water activity difference in the wet-cup measurements. Two samples were studied for each coating type for both leached and non-leached conditions that their results are shown in Figure 5.8. Fickian diffusion with a constant diffusion coefficient has been proven by the observed linear relationship for all the coating types. The slopes of the lines give directly the permeabilities of the coating films via Equation 5.3.

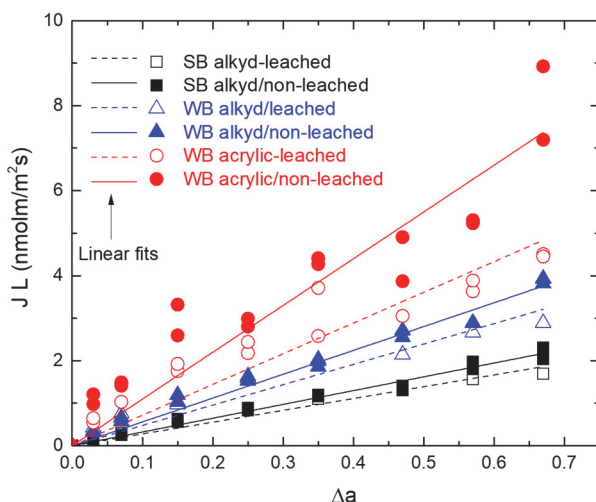


Figure 5.8. Flux (J) multiplied by thickness (L) of each film as a function of water activity difference (Δa) over the non-leached and leached free films. The solid and dashed lines represent the linear fits (R^2 is between 0.97 and 0.99 for SB and WB alkyd, about 0.95 for WB acrylic).

The calculated permeability results for leached and non-leached free films will be given in the next section “Coatings on wood versus free films”.

5.3.3.3. Coatings on wood versus free films

The calculated permeability results for coatings on wood, and leached and non-leached free films are shown in Figure 5.9. The error bars are based on the variation in layer thickness (see Figure 5.7), which is the most influencing factor based on the experiments.

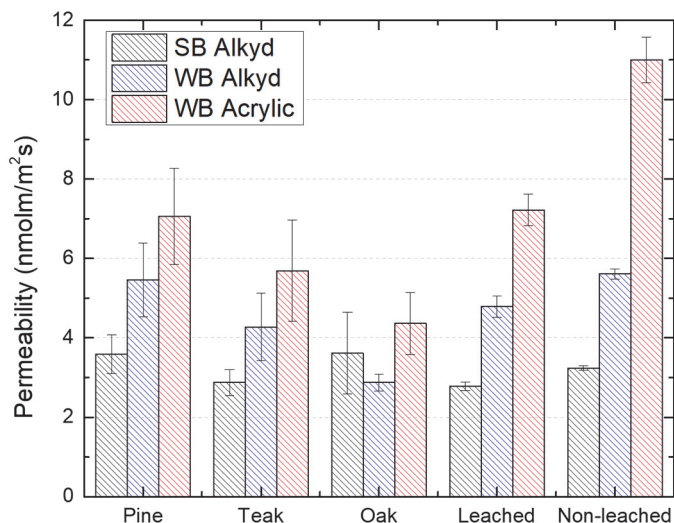


Figure 5.9. Permeability of coatings on wood determined by NMR profiles, and permeability of leached and non-leached free films determined by the wet-cup method.

We first compare the permeability of coatings on different wood species. For softwood pine sapwood and hardwood teak, the permeability values are similar within the error bars. Opposed to teak, pine sapwood has low density and highly permeable pores. These similar results for these very different wood types suggest that there is no significant influence of wood types on the permeability of a coating on wood for the studied coating and wood types. Ahola et al. ³⁹ also observed relatively small differences in permeability of model coatings on pine and spruce, even though these two wood species had large differences in water sorption characteristics. This fact suggests that the wood substrate should not be considered as a primary influence on the water transmission rate through a relatively impermeable coating film, since the rate controlling parameter is the permeability of the coating ¹⁴⁷. For oak, SB alkyd has unexpectedly higher permeability due to vessels, i.e. big pores, on the surface. The orientation of the vessels matters as previously discussed. The film uniformity is expected to be distorted within these regions of large pores, thereby resulting in water permeable paths that may increase the permeability.

After showing that the influence of wood species on the wood coating permeability was not significant, we compare the free films with wood supported films to investigate the influence of wood-coating interactions on the permeability of coatings. The films on wood and the free films after leaching reveal similar permeability values within the error bars. This type of comparison was also performed by Hulden and Hansen ¹⁴⁸, for which they reported water vapor permeability coefficients for some commercial coatings, obtained from measurements on free films and on films on wood substrates. They also observed similar permeability coefficients for the free films and the film on wood. Our findings suggest that effects like penetration or interaction of the coating with the wood has no significant influence on the water permeability for the wood-coating combinations considered. However, the permeability results of coated oak show the significance of careful selection of wooden substrates for the purpose of obtaining as uniform a sample collection as possible.

The permeability results for the free films are in agreement with the values reported by Shreepathi et al. ¹⁴⁹. They worked on pigmented coatings with 13.2 wt. % PVC, and determined the permeability values of the free films by the wet-cup method. They reported the values as $2.1 \times 10^{-9} \text{ mol m}^{-2}\text{s}^{-1}$ for the alkyd system and $1.9 \times 10^{-9} \text{ mol m}^{-2}\text{s}^{-1}$ for the acrylic system, which are in the same order of magnitude with the results reported in this study.

In the light of these observations, the wet-cup method seems to be a good indication for testing the permeability of these coatings in order to get an idea for coatings on wood.

5.3.3.4. Factors affecting permeability

How does the permeability differ for different coating systems? In Figure 5.9, three types of comparisons can be made. Firstly, different non-leached coating systems are compared; WB acrylic has the highest, WB alkyd has the second highest and SB alkyd has the lowest permeability. Secondly, different leached coating systems can be compared, where the same trend with non-leached films is observed. Thirdly, the influence of leaching out any possible water soluble materials on the permeability can be analyzed. It is clear that leaching has a significant effect on the permeability of WB acrylic, which decreases significantly for the films undergoing a prior leaching process. WB and SB alkyds do not display significant differences in the permeability between leached and non-leached films.

The differences in the permeability (P) can be explained by either differences in diffusion (D) or in solubility (S) of water in the coating.

Sorption isotherms and solubility by DVS

The moisture sorption of non-leached and leached films was analyzed using Dynamic Vapor Sorption (DVS) to quantify the amount of water in the films at different humidity conditions. The moisture contents (MC) as a function of relative humidity (RH) for adsorption and

desorption are given in Figure 5.10. The presented results are based on one sample measurement for each type. The shapes of the isotherms are typical for Type III isotherms according to the B.E.T. classification¹⁵⁰, reflecting a process of water clusters in the coating films¹⁵¹.

Three types of comparisons can be made as in the permeability part. Firstly, different non-leached coating systems can be compared; WB acrylic has the highest, WB alkyd has the second highest and SB alkyd has the lowest MC under conditions of high humidity. Secondly, different leached coating systems can be compared; WB acrylic and WB alkyd have almost the same MC, while SB alkyd has the lowest MC under conditions of high humidity. Thirdly, the influence of leaching out any possible water soluble materials on the MC can be investigated.

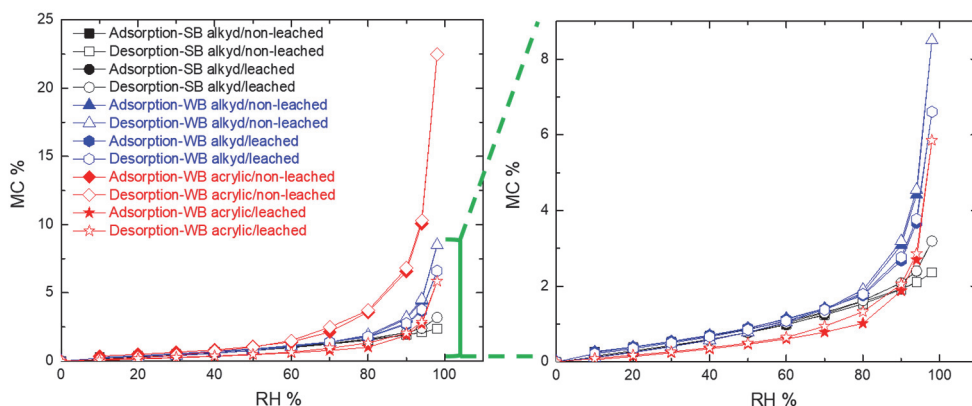


Figure 5.10. Adsorption and desorption isotherms of the non-leached and leached free films, measured by Dynamic Vapor Sorption (DVS).

WB acrylic has the largest difference between leached and non-leached films as the MC decreases significantly with leaching. The MC decreases less for the leached WB alkyd film and does not change significantly for the leached SB alkyd film.

Moreover, there is no hysteresis observed for any of the coatings since the adsorption and desorption isotherms overlap perfectly.

Furthermore, the water solubility of each coating film, i.e. the intrinsic mobility of water molecules, was estimated from the highest humidity condition, which is 98% for DVS. The numerical solubility results are given in Figure 5.11 as a histogram.

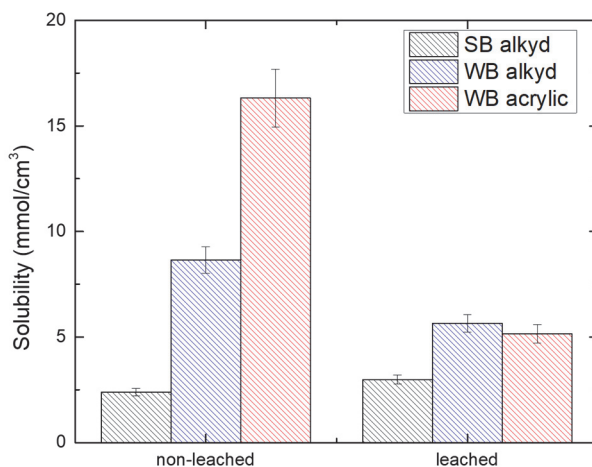


Figure 5.11. Solubility found by DVS at RH of 98%.

Diffusion

The diffusion coefficients were estimated by dividing the permeability by solubility, and are given in Figure 5.12. The diffusion coefficient is in the order of $10^{-12} \text{ m}^2\text{s}^{-1}$, which fits well with diffusion in a solid matrix. These results are also in agreement with the diffusion data for a range of model coatings reported by Muizebelt and Heuvelsland¹⁵².

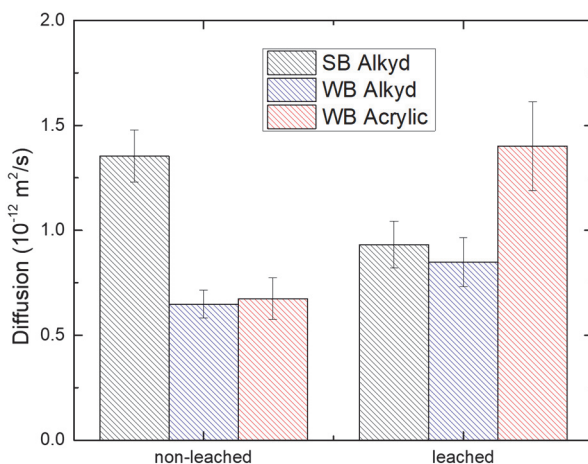


Figure 5.12. Diffusion coefficients of free films.

The non-leached films show a large difference in permeability and solubility. The waterborne coatings have the highest P and S . This may be merely caused by the presence of hydrophilic materials as surfactants, which were used to prepare waterborne emulsions. The WB acrylic contains the highest amount of surfactant and is not crosslinked, thereby

resulting in the highest P and S. The WB alkyd performs better probably due to the lower amount of surfactant combined with the crosslinking capability. As expected, the SB alkyd shows the lowest P and S and the highest D.

After removal of the hydrophilic material in the films by leaching with water, the S remains the lowest for the SB alkyd compared to WB coatings. The WB coatings show equal values for S. The P difference between the systems may be caused by the differences in crosslinking and the residual amounts of hydrophilic material. After leaching, the P and S values decrease significantly for the WB coatings but the leaching has no significant influence on the values for the SB alkyd.

As a conclusion, the permeability is largely determined by the water solubility. In the case of water permeability in polymer films, permeability is more usually dominated by the solubility of water in the polymer, which was illustrated by the work of Muizebelt and Heuvelsland¹⁵². Their data showed that increases in water vapor permeability in a range of model coatings were due to increases in solubility rather than diffusivity, which is in agreement with our findings.

5.4. Conclusions

The drying of coated wood appears to be a homogeneous process in all parts of the wood for all combinations studied - three unpigmented coatings, SB alkyd, WB alkyd and WB acrylic on pine sapwood, teak and oak. In contrast with uncoated wood, no drying front is noticed in coated wood, which shows externally (i.e. coating) limited transport. The barrier properties of the coatings on each wood type seem to be similar regardless of coating type. The free and bound water is in a local thermodynamic equilibrium in the whole range of concentration for any combination.

Prior water treatment of free films allows to study the differences in the permeability, solubility and diffusion of leached and non-leached systems, which probably indicates the influence of the presence of hydrophilic materials as surfactants. The permeability of the coatings is similar for leached free films and films on wood. Apparently, the interaction of the coating with the wood has no influence on the permeability for the considered combinations. Non-leached waterborne films show a significant higher permeability and solubility compared to leached ones. After removal of the hydrophilic material in the films by leaching with water, the permeability and solubility values decrease significantly for the WB coatings but the leaching has no significant influence on the values for the SB alkyd.

Finally, the results show that wet-cup is a good indication for testing permeability of these coatings to get an idea for wood-supported films. But, the films, especially WB systems, should undergo prior leaching process.

Chapter 6

Moisture content of the coating determines the water permeability as measured by 1D magnetic resonance imaging

In addition to the desired aesthetical properties, a coating is applied to protect against weathering. A coating prevents moisture accumulation in wood by reducing the water uptake into the wood by its barrier function. The studies in the coating permeability has gained interest with the shift towards waterborne coatings, which make coatings intrinsically more sensitive to water. This paper presents the results of a Nuclear Magnetic Resonance (NMR) study on the influence of a coating's moisture content on the permeability of a coating on wood. In this work, pine sapwood, oak, and teak were selected as wood types covering a whole range of low to high density wood types. Three transparent coatings were formulated: a solventborne alkyd, a waterborne alkyd and a waterborne acrylic. The aim of this study is to investigate how sensitive the permeability of coatings on wood against moisture during liquid water uptake and subsequent drying below Fiber Saturation Point. During both water uptake and subsequent drying, the coating limited transport was observed for the studied wood-coating combinations. The NMR profiles are used to calculate the water permeability of coatings on wood. We have demonstrated the direct relation of the permeability with the average water activity inside the coating, which is connected to the activities of both sides of the coating. We observed reasonably well correlation between the sorption isotherm of the coatings and the permeability, which proves that the permeability variations are due to the amount of water present in the coating. Finally, we have shown that the permeability is not about the type of water vapour or liquid present at one side of the coating, it is all about the local moisture content in the coating.

This chapter has been submitted to

Ö. Gezici-Koç et al., *Progress in Organic Coatings*.

6. Moisture content of the coating determines the water permeability as measured by 1D magnetic resonance imaging

6.1. Introduction

Wood is a porous material that can accumulate moisture resulting in favourable conditions for decay. For protective and decorative reasons, coatings are generally applied on wooden substrates. The regulations concerning the usage and emissions of volatile organic compounds (VOCs) have led to increased use of waterborne (WB) coatings. While solventborne (SB) coatings are still have their place, WB coatings are becoming more and more common in the wood coatings sector. WB coatings are more sensitive to water compared to SB coatings³⁹, which requires more understanding of the influence of coatings on the changes of wood moisture content.

Several approaches have been used to understand the influence of coatings on water transport through coated wood and resulting wood moisture content. For example, the average moisture content in bulk wood was measured to investigate the water transport properties through coatings^{39–41}. However, the inhomogeneous distribution of water close to the surface have been demonstrated by many studies^{42–45}. These findings reveal the need of measuring the moisture content with spatial and time resolution to evaluate the barrier properties of coatings.

Nuclear Magnetic Resonance (NMR) imaging is one of the methods to study wood moisture content, which is non-destructively providing temporally and spatially resolved moisture profiles⁵⁶. It has proven to be an excellent tool for determining the moisture content of wood samples during water sorption^{44,55,134,153}. The second advantage of NMR imaging compared to other methods (such as weighing^{57,135} or X-ray computer tomography (CT)⁵⁸ or neutron imaging¹³³/radiography⁵⁹) is its ability to distinguish the state of moisture as bound or free water. It allows understanding the transport properties by understanding the changes in bound and free water¹⁰⁸.

Recently, we have published a study, which aimed to elucidate the influence of the wooden substrate on the water vapour permeability of the coating applied to it¹⁵³. NMR imaging was used to measure the moisture content distribution and quantify the changes in bound and free water in wood (pine sapwood, teak and oak) as a function of coating permeability (SB alkyd, WB alkyd and WB acrylic) during drying of completely water saturated samples. We observed that water transport appeared to be externally (i.e. coating) limited for all studied wood-coating combinations. We furthermore compared water vapour permeability of free films and wood supported films to understand the influence of the wood-coating interactions. We found that the interaction of the coating with the wood has no influence on the water vapour permeability for the considered combinations.

The dependence of the permeability to the physical state of water is still in debate^{147,154}. In principle, there is no theoretical difference between the permeation of liquid and water vapour for non-porous materials^{148,155}. However, the coatings have porous structure and the transport of water may occur through capillary flow (especially in pigmented coatings) that may result in the differences between the liquid water and water vapour permeability^{148,155,156}. It is often believed that the permeability of liquid water is higher than the water vapour permeability¹⁴⁷. However, it is still under investigation whether or not the water vapour permeability during drying is really different than the liquid water permeability during water uptake.

The aim of this study is to investigate how sensitive the permeability of coatings on wood against moisture during long term exposure (about 3 months) to liquid water and subsequent drying below FSP. Various combinations of wood and coating types are studied that same wood (pine sapwood, teak and oak) and coating (SB alkyd, WB alkyd and WB acrylic) types with the previous study¹⁵³ are used. More specifically, four subsequent steps are taken to answer to this objective. The first step is to measure the moisture content (MC) distribution in coated wood during liquid water uptake. Besides the MC profiles, relaxation analysis is used to identify and quantify the state of water during water uptake. The second step is to measure the MC distribution during subsequent drying on the same samples. In the third step, the average moisture content in coated wood is found for permeability calculations. Finally, the permeability results are correlated with the average water activity in the coating, and the sorption isotherms of the coatings.

6.2. Materials and methods

6.2.1. Wood and coating types

Three types of wood were studied: one type of softwood, pine sapwood (*Pinus sylvestris*), and two types of hardwood, oak (*Quercus petraea*) and teak (*Tectona grandis*). The properties of these wood types were given in detail in our previous work¹³⁴ in Chapter 4, and the sorption isotherms are recalled in Figure 6.1.

Due to increased use of WB coatings, as a result of the regulations on volatile organic compounds, two types of waterborne (WB) coating and one solventborne (SB) coating as a reference were studied to gain knowledge of how coatings resist water. Three transparent coating formulations, WB acrylic, WB alkyd, and SB alkyd, were prepared by AkzoNobel Decorative Paints, Sassenheim, the Netherlands, specifically for this work, which is a part of a previous work¹⁵³, Chapter 5. The WB acrylic dispersion was based on butyl acrylate and methyl methacrylate, with a glass transition temperature (T_g) of 2.4 °C and a minimum film formation temperature of 7 °C. The final WB acrylic composition had a solid content of 35 wt. (weight) %, and the surfactant amount of 6.9 wt.% on solid content.

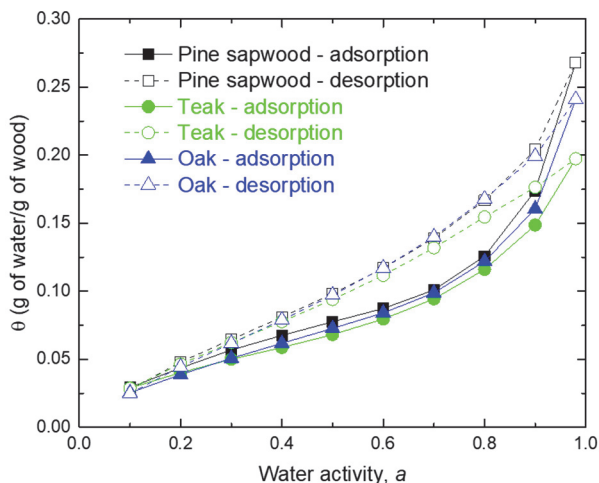


Figure 6.1. Sorption isotherms for pine sapwood, oak and teak measured by Dynamic Vapour Sorption (DVS) at 25 °C. The data is obtained from our previous study¹³⁴, Chapter 4.

The alkyd binder for both WB and SB compositions was based on tall-oil fatty acids with a long oil length and low molecular weight. The WB alkyd emulsion was prepared using a 2% load of non-ionic surfactant to obtain an average particle size of 200 nm. The final WB alkyd composition had a solid content of 35 wt.%, and the surfactant amount of 5.1 wt.% on solid content. The final SB alkyd formulation had a solid content of 65 wt.%.

6.2.2. Coatings on wood

The coatings (WB Acrylic, WB alkyd, SB alkyd) were applied by brush on wood (pine sapwood, oak, and teak). The overview of studied wood-coating combinations is given in Table 6.1.

In all combinations, three layers were applied to get a final effective thickness of around 50 μm on wood. The first layer was sanded to eliminate surface roughness. Two more subsequent layers were applied. The time between the applications of consecutive layers was one day. The coated wood samples were dried at room condition, i.e. 21 °C and 40% relative humidity, for at least four months before the measurements were performed. Note that all measurements were done on unaged coatings.

The dry film thickness of coatings on wood was determined from the cross-sections of the samples by using light microscope (Leica DMRX) according to ISO 2808:2007¹⁴¹ and ISO 1463:2003¹⁴², shown in Figure 6.2.

Table 6.1. Overview of studied wood-coating combinations.

Wood type	Coating type	Coating properties	Applied on
Pine sapwood (<i>Pinus sylvestris</i>)	SB alkyd	Solid Content: 65 wt.%	Radial plane: the rays are parallel and the growth rings are perpendicular to the coated surface
	WB alkyd	Solid Content: 35 wt.% Surfactant: 5.1 wt.% on solids	
	WB Acrylic	Solid Content: 35 wt.% Surfactant: 6.9 wt.% on solids	
Teak (<i>Tectona grandis</i>)	SB alkyd	Solid Content: 65 wt.%	Tangential plane: the growth rings and rays are oriented diagonally (about 45 ° angle) to the coated surface
	WB alkyd	Solid Content: 35 wt.% Surfactant: 5.1 wt.% on solids	
	WB Acrylic	Solid Content: 35 wt.% Surfactant: 6.9 wt.% on solids	
Oak (<i>Quercus petraea</i>)	SB alkyd	Solid Content: 65 wt.%	Tangential plane: the rays are perpendicular and the growth rings are parallel to the coated surface, i.e. vessels are oriented parallel to the surface
	WB alkyd	Solid Content: 35 wt.% Surfactant: 5.1 wt.% on solids	
	WB Acrylic	Solid Content: 35 wt.% Surfactant: 6.9 wt.% on solids	

Firstly, 20 mm diameter cylindrical samples were drilled from 10 mm thick coated wood panels. The samples were fixed on a small piece of wood with epoxy glue for better handling. The cross-sections were made with a sledge microtome by cross cutting them with a sharp microtome knife. The cross-sections were examined with a light microscope using UV-light, where the investigated length was approximately 12 mm. The thickness analysis was based on measuring 10 different points for each sample. Thickness analyses were done on the same samples which were used for the NMR experiments.

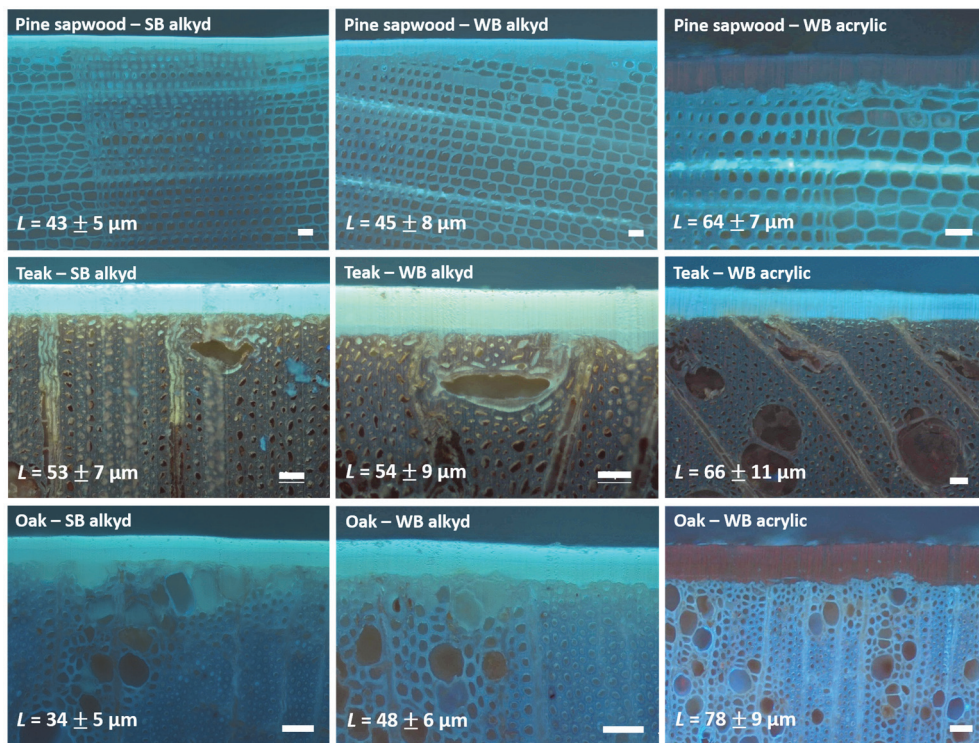


Figure 6.2. The light microscope images of the cross-sections of coated wood using UV-light. The scale bar in the corners represent $50 \mu\text{m}$. The thickness analysis is based on 10 different points. The average values (AV) and the standard deviation (SD), $L = AV \pm SD$, are given in the corners of each cross section images.

6.2.3. NMR imaging and relaxometry

6.2.3.1. Principles and settings

As in the previous work¹⁵³ in chapter 5, NMR imaging and relaxometry was used to measure the moisture content distribution and to quantify the changes in bound and free water in coated wood. For details of the NMR principles we refer to our previous studies^{134,153} in chapters 4 and 5.

The experiments were performed with a home-built NMR set-up with a main magnetic field of 0.75 T and a constant gradient of 418 mT/m. It was designed with an electromagnet from GMW (Model 3473-70) and RadioProcessor™ (USB board) from SpinCore as a digital system for RF signal acquisition, detection and processing¹⁵³.

The moisture profiles were obtained with a Hahn Spin Echo (HSE) sequence and a Carr-Purcell-Meiboom-Gill (CPMG) sequence was used to measure the relaxation time, T_2 .

The resulting NMR signal shows an exponential decay, as described by:

$$I(\tau) = \sum_{i=1}^m I_i \exp\left(-n \cdot 2\tau / T_2^i\right), \quad (4)$$

where $I(\tau)$ is the observed NMR signal at a time, I_i is the signal from each exponential component, and m is the number of components. The signal intensity of each exponential term is proportional to the pore volume^{123,143}. Therefore, the signal intensity of each term versus T_2 values produces a continuous spectrum of T_2 values, i.e. a map of the volume occupied by each pore size or the pore size distribution. For details of the method of T_2 relaxation analysis we refer to our previous papers^{134,153}.

The settings are summarized in Table 6.2. t_e is the echo time, t_{ww} is the recording window, t_{90° is the pulse time, G_z is the linear magnetic field gradient, Δx is the theoretical spatial resolution, n is the number of echoes, n_{avg} is the number of signal averages, and t_{RT} is the repetition time between two subsequent pulses.

Table 6.2. The measurement settings of Hahn Spin Echo (HSE) and Carr-Purcell-Meiboom-Gill (CPMG) pulse sequences used for water uptake and subsequent drying of coated wood for all studied wood-coating combinations.

	t_e (μ s)	t_{ww} (μ s)	t_{90° (μ s)	G_z (mT/m)	Δx (mm)	n	n_{avg}	t_{RT} (s)
HSE	200	120	25	418	0.46	-	4	8
CPMG	200	120	25	418	0.46	2048	32	8

In order to determine the local hydrogen density, the measured signal profiles were divided by the signal profile of a reference sample (an equal volume of aqueous 0.01 M CuSO_4 solution).

The moisture content (MC) was determined from the measured NMR signal based on calibration done in our previous study¹³⁴ and expressed as a percentage of the mass of water over the mass of dry wood (θ). The mass of dry wood is 1.7 ± 0.04 g for pine sapwood, 2.0 ± 0.04 g for oak and 2.0 ± 0.02 g for teak¹³⁴.

6.2.3.2. Samples and sample holder for water uptake/drying of coated wood

20 mm diameter cylindrical samples were drilled from 10 mm thick wood panels (radial cut for pine sapwood, and tangential cut for oak and teak). Prior to the water uptake measurements, all samples were equilibrated at 33% RH for at least 4 weeks. The cylindrical wood samples were mounted in Teflon sample holders. These holders do not show any ^1H NMR signal. A glass tube was glued on top of the samples to act as a water reservoir. The glued glass tube reduces the effective surface radius of the samples to 6.5 ± 0.5 mm from 10 mm. Note that the lateral distribution is so fast that this has no influence on the water

distribution. The sides of the samples were sealed with Teflon grease and Teflon tape to ensure that water can only enter the wood from the top side. Distilled water was put on top of coated wood samples.

The same samples used for the water uptake were used for subsequent drying. After completing the long term (about 100 days) water uptake, the remaining liquid water was taken away from the top of the samples and the top surface was exposed to a flow of dry air. The air flow was set at 3 L/min with an RH about 0-5% at room temperature (~ 22 °C).

6.3. Results and discussion

6.3.1. Water uptake

6.3.1.1. Uncoated wood versus coated wood

In order to understand the barrier properties of coatings during long term exposure to liquid water uptake, we first compare uncoated and coated wood. As an example of comparison, uncoated and WB acrylic coated pine sapwood were chosen that the moisture content (MC) profiles during water uptake are given in Figure 6.3. In our previous paper we discussed the water transport properties in uncoated wood during water uptake¹³⁴, which we will use as a reference in this study. The surface exposed to liquid water is located at position $x=0$. The Fiber Saturation Point (FSP) is indicated by the horizontal dashed line, which was found to be around a MC of 29% for pine sapwood¹³⁴.

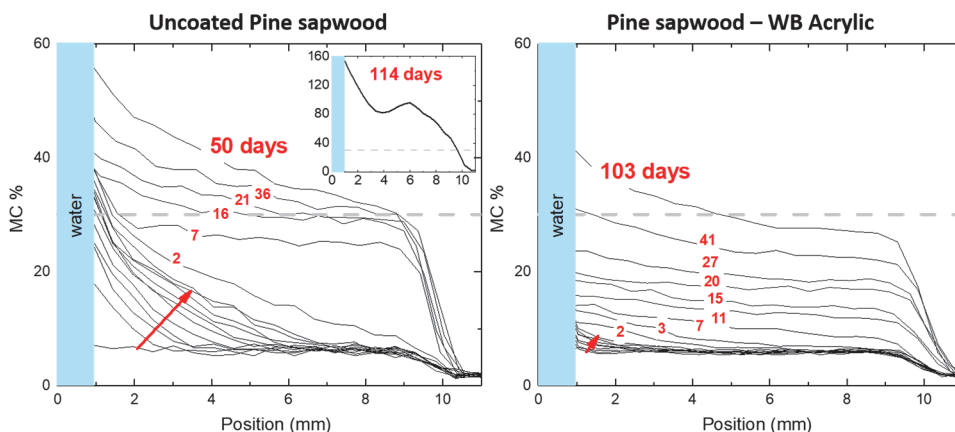


Figure 6.3. The moisture content (MC) profiles of water uptake of uncoated and WB acrylic coated pine sapwood. The data for uncoated pine sapwood is obtained from our previous study¹³⁴ (Chapter 4). Profiles were obtained every 2 h during the first day represented by an arrow, then at indicated times in terms of days.

For uncoated wood, three phases of water uptake are observed. Firstly, during the early phase of the uptake (first 2 days), a front develops indicating that the transport is internally limited. This front occurs until the moisture reaches the bottom, where the MC remains below the FSP. Secondly, there is a homogeneous increase up to the FSP (between 7 and 16

days). Thirdly, the last phase of water uptake occurs above the FSP (between 21 and 114 days), where the MC significantly exceeds the FSP. In the case of WB acrylic coated pine sapwood, we observe the first phase of the uptake during the first week, where the front is not as visible as in the case of uncoated wood. The second phase of homogeneously increasing profiles up to the FSP is observed until around 40 days. Even after about 100 days exposure to liquid water, the MC of the upper part of the sample is slightly higher than the FSP, and the MC of the bottom part is close to but lower than the FSP. In other words, the third phase of the uptake above the FSP is hardly visible for coated wood.

6.3.1.2. Combinations of wood and coatings types

The barrier properties of wood coatings against moisture are investigated by studying various combinations of wood and coating types during long term exposure to liquid water, of which the moisture content profiles are given in Figure 6.4.

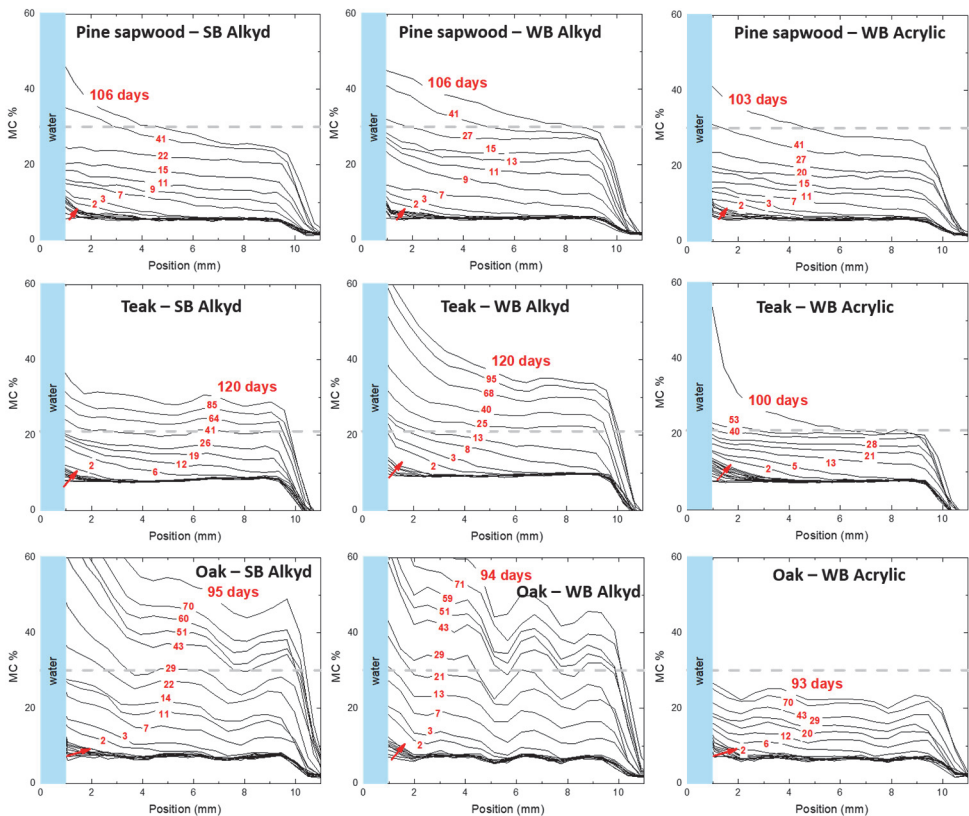


Figure 6.4. The moisture content (MC) profiles of various combinations of wood (pine sapwood, teak and oak) and coating (SB alkyd, WB alkyd and WB acrylic) types during water uptake. Profiles were obtained every 2 h during the first day represented by an arrow, then at indicated times in terms of days.

Note that FSP was found to be around a MC of 30% for oak and 22% for teak¹³⁴.

Pine sapwood

For SB alkyd and WB alkyd coated pine sapwood, the first two phases of the uptake are similar as in the case of WB acrylic coated pine sapwood. The first phase of the uptake is observed during the first week, where the front is not much obvious. Then until around 40 days, the second phase of homogeneously increasing profiles up to the FSP is observed. Until around 100 days, the third phase of the uptake exceeding the FSP is observed for WB alkyd coated pine sapwood, while it is hardly visible for the others.

Teak

For teak with 3 different coating types (SB alkyd, WB alkyd and WB acrylic), the first phase of the uptake is observed during the first week, where the front is not much obvious. The second phase of homogeneously increasing profiles up to the FSP is observed until 40 days for SB alkyd and WB acrylic coated teak, and until 20 days for WB alkyd coated teak. The third phase of the uptake exceeding the FSP is clearly observed for SB alkyd and WB alkyd coated teak until 120 days, while it is hardly visible for WB acrylic coated teak even after about 100 days.

Oak

In the case of oak, the wave-like moisture distribution is observed for SB alkyd, WB alkyd and WB acrylic coated oak. This is because of the structure of the wood, i.e. the orientation of the vessels to the surface¹⁴⁶. The vessels in the earlywood rings have different water capacity compared to the cells in the latewood rings. When these vessels are oriented parallel to the surface as in this case, a lower MC is observed in these regions, which leads wave-like moisture distribution through wood samples. For oak with 3 different coating types (SB alkyd, WB alkyd and WB acrylic) we again observe the first phase of front like uptake for the first week. For SB alkyd and WB alkyd coated oak, the second phase of homogeneously increasing profiles up to the FSP is observed until 22 days. The third phase is observed until 95 days, where the MC exceeds the FSP over the whole sample. For WB acrylic coated oak, the third phase is not observed at all. Even after 93 days the MC is far below the FSP – around 20% – all over the sample, even close to the surface.

Besides the MC profiles, relaxation analysis is used to identify and quantify the state of water during water uptake, shown in Figure 6.5. The relaxation analysis is performed at three different points, around 2 mm (top), 5 mm (middle) and 8 mm (bottom) below the coated surface, where it relates to a region of 0.5 mm width at each position.

At all positions, free water is only observed after all the cell walls are saturated with the bound water. This is the transition point from the second phase of the uptake to the third phase. The number of days indicated by vertical arrows represent the beginning time of the third phase. During the first and the second phases of the uptake below FSP, only bound

water is available showing the transport in the vapour phase and in the wood fibers¹³⁴. Free water is available only in the third phase.

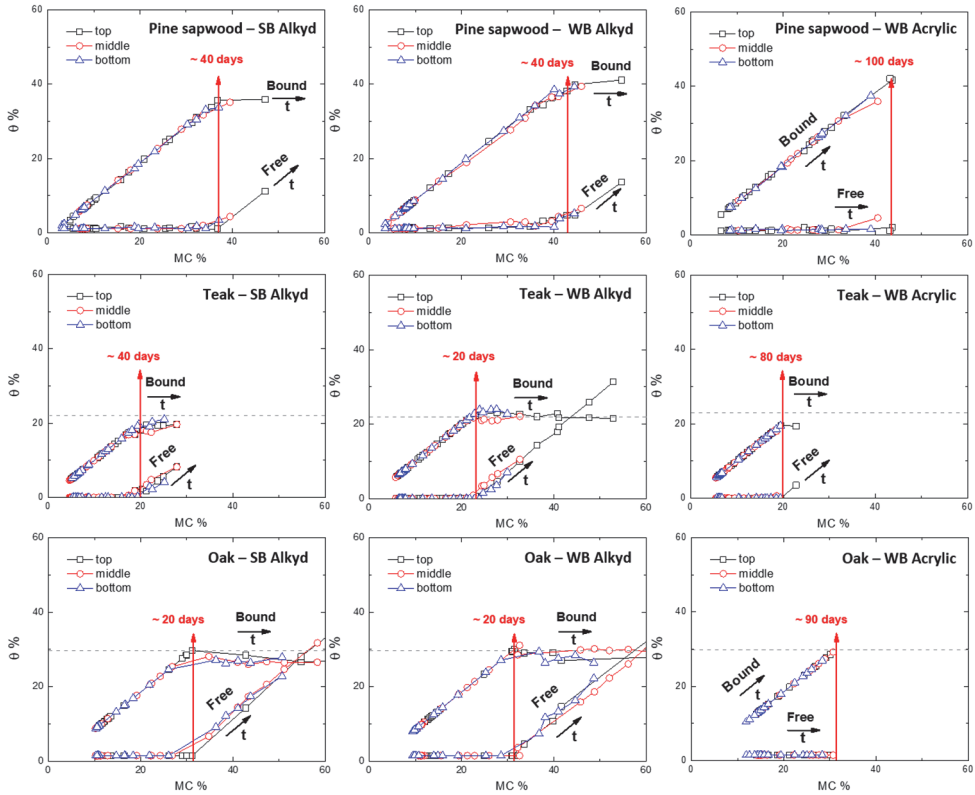


Figure 6.5. Moisture fractions (θ) of free and bound water versus total MC at 3 positions; around 2 mm (top), 5 mm (middle) and 8 mm (bottom) below the coated surface.

6.3.2. Drying after water uptake

After the liquid water uptake, drying is performed on the same samples to follow the moisture profiles during water vapour leaving the wood through the coatings. After completing the long term water uptake, the remaining liquid water was taken away from the top of the samples and then the top surface oak was exposed to a flow of dry air. The MC profiles during drying are given in Figure 6.6 for coated pine sapwood, teak and oak. The surface exposed to dry air is located at position $x=0$. The FSP is indicated by horizontal dashed line.

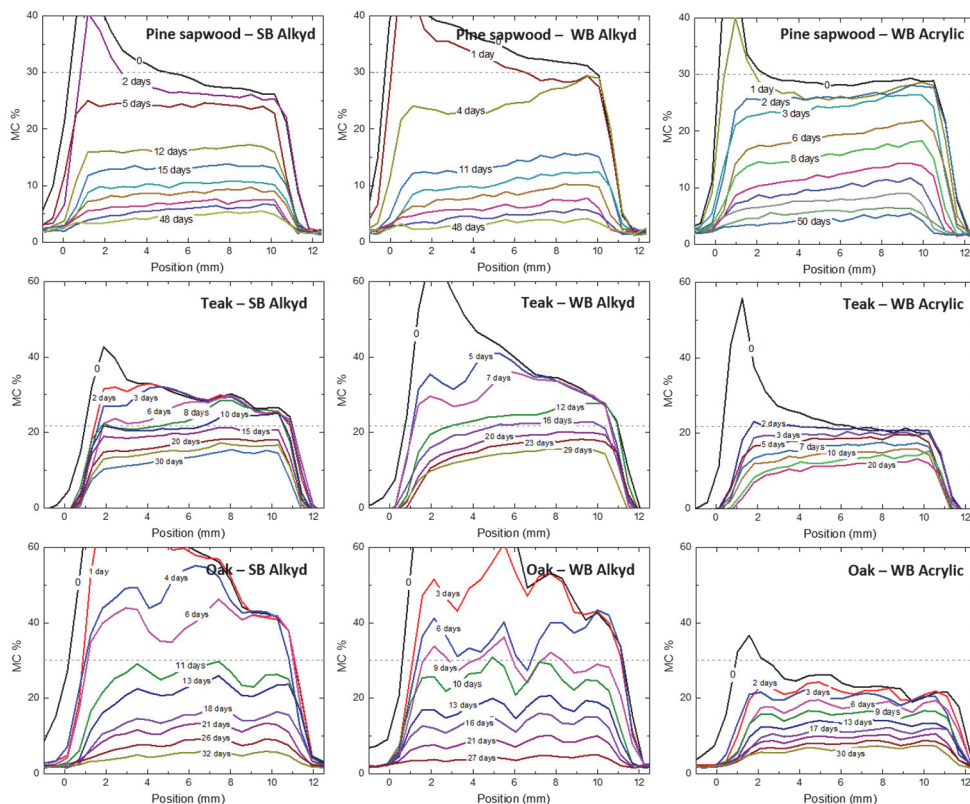


Figure 6.6. The moisture content (MC) profiles of various combinations of wood (pine sapwood, teak and oak) and coating (SB alkyd, WB alkyd and WB acrylic) types during drying just after water uptake. Profiles were obtained at indicated times.

In all wood-coating combinations, homogeneously decreasing profiles are observed which shows the coating (externally) limited drying. Note the peak on the coated surface during the early phase of drying. This peak comes from the moisturized glue which was used to glue a glass tube on top of the samples to act as a water reservoir. When the glue is wet, it also gives NMR signal resulting the observed peak. However, it dries in time and its relaxation becomes very short that cannot give signal anymore.

The change in average MC over the whole sample during water uptake and subsequent drying is also shown in Figure 6.7. The average MC has been calculated by summing up the MC values and dividing by the number of points on the MC profiles. The error bar represents the standard deviation in MC over a MC profile. Note that the average MC was calculated after the peak from moisturized glue disappears, such as 5 days after in the case of SB alkyd coated pine sapwood (see Figure 6.6).

Moisture content of the coating determines the water permeability as measured by 1D magnetic resonance imaging

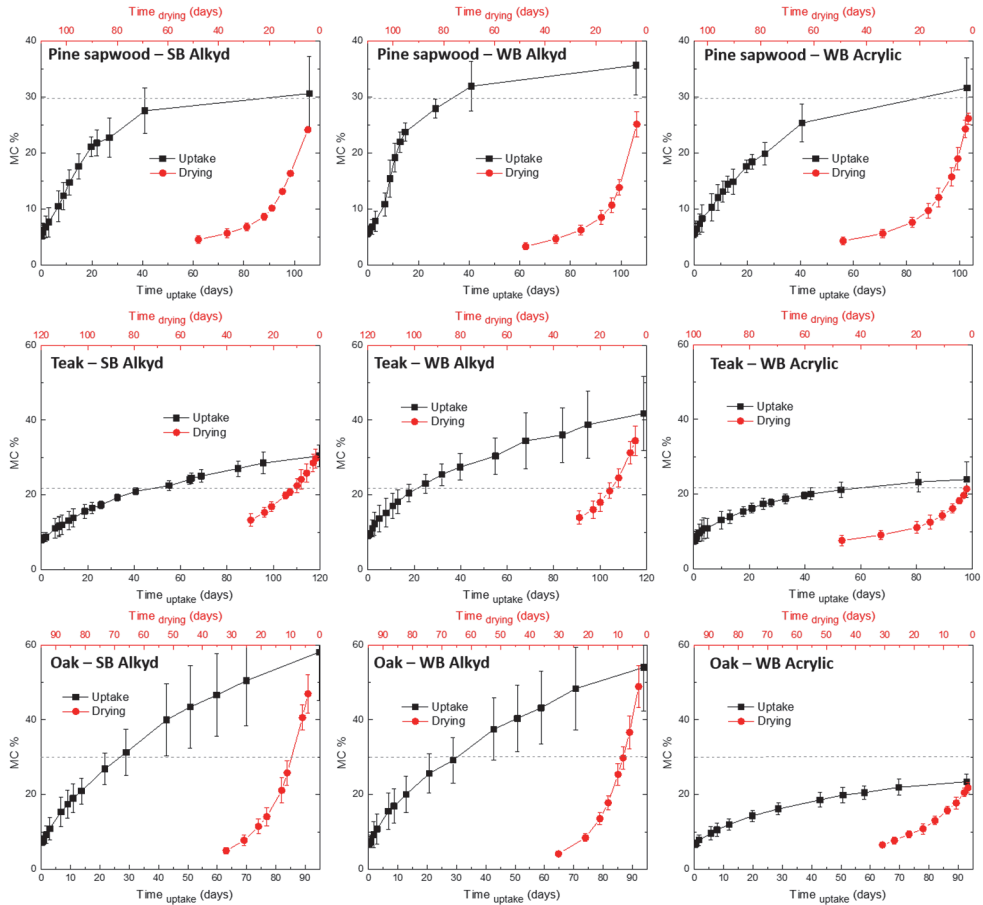


Figure 6.7. The change in average MC over the whole sample during water uptake and subsequent drying.

Note that the average MC below the FSP during drying will be used to calculate water permeability below the FSP.

6.3.3. Permeability of coatings

6.3.3.1. Theory

The water permeability of transparent coatings on wood can be calculated from the NMR profiles. In order to calculate permeability of coatings on wood during liquid water uptake and subsequent drying below the FSP, we performed following derivations.

The total amount of water in the wood can be connected with the flux through coating via the mass conservation equation:

$$\frac{1}{A \cdot M} \frac{\Delta m}{\Delta t} = -J \equiv -k \frac{\Delta a}{L}, \quad (6.5)$$

where A [m^2] is the area of the coated surface exposed to liquid water or dry air and $M = 18$ g/mol is the molar mass of water. $\Delta m / \Delta t$ is the mass change over time. m is the total amount of water in the wood, which is obtained by multiplying the average moisture content θ (m/m_{wood} [g/g]) by the dry mass of the wood sample, m_{wood} .

The right side of the equation represents the flux through coating, J [$\text{g}/\text{m}^2\text{s}$]. $k \equiv D\rho$ is the permeability of the film, where D [m^2/s] is the diffusivity of water through the coating, ρ [g/m^3] is the solubility. L [m] is the thickness of the film. The driving force for the flux is the water activity difference $\Delta a \equiv a - a_{\text{ex}}$, where a and a_{ex} are the water activities in the wood and the environment, respectively.

Local flux

At a given point in the coating with a thickness L the mass flux J equals:

$$J = -D(a) \left(\frac{\partial \rho}{\partial a} \right) \frac{\partial a}{\partial x} \equiv -f(a) \frac{\partial a}{\partial x} \quad (6.6)$$

where f is a combination of the local diffusion coefficient and the solubility. And in case that the diffusion coefficient varies with the water content, f can be a function of a (the local water activity). Also, $\partial \rho / \partial a$ is the derivative of the sorption isotherm, where sorption comes into play.

We assume that the density distribution of water in the coating slowly varies compared to the flux, so the flux will be constant at very point in the coating. Therefore:

$$JL = - \int_0^L f(a) \frac{\partial a}{\partial x} dx = -[F(a_L) - F(a_0)] \quad (6.7)$$

where F is the primitive of f . Moreover, one can consider a_0 as the water activity in the wood and a_L as the water activity of the environment. As a consequence, one can define a permeability k as,

$$k \equiv \frac{|J|L}{|\Delta a|} = \frac{F(a_L) - F(a_0)}{|a_L - a_0|} \quad (6.8)$$

Activity dependent permeability

To understand the relation between the permeability and the activities at both sides of the coating, we start with the following expression for f ,

$$f(a) = f_0 + f_1 a + O(2). \quad (6.9)$$

The primitive of this expression (Eq. 6.6) is

$$F(a) = const + f_0 a + \frac{1}{2} f_1 a^2 + O(3) \quad (6.10)$$

Inserting this expression (Eq. 6.7) into the derived equation for the permeability (Eq. 6.5) gives

$$k = \frac{F(a_L) - F(a_0)}{|a_L - a_0|} = f_0 + \frac{1}{2} f_1 (a_0 + a_L) + O(2) \quad (6.11)$$

This expression (Eq. 6.8) demonstrates the importance of the state on both sides of the coating. The second term shows how the moisture distribution in the coating could affect the permeability. It also supplies a simple parameter for this: $\frac{1}{2}(a_0 + a_L)$, which is the average water activity in the coating.

6.3.3.2. Permeability of one coated system

The NMR moisture profiles were used to determine the water permeability of coatings on wood by Eq. 6.2. WB acrylic coated pine sapwood was chosen to show how to calculate water activity dependent permeability, and its correlation with the average water activity in the coating.

Eq. 6.2 can be rewritten as,

$$k \equiv \frac{L}{A \cdot M} \frac{\Delta m}{\Delta t} \frac{1}{|\Delta a|} \quad (6.12)$$

The MC versus time graphs (Figure 6.7) provides the mass change over time, $\Delta m / \Delta t$.

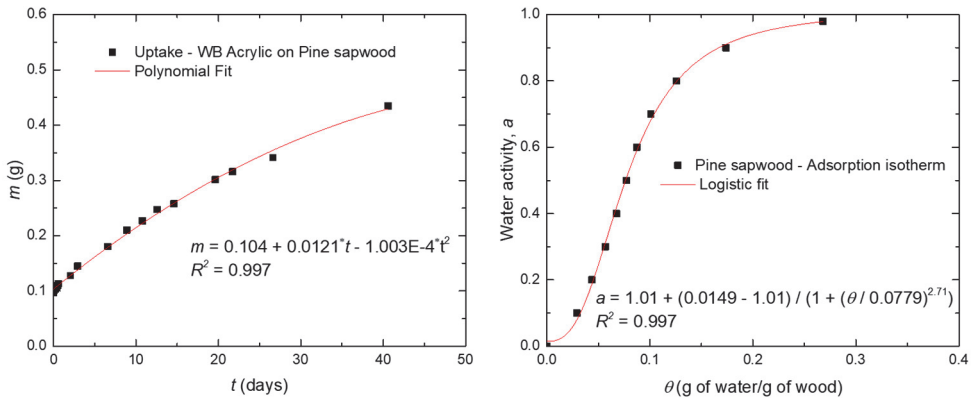


Figure 6.8. (a) The total amount of water in the wood (m) versus time (t). (b) Water activity (a) versus the average moisture content (θ).

Firstly, the average moisture content (θ) is obtained by dividing the MC by 100. θ is the mass of water over the mass of dry wood; so θ is multiplied by the mass of dry wood to obtain the total amount of water in the wood. Secondly, an equation is obtained for the

mass change over time, which is the derivation of the fitted equation of m versus t plot (Figure 6.8a). Thirdly, the average moisture content (θ) is not constant, but depends on the water activity, $\theta(a)$. The sorption isotherms of uncoated wood in Figure 6.1 are used to obtain the reverse isotherm (Figure 6.8b). a is the water activity in the wood, which is obtained at each θ value by a versus θ in Figure 6.8b. Then the water activity difference, $\Delta a \equiv a - a_{ex}$, is calculated where a_{ex} is the water activity in the environment that is 1 for uptake and 0 for drying. Finally, L , A and M are known values, which are directly put in Eq. 6.9 to find permeability, see Figure 6.9.

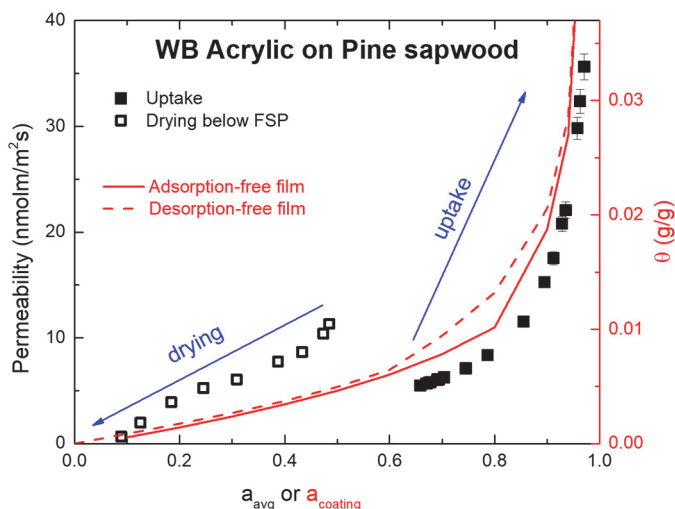


Figure 6.9. Permeability of WB acrylic on pine sapwood for liquid water uptake and subsequent drying below the FSP. Adsorption and desorption isotherms of leached free films, measured by DVS were obtained from the previous study¹⁵³ (Chapter 5).

Recalling the previous section that the activities at both sides of the coating, i.e. the average water activity in the coating, could affect the permeability. Figure 6.9 shows the permeability versus the average water activity in the coating for WB acrylic on pine sapwood. The average water activity of the coating is calculated by taking the average of the external water activity (1 for uptake and 0 for drying) and the water activity inside the wood.

There are two parts in the curve; drying and uptake. There is roughly continuous curve from the drying branch to the uptake branch. First part, where the average water activity in the coating is below 0.5, shows the permeability variations during drying below FSP. In this part, the permeability drops as the average water activity in the coating decreases. Second part, where the average water activity in the coating is above 0.5, shows the permeability variations during uptake. In this part, the permeability rises as the average water activity in

the coating increases. At the end of the uptake, it has the highest permeability, where the activity is 1 on both sides of the coating.

It has been observed that permeability varies as a function of average water activity, which hints towards the importance of the amount of water present inside the coating, so the sorption isotherm. In order to check if there is any correlation between the permeability and the sorption isotherm, the adsorption and desorption isotherms of leached free film for WB acrylic are shown in Figure 6.9. The scale of the sorption curves is set such that it covers the scale of permeability to be able to correlate the permeability to sorption isotherms of the coating.

The trend in the permeability variations is in line with the sorption isotherms of the coating, which shows a reasonable correlation. This also proves that the permeability variations are due to the coating absorption itself. Moreover, the permeability is equal to diffusion coefficient (D) times the solubility (ρ), so the sorption isotherm basically. The good correlation of the permeability with the sorption isotherm raises the question about constant diffusion, which is an open discussion that deserves more study.

6.3.3.3. Permeability of all coating-wood combinations

In order to understand if the activity dependent permeability is specific for one particular system (WB acrylic on pine sapwood), or it holds for the other systems as well, the permeability variations for various combinations of wood and coating types are studied during liquid water uptake and subsequent drying, see Figure 6.10.

For each coating type, there is quantitatively similar trend between different wood types. As seen in the previous chapter, the permeability is hardly sensitive to the wood type¹⁵³. The permeability variations for different coating-wood combinations show the similar behaviour as the WB Acrylic on pine sapwood discussed in the previous section. Firstly, all the curves are continuous in such a way that the drying branch and the uptake branch can be easily connected together. Secondly, the permeability rises when the average activity increases during uptake, and drops when the average activity decreases during drying. In other words, the permeability has a direct relation with the average water activity inside the coating, which is connected to the activities of both sides of the coating.

The adsorption and desorption isotherms of leached coating films are shown in Figure 6.10 to check if the correlation between the permeability and the sorption isotherm holds for all studied coating and wood combinations.

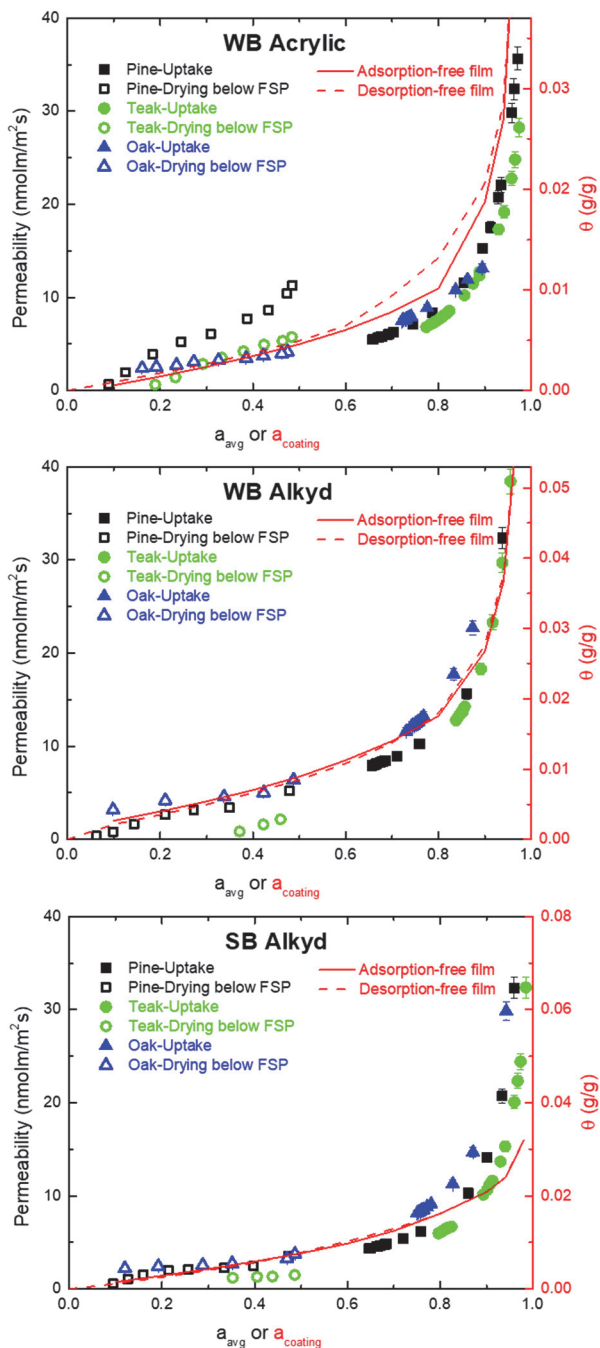


Figure 6.10. Permeability of coatings (WB acrylic, WB alkyd, SB alkyd) on wood (pine, teak, oak) for liquid water uptake and subsequent drying below the FSP. Adsorption and desorption isotherms of leached free films, measured by DVS were obtained from the previous study¹⁵³ (Chapter 5).

The overall trend in the permeability variations is in line with the sorption isotherms of the coatings. For all studied systems, this correlation between the sorption isotherm and the permeability is remarkably well, suggesting that the permeability variations are due to the amount of water present in the coating. However, there is one remark that this correlation with the sorption isotherm may vary in case a polymer plasticizes above certain moisture content. This type of condition may significantly influence the permeability. Further tests to check whether or not the correlation with the sorption isotherm is polymer specific, should focus on polymers which can be easily plasticized. Although it is not very interesting from coating perspective, nylon could be a nice testing polymer to investigate the limitations.

The permeability variation due to the amount of water present in the coating hints towards the importance of the boundary conditions. The biggest variation in the permeability is observed at the switch from drying to uptake, where there is more water during uptake than drying. It suggests that it is not so much due to the fact that is vapour or liquid. In fact, the dependence of the permeability to the physical state of water is still in debate^{147,148,154-156}.

As shown in this study, it is not about the type of water vapour or liquid present at one side of the coating; it is all about the moisture content of the coating which is connected to the water activities of the sides of the coating. In other words, permeability is all about the local moisture content in the coating. At this point, there is an open discussion related to the previous work¹⁵³, in which the permeability of free films was found constant via wet-cup experiments. We still have to investigate how the outcomes of this study link to the previous results found by wet-cup. This will require a more detailed series of experiments.

6.4. Conclusions

The distribution of moisture content in coated wood during liquid water uptake and subsequent drying were studied in detail by NMR imaging. During both water uptake and subsequent drying, coating limited transport was observed for the studied wood-coating combinations – three unpigmented coatings, SB alkyd, WB alkyd and WB acrylic on pine sapwood, teak and oak. During water uptake, free water was only observed after all the cell walls were saturated by the bound water, which showed a local thermodynamic equilibrium of bound and free water.

The water permeability of coatings on wood was calculated from the NMR profiles, then the results were correlated with the average water activity in the coating. The following conclusions are valid for all studied wood-coating combinations. Firstly, there is a continuous curve from the drying branch to the uptake branch. The permeability strongly rises as the water activity increases. In other words, the permeability has a direct relation with the average water activity inside the coating, which is connected to the activities of both sides of the coating. Secondly, the correlation between the sorption isotherms and the

permeability is remarkably good, which proves that the permeability variations are due to the amount of water present in the coating. This good correlation raises the question about constant diffusion, which is an open discussion that deserves more study. In overall, the permeability is not about the type of water vapour or liquid present at one side of the coating; it is all about the moisture content of the coating.

A few issues upon these conclusions that need to be addressed in future research. Further tests are suggested to check whether or not the correlation between the permeability and the sorption isotherm is polymer specific. This requires a study on polymers which can be easily plasticized in which nylon could be a nice testing polymer to investigate the limitations. Secondly, it has to be still investigated how wet-cup experiments fit in the outcomes of this study that requires a more detailed series of experiments, such as more points in the dry region.

Chapter 7

Conclusions and Outlook

7. Conclusions and Outlook

7.1. Conclusions

The work in this thesis contributes to a more in-depth understanding of (i) drying (curing) of alkyd coatings under the influence of cobalt alternatives, and the working mechanism of secondary driers in combination with cobalt alternatives (and even for cobalt), and (ii) the influence of key factors – the wood substrate, the type of binder (coating), the wood-coating interface, and the moisture content of the coating – on the permeability of a wood coating. The main conclusions of this work are summarized in this chapter.

7.1.1. The influence of cobalt alternatives and secondary driers on curing of alkyds

In the first part (Chapter 2), the influence of Co alternatives (Mn- and Fe-based driers) on curing of alkyd coatings was studied by investigating the molecular network development and mechanical properties of the final films. During the drying in the presence of Co-based drier, a skin layer is formed that acts as a front and moves towards the bottom of the film. On the other hand, Co alternatives exhibit more uniform, i.e. homogeneous, crosslinking throughout the film. Further analyses show that Co gives a lower overall drying rate, significantly higher final crosslink density and hardness development compared to its alternatives. These results can be explained by the balance between the speed of crosslinking reactions and oxygen diffusion, which determines the dominating type of drying.

The skin layer is densely crosslinked and limits the oxygen penetration into deeper layers, resulting in slower drying of the bottom part. At the end, a highly crosslinked hard film is achieved by the stepwise crosslinking with the available alkyd chains in the bottom viscous liquid. In case of homogeneous drying, oxygen diffusion is fast relative to crosslinking reactions. This results in hindering the film hardening. However, the long-term drying promotes further crosslinking and hardness development, but still exhibits lower values compared to front-forming drying.

In the second part (Chapter 3), we investigated the role of secondary driers (Ca- and Zr-based) in combination with Co alternatives on drying speed, crosslink density and hardness development. In the beginning of drying, there is an inhibition period present. The addition of secondary driers reduces the inhibition period. Ca seems to be more efficient than Zr in reducing the inhibition period. The exact mechanism, however still needs to be unraveled.

Furthermore, we found that the addition of Ca-based drier increases the front speed, which is most likely due to increasing the permeability of oxygen. In addition, Zr-based drier increases the crosslink density, determined by DMA. In a diagram showing both the crosslink density and front speed, the effect of Ca and Zr can be described as a vector addition, i.e. they have additive effects.

These findings provide an overall update for the paint industry and the ongoing research of Co alternatives. For further optimization of Co alternatives, the focus of the research should be on understanding the influence of the driers on drying pattern of the film and the role of inhibition period on the drying rate. Front drying works best to obtain densely crosslinked hard films. For a fast drying film with a reasonable crosslink density and hardness, a primary drier in combination with secondary driers promoting homogeneous drying without an inhibition period should be preferred.

7.1.2. The permeability of a coating as a function of wood type and the water activity

We studied moisture transport (water uptake and drying) through coatings on wood to understand the influence of key factors – the wood substrate, the coating type, the wood-coating interface, and the moisture content of the coating – on the permeability of a coating. Throughout this work, same wood (pine sapwood, oak and teak) and coating (unpigmented SB alkyd, WB alkyd and WB acrylic) types were used.

The studies on the wood itself (Chapter 4) showed that water transport appeared to be internally (i.e. wood) limited during both uptake and drying. This means that the water movement is limited by water transport within the wood. We further found that there is a unique coupling between the MC and the fractions of bound and free water during uptake and drying. This fact allows to obtain the ratio between each state at any period, just by knowing the MC. For conceptual understanding of transport mechanism, we compared experimentally determined diffusion constants with those derived by the diffusion models. We found that diffusion in the cell wall fibers plays a critical role in the transport process.

To understand the influence of the wood substrate on the permeability, we compared water permeability of free films and wood supported films (Chapter 5). We studied free films in two pre-conditioned states, whereas the free films with water treatment are considered as *leached* and without water treatment as *non-leached*. This allows to study the differences in the permeability, solubility and diffusion. Non-leached WB films show a significant higher permeability and solubility compared to leached ones. After removal of the hydrophilic material (such as surfactants) in the films by leaching with water, the permeability and solubility values decrease significantly for the WB coatings, but the leaching has no significant influence on the values for the SB alkyd. We found that the permeability of the coatings is similar for leached free films and films on wood. Apparently,

the interaction of the coating with the wood has no influence on the permeability for the considered combinations. These results show that wet-cup is a good indication for testing permeability of these coatings, when applied on wood. The films, especially WB systems, should undergo, prior to a wet cup experiment, a leaching process.

We have demonstrated the direct relation of the permeability with the average water activity inside the coating, which is connected to the activities of both sides of the coating (Chapter 6). The permeability rises when the average activity increases during uptake, and drops when the average activity decreases during drying. Further, the correlation between the sorption isotherms and the permeability is found to be remarkably well, which proves that the permeability variations are due to the amount of water present in the coating. This good correlation raises the question about constant diffusion, which is an open discussion that deserves more study. In overall, the permeability is not about the type of water vapour or liquid present at one side of the coating; it is all about the moisture content of the coating.

7.2. Outlook

In the previous section, important conclusions are drawn from the work presented in this thesis. Here, we suggest several issues upon our findings that need to be addressed in future research.

7.2.1. Understanding the relation between oxygen diffusion and crosslinking of alkyds

In this subsection we discuss the value of understanding the key factors that determine oxygen transport in alkyds. Such a study is of interest because the influencing factor of the chemistry of crosslinking reactions in alkyds is the physical processes, especially oxygen diffusion. The key research question is how oxygen diffusion is affected as a function of the crosslink density, the type and the amount of primary and/or secondary driers, and the temperature, etc. Therefore, a technique is needed to visualize how and how much oxygen transports through an alkyd film during crosslinking.

We made several attempts on the design of a gas permeation cell, testing the alkyd films with various concentrations of calcium based secondary drier. For that purpose, we used a portable optical oxygen meter (Fibox 3, PreSens) with a sensor (Planar Oxygen-Sensitive Spot with a diameter of 10 mm, PreSens). Initial trials explored how much oxygen diffuses through a coating film. In our first experimental set-up, we placed the free film in the screw cap with a central hole (diameter of 15 mm), as shown in Figure 7.1a. The oxygen sensor spot was mounted in a transparent vessel, see the bottom part of the vessel in Figure 7.1b, and then read out contactless from the outside – through the container. There was no oxygen measured by the oxygen meter after a day. Secondly, we designed a special glass vessel with an extra narrow neck to connect with a tube, see Figure 7.1c. As shown in Figure

7.1d, the tube was placed to achieve a U-shape and included grease to regulate the pressure. There was still no oxygen measured by the oxygen meter at the end of 20 h.

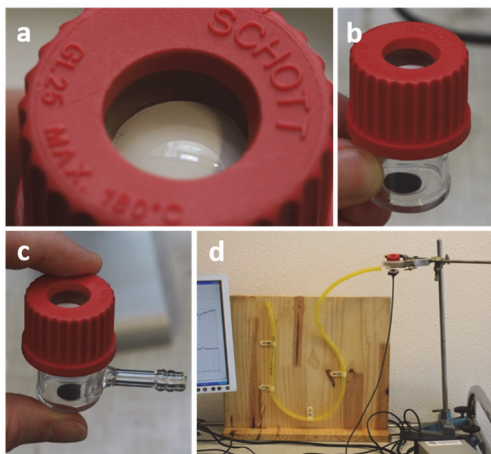


Figure 7.1. Experimental set-up for the measurement of oxygen permeability; (a) free coating film placed in the screw cap with a central hole, (b) oxygen sensor spot mounted at the bottom in a transparent vessel, (c) specially designed vessel with an extra narrow neck, and (d) U-shaped tube with grease connected to the specially designed vessel with the narrow neck.

These initial trials to explore how much oxygen diffuses through a coating film were valuable to further develop the method. Firstly, a smaller volume-sized vessel is recommended to achieve a detectable concentration of oxygen. Secondly, a proper screw cap should be searched in order to get a leak-free system.

Measuring the oxygen permeability during film formation is also recommended for further research to unravel the exact mechanism of the formation of crosslinking front. The oxygen sensor can be mounted on a glass slide, and the coating can be applied on the sensor. Note that the coating should be transparent for not interfering with sensor read-out. By this method, the amount of oxygen that reaches the bottom of the coating can be measured, and related to the speed of crosslinking front. However, it should be taken into account that these oxygen sensors are costly, and each coating application will require an unused sensor.

7.2.2. The factors influencing the permeability of a coating

7.2.2.1. Effect of climatic conditions

The research question is how the climatic conditions affect the permeability of a coating. In this thesis, the water transport properties of coated wood were studied under extreme conditions, such as drying of a completely water saturated samples (Chapter 5) and liquid water uptake for very long period up to 3 months (Chapter 6) in order to determine the boundaries. However, most natural fluctuations in relative humidity are cyclic of nature, e.g. daily or seasonal. It is required to study moisture transport behavior under the cyclic

conditions simulating natural fluctuations in the hygroscopic (i.e. water vapor) range. For further studies, the relative humidity of air blown over the top surface can be varied by using a humidifier¹⁵⁷. It mixes a dry and a wet air stream and their mixing proportions determine the relative humidity of the resulting air stream.

7.2.2.2. Effect of weathering

One of the key research question in the beginning of this work was understanding the barrier properties of a coating in relation to its weathering conditions for improving its performance. Due to time constraints, only unweathered samples were studied. The several weathering conditions multiplied by the studied coating-wood combinations (nine in total) would have resulted in very high number of samples to study. For a follow-up study, only weathered samples can be investigated by selecting less wood-combinations. While planning the project schedule, timing for weathering the coated wood and the time required for an NMR measurement should be carefully noted.

7.2.2.3. Effect of the number of layers/thickness on water transport of coated wood

In this subsection we are going to elucidate the influence of the number of layers/thickness on the water permeability. In this thesis, one type of condition in terms of the number of layers/thickness was studied in Chapters 5 and 6. This section includes preliminary results of multilayered coated wood to explore the influence of the number of layers/thickness on the water transport properties.

We chose two types of coatings to study two set of conditions; WB acrylic is believed to be more water sensitive compared to SB alkyd. Note that the same coating formulations as applied in Chapters 5 and 6 were used. These coatings were applied on two types of wood; pine sapwood and teak. These two types of wood were selected to have variations in the density, where teak is a denser wood compared to pine sapwood. The coatings were applied on wood in various layers to get a final effective thickness of around 25 μm for 1 layer, 50 μm for 2 layers, 75 μm for 3 layers, and 100 μm for 4 layers (see the light microscope images in Figure 7.2 for the measured thickness of selected ones). In all cases, the first layer is sanded till zero thickness and counted as the zero layer.

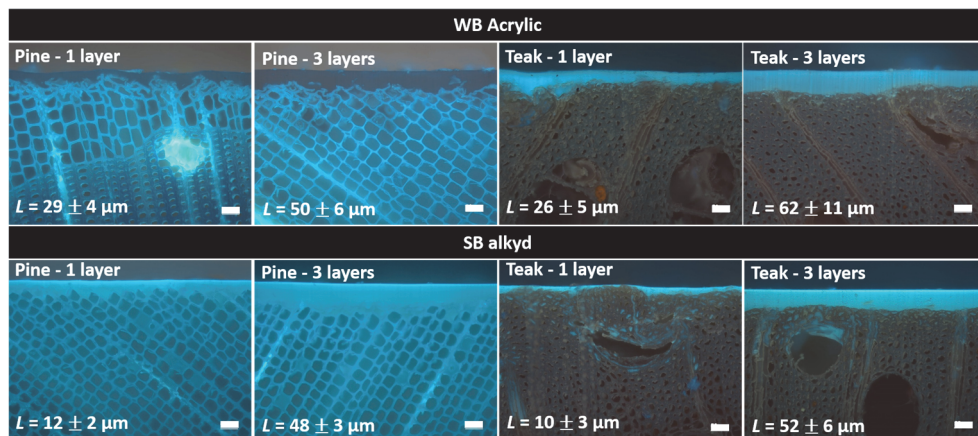


Figure 7.2. The light microscope images of the cross-sections of coated pine sapwood and teak using UV-light. The scale bar in the corners represent $50 \mu\text{m}$. The thickness analysis is based on 10 different points. The average values (AV) and the standard deviation (SD), $L = AV \pm SD$, are given in the corners of each cross section images.

The moisture content distribution in multilayered coated wood during liquid water uptake was studied in detail by NMR imaging. In order to compare the barrier properties of different layers/thickness on pine sapwood and teak, the increase in the MC for the 1 mm region below the coating during uptake is shown in Figure 7.3.

For WB acrylic coated pine sapwood, the samples with 1 layer and 3 layers have the same uptake behavior, while the ones with 2 layers and 4 layers have the same uptake behavior as well. Note that each layered systems was prepared on different wood panels and that structural variations might affect the results. The variations in the number of layers/thickness had no influence on the barrier properties for WB acrylic coated pine sapwood.

For SB alkyd coated pine sapwood, it took less water in time when the number of layers/thickness was increased, in which the variations in the number of layers/thickness seemed to have an influence on the barrier properties.

For WB acrylic and SB alkyd coated teak, the variations in the number of layers/thickness had no significant influence on the barrier properties. The difference between the systems comes from different initial moisture content. As in the case of pine sapwood, each layered coating systems on teak were prepared on different wood panels. These variations might be due to the structural differences of each individual sample.

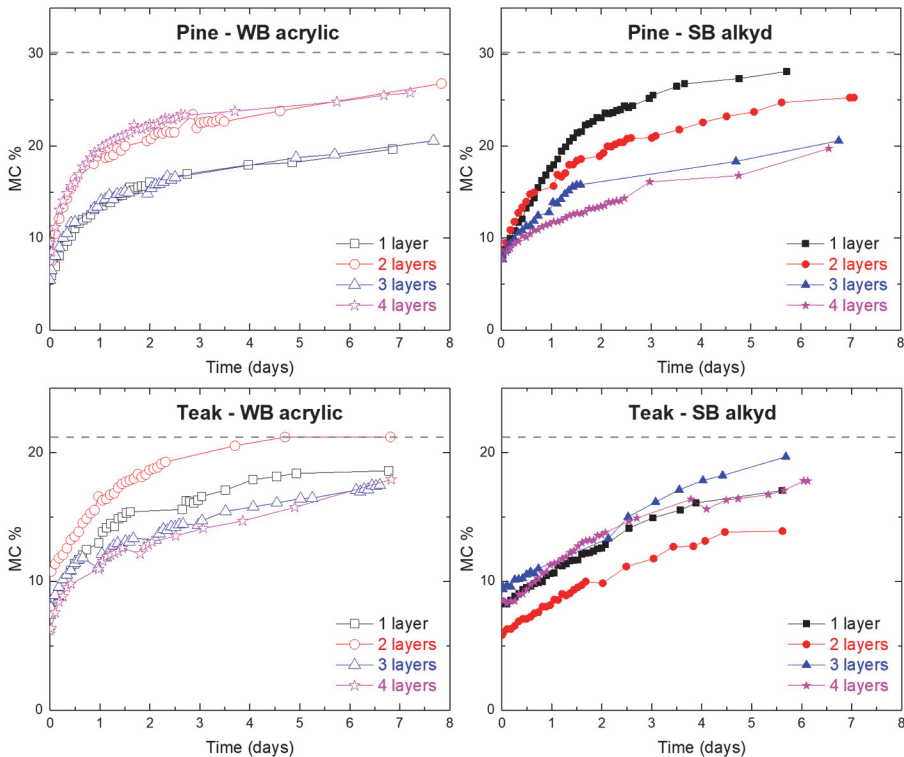


Figure 7.3. The increase in MC of 1 mm region below the coating as a function of time during 1 week water uptake for WB acrylic and SB alkyd coated pine sapwood and teak. The horizontal dashed lines represent the FSP.

Obviously, the variations in the number of layers/thickness had no influence on the barrier properties for WB acrylic coated pine sapwood, and for WB acrylic and SB alkyd coated teak. These preliminary results show the need of a more profound understanding of the variations in the number of layers/thickness on the water transport properties of coatings. While building up multilayered systems, we should introduce bigger difference in thickness to ignore variability in wood.

7.2.3. Curing of alkyds on wood and moisture transport at wood-coating interface

In this section, we will show the possibility to study curing of alkyds on wood and the moisture transport at the wood-coating interface.

In Chapters 2 and 3, in-depth study on the curing of alkyd coatings were performed by applying the coatings on a thin glass slide with a thickness of 140 μm , and measuring with a GARField NMR setup (High Resolution NMR, a spatial resolution of around 6.5 μm). The reason to use this thin glass slide is the position of the insert of the set-up. It measures from

the bottom and has a range of 500 μm in depth. However, in reality, coatings are applied on porous substrates (e.g. wood) instead of glass. Since the wood substrates have a thickness in the millimeter range, a new method that measures from the top of the surface is needed. During the master studies at the Transport in Permeable Media group at TU/e¹⁵⁸, Peter de Vrieze designed an insert to study samples from above, as shown in Figure 7.4.

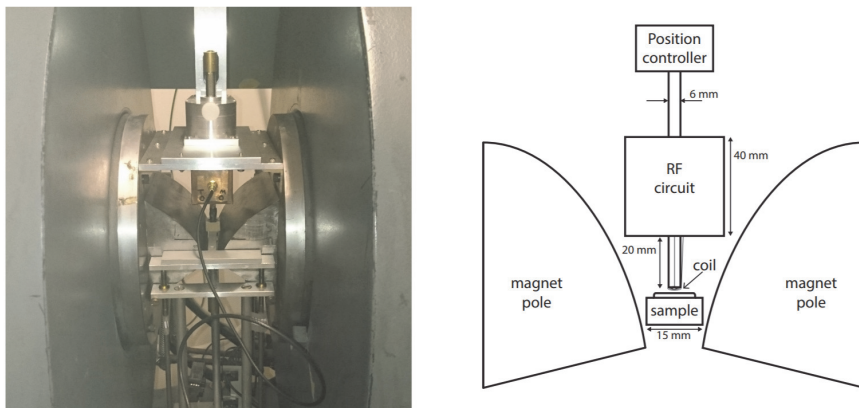


Figure 7.4. Picture (left) and schematic drawing (right) of the new insert designed in this project to study samples from above¹⁵⁸.

This insert has the RF coil above a sample, making it for the first time possible to measure coatings on top of thicker substrates. The insert was able to measure in a range of up to 700 μm at a resolution between 5.5 and 11 μm . Moreover, using a moving average and averaging over echoes it was possible to measure profiles with time intervals of 19.3 s. After designing the insert, the penetration characteristics of alkyd coatings into different types of wood and the crosslinking inside the wood were studied with this insert. In a future study, the influence of cobalt alternatives and secondary driers on the film forming properties of alkyd coatings *on wood* can be studied with High Resolution NMR set-up with this inverse insert.

Secondly, the used parameters Chapters 4, 5 and 6 give a resolution of around 0.5 mm. This low resolution output only provides few data points at the region below the coating. However, the High Resolution NMR set-up with inverse insert can be used for the studies on moisture transport through coatings on wood. This will allow collecting more data points inside the coating, at the wood-coating interface and at the region just below the coating. This opens the door to look into the interfacial layer and will shorten the measuring period significantly.

Bibliography

1. De Boer, J. W. *et al.* The quest for cobalt-free alkyd paint driers. *Eur. J. Inorg. Chem.* 3581–3591 (2013).
2. Soucek, M. D., Khattab, T. & Wu, J. Review of autoxidation and driers. *Prog. Org. Coatings* 73, 435–454 (2012).
3. Lison, D., De Boeck, M., Verougstraete, V. & Kirsch-Volders, M. Update on the genotoxicity and carcinogenicity of cobalt compounds. *Occup. Environ. Med.* 58, 619–625 (2001).
4. Bucher, J. R. *et al.* Inhalation toxicity and carcinogenicity studies of cobalt sulfate. *Toxicol. Sci.* 49, 56–67 (1999).
5. Cobalt REACH Consortium: The classification of its cobalt substances under the EU CLP Regulation.
6. Muizebelt, W. J., Hubert, J. C. & Venderbosch, R. A. M. Mechanistic study of drying of alkyd resins using ethyl linoleate as a model substance. *Prog. Org. Coatings* 24, 263–279 (1994).
7. Hubert, J. C., Venderbosch, R. A. M., Muizebelt, W. J., Klaasen, R. P. & Zabel, K. H. Mechanistic study of drying of alkyd resins using (Z,Z)- and (E,E)-3,6-nonadiene as model substances. *Prog. Org. Coatings* 31, 331–340 (1997).
8. Oyman, Z. O., Ming, W. & Van der Linde, R. Oxidation of model compound emulsions for alkyd paints under the influence of cobalt drier. *Prog. Org. Coatings* 48, 80–91 (2003).
9. Oyman, Z. O. *et al.* A promising environmentally-friendly manganese-based catalyst for alkyd emulsion coatings. *Polymer.* 45, 7431–7436 (2004).
10. Miccichè, F., Oostveen, E., Haveren, J. van & Linde, R. van der. The combination of reducing agents/iron as environmentally friendlier alternatives for Co-based driers in the drying of alkyd paints. *Prog. Org. Coatings* 53, 99–105 (2005).
11. Warzeska, S. T. *et al.* The influence of bipyridine on the drying of alkyd paints: A model study. *Prog. Org. Coatings* 44, 243–248 (2002).
12. Bouwman, E. & Van Gorkum, R. A study of new manganese complexes as potential driers for alkyd paints. *J. Coatings Technol. Res.* 4, 491–503 (2007).
13. Liu, Z., Kooijman, H., Spek, A. L. & Bouwman, E. New manganese-based catalyst systems for alkyd paint drying. *Prog. Org. Coatings* 60, 343–349 (2007).
14. Bieleman, J. H. Progress in the development of cobalt-free drier systems. *Macromol. Symp.* 187, 811–822 (2002).
15. Mallégol, J. *et al.* Influence of drier combination on through-drying in waterborne alkyd emulsion coatings observed with magnetic resonance profiling. *J. Coatings Technol.* 74, 113–124 (2002).
16. Van Gorkum, R. & Bouwman, E. The oxidative drying of alkyd paint catalysed by metal complexes. *Coord. Chem. Rev.* 249, 1709–1728 (2005).

-
17. Muizebelt, W. J., Hubert, J. C., Nielen, M. W. F., Klaasen, R. P. & Zabel, K. H. Crosslink mechanisms of high-solids alkyd resins in the presence of reactive diluents. *Prog. Org. Coatings* 40, 121–130 (2000).
 18. Gorce, J.-P. *et al.* Vertical water distribution during the drying of polymer films cast from aqueous emulsions. *Eur. Phys. J. E. Soft Matter* 8, 421–429 (2002).
 19. Frankel, E. N. Lipid oxidation: Mechanisms, products and biological significance. *J. Am. Oil Chem. Soc.* 61, 1908–1917 (1984).
 20. Wallin, M., Glover, P. M., Hellgren, A. C., Keddie, J. L. & McDonald, P. J. Depth profiles of polymer mobility during the film formation of a latex dispersion undergoing photoinitiated cross-linking. *Macromolecules* 33, 8443–8452 (2000).
 21. Erich, S. J. F., Laven, J., Pel, L., Huinink, H. P. & Kopinga, K. NMR depth profiling of drying alkyd coatings with different catalysts. *Prog. Org. Coatings* 55, 105–111 (2006).
 22. Erich, S. J. F., Laven, J., Pel, L., Huinink, H. P. & Kopinga, K. Influence of catalyst type on the curing process and network structure of alkyd coatings. *Polymer*. 47, 1141–1149 (2006).
 23. Wu, J. Z., Bouwman, E. & Reedijk, J. Chelating ligands as powerful additives to manganese driers for solvent-borne and water-borne alkyd paints. *Prog. Org. Coatings* 49, 103–108 (2004).
 24. Oyman, Z. O., Ming, W. & van der Linde, R. Catalytic activity of a dinuclear manganese complex (MnMeTACN) on the oxidation of ethyl linoleate. *Appl. Catal. A Gen.* 316, 191–196 (2007).
 25. Erben, M., Veselý, D., Vinklársek, J. & Honzíček, J. Acyl-substituted ferrocenes as driers for solvent-borne alkyd paints. *J. Mol. Catal. A Chem.* 353–354, 13–21 (2012).
 26. Kalenda, P., Holeček, J., Veselý, D. & Erben, M. Influence of methyl groups on ferrocene on rate of drying of oxidizable paints by using model compounds. *Prog. Org. Coatings* 56, 111–113 (2006).
 27. Stava, V., Erben, M., Vesely, D. & Kalenda, P. Properties of metallocene complexes during the oxidative crosslinking of air drying coatings. *J. Phys. Chem. Solids* 68, 799–802 (2007).
 28. Kalenda, P., Veselý, D., Kalendová, A. & Št'Áva, V. Ferrocene-based catalyst systems for alkyd paint drying. *Pigment Resin Technol.* 39, 342–347 (2010).
 29. Štáva, V., Veselý, D. & Kalenda, P. Catalytic effects of transition metals in the form of the salts of organic acids in the cross linking of alkyds. *Pigment Resin Technol.* 37, 67–72 (2008).
 30. Pirš, B. *et al.* The Influence of Co/Sr and Fe/Sr Driers on Film Formation of High Solid Alkyd Coatings. *Acta Chim. Slov.* 62, 52–59 (2015).
 31. Pirš, B. *et al.* Iron as an alternative drier for curing of high-solid alkyd coatings. *J. Coatings Technol. Res.* 12, 965–974 (2015).
 32. Bieleman, J. H. *Additives for Coatings.* (Wiley-VCH, 2000).
 33. Froud, C. A., Hayward, I. P. & Laven, J. Advances in the Raman Depth Profiling of

-
- Polymer Laminates. *Appl. Spectrosc.* 57, 1468–1474 (2003).
34. Marton, B. *et al.* A depth-resolved look at the network development in alkyd coatings by confocal Raman microspectroscopy. *Polymer.* 46, 11330–11339 (2005).
 35. Erich, S. J. F., Laven, J., Pel, L., Huinink, H. P. & Kopinga, K. Comparison of NMR and confocal Raman microscopy as coatings research tools. *Prog. Org. Coatings* 52, 210–216 (2005).
 36. Costa, T. L. *et al.* Long-Term Occupational Exposure to Organic Solvents Affects Color Vision, Contrast Sensitivity and Visual Fields. *PLoS One* 7, e42961 (2012).
 37. Böckelmann, I., Pfister, E., Peters, B. & Duchstein, S. Psychological effects of occupational exposure to organic solvent mixtures on printers. *Disabil. Rehabil.* 26, 798–807 (2004).
 38. European Commission. The Paints Directive 2004/42/EC of the European Parliament and of the Council of 21 April 2004: Annex II.
 39. Ahola, P., Derbyshire, H., Hora, G. & de Meijer, M. Water protection of wooden window joinery painted with low organic solvent content paints with known composition. Part 1. Results of inter-laboratory tests. *Holz als Roh- und Werkst.* 57, 45–50 (1999).
 40. Ekstedt, J. & Östberg, G. Liquid water permeability of exterior wood coatings-testing according to a proposed european standard method. *J. Coatings Technol.* 73, 53–59 (2001).
 41. Ekstedt, J. Influence of coating system composition on moisture dynamic performance of coated wood. *J. Coatings Technol.* 75, 27–37 (2003).
 42. Dvinskikh, S. V., Henriksson, M., Mendicino, A. L., Fortino, S. & Toratti, T. NMR imaging study and multi-Fickian numerical simulation of moisture transfer in Norway spruce samples. *Eng. Struct.* 33, 3079–3086 (2011).
 43. Pourmand, P., Wang, L. & Dvinskikh, S. V. Assessment of moisture protective properties of wood coatings by a portable NMR sensor. *J. Coatings Technol. Res.* 8, 649–654 (2011).
 44. van Meel, P. A. *et al.* Moisture transport in coated wood. *Prog. Org. Coatings* 72, 686–694 (2011).
 45. Johansson, J., Blom, Å. & Dvinskikh, S. NMR-measurements for determination of local moisture content of coated wood. *J. Coatings Technol. Res.* 10, 601–607 (2013).
 46. Glover, P. M., Aptaker, P. S., Bowler, J. R., Ciampi, E. & McDonald, P. J. A Novel High-Gradient Permanent Magnet for the Profiling of Planar Films and Coatings. *J. Magn. Reson.* 139, 90–97 (1999).
 47. Hellgren, A.-C. *et al.* New techniques for determining the extent of crosslinking in coatings. *Prog. Org. Coatings* 43, 85–98 (2001).
 48. Erich, S. J. F., Huinink, H. P., Adan, O. C. G., Laven, J. & Esteves, A. C. The influence of the pigment volume concentration on the curing of alkyd coatings: A 1D MRI depth profiling study. *Prog. Org. Coatings* 63, 399–404 (2008).
-

-
49. Erich, S. J. F., Van Der Ven, L. G. J., Huinink, H. P., Pel, L. & Kopinga, K. Curing processes in solvent-borne alkyd coatings with different drier combinations. *J. Phys. Chem. B* 110, 8166–8170 (2006).
 50. Erich, S. J. F., Laven, J., Pel, L., Huinink, H. P. & Kopinga, K. Dynamics of cross linking fronts in alkyd coatings. *Appl. Phys. Lett.* 86, 1–3 (2005).
 51. Mitra, S., Ahire, A. & Mallik, B. P. Investigation of accelerated aging behaviour of high performance industrial coatings by dynamic mechanical analysis. *Prog. Org. Coatings* 77, 1816–1825 (2014).
 52. Quick, J. J., Hailey, J. R. T. & MacKay, A. L. Radial Moisture Profiles of Cedar Sapwood During Drying: A Proton Magnetic Resonance Study. *Wood Fiber Sci.* 22, 404–412 (2007).
 53. Stenström, S., Bonazzi, C. & Foucat, L. Magnetic Resonance Imaging for Determination of Moisture Profiles and Drying Curves. in *Modern Drying Technology, Set* (Wiley-VCH Verlag GmbH & Co. KGaA, 2014).
 54. Robertson, M. B. & Packer, K. J. Diffusion of D2O in archaeological wood measured by 1-D NMR profiles. *Appl. Magn. Reson.* 17, 49–64 (1999).
 55. Donkers, P. A. J., Huinink, H. P., Erich, S. J. F., Reuvers, N. J. W. & Adan, O. C. G. Water permeability of pigmented waterborne coatings. *Prog. Org. Coatings* 76, 60–69 (2013).
 56. Bucur, V. *Nondestructive Characterization and Imaging of Wood*. (Springer Berlin Heidelberg, 2003).
 57. Wiberg, P., Sehlstedt-P, S. M. B. & Morén, T. J. Heat and Mass Transfer During Sapwood Drying Above the Fibre Saturation Point. *Dry. Technol.* 18, 1647–1664 (2000).
 58. Sandberg, K. & Salin, J.-G. Liquid water absorption in dried Norway spruce timber measured with CT scanning and viewed as a percolation process. *Wood Sci. Technol.* 46, 207–219 (2010).
 59. Sedighi-Gilani, M. *et al.* Visualization and quantification of liquid water transport in softwood by means of neutron radiography. *Int. J. Heat Mass Transf.* 55, 6211–6221 (2012).
 60. Erich, S. J. F., Adan, O. C. G., Pel, L., Huinink, H. P. & Kopinga, K. NMR imaging of coatings on porous substrates. *Chem. Mater.* 18, 4500–4504 (2006).
 61. Mallégol, J., Gardette, J.-L. & Lemaire, J. Long-term behavior of oil-based varnishes and paints I. Spectroscopic analysis of curing drying oils. *J. Am. Oil Chem. Soc.* 76, 967–976 (1999).
 62. Lazzari, M. & Chiantore, O. Drying and oxidative degradation of linseed oil. *Polym. Degrad. Stab.* 65, 303–313 (1999).
 63. Mallégol, J., Lemaire, J. & Gardette, J. L. Drier influence on the curing of linseed oil. *Prog. Org. Coatings* 39, 107–113 (2000).
 64. Wang, T. *et al.* Cross-linked network development in compatibilized Alkyd/acrylic hybrid latex films for the creation of hard coatings. *Langmuir* 26, 14323–14333

-
- (2010).
65. Hofland, A. Alkyd resins: From down and out to alive and kicking. *Prog. Org. Coatings* 73, 274–282 (2012).
 66. Lison, D., De Boeck, M., Verougstraete, V. & Kirsch-Volders, M. Update on the genotoxicity and carcinogenicity of cobalt compounds. *Occup. Environ. Med.* 58, 619–25 (2001).
 67. Bucher, J. R. *et al.* Inhalation toxicity and carcinogenicity studies of cobalt sulfate. *Toxicol. Sci.* 49, 56–67 (1999).
 68. Erich, S. J. F., Laven, J., Pel, L., Huinink, H. P. & Kopinga, K. NMR depth profiling of drying alkyd coatings with different catalysts. *Prog. Org. Coatings* 55, 105–111 (2006).
 69. Erich, S. J. F., Laven, J., Pel, L., Huinink, H. P. & Kopinga, K. Influence of catalyst type on the curing process and network structure of alkyd coatings. *Polymer*. 47, 1141–1149 (2006).
 70. Wu, J. Z., Bouwman, E. & Reedijk, J. Chelating ligands as powerful additives to manganese driers for solvent-borne and water-borne alkyd paints. *Prog. Org. Coatings* 49, 103–108 (2004).
 71. Oyman, Z. O., Ming, W. & van der Linde, R. Catalytic activity of a dinuclear manganese complex (MnMeTACN) on the oxidation of ethyl linoleate. *Appl. Catal. A Gen.* 316, 191–196 (2007).
 72. Bieleman, J. H. Progress in the development of Cobalt-free drier systems. in *Macromolecular Symposia* 187, 811–821 (2002).
 73. Oyman, Z. O. *et al.* A promising environmentally-friendly manganese-based catalyst for alkyd emulsion coatings. *Polymer*. 45, 7431–7436 (2004).
 74. Liu, Z., Kooijman, H., Spek, A. L. & Bouwman, E. New manganese-based catalyst systems for alkyd paint drying. *Prog. Org. Coatings* 60, 343–349 (2007).
 75. Bouwman, E. & Van Gorkum, R. A study of new manganese complexes as potential driers for alkyd paints. *J. Coatings Technol. Res.* 4, 491–503 (2007).
 76. Warzeska, S. T. *et al.* The influence of bipyridine on the drying of alkyd paints: A model study. *Prog. Org. Coatings* 44, 243–248 (2002).
 77. Erben, M., Veselý, D., Vinklárek, J. & Honzíček, J. Acyl-substituted ferrocenes as driers for solvent-borne alkyd paints. *J. Mol. Catal. A Chem.* 353–354, 13–21 (2012).
 78. Kalenda, P., Holeček, J., Veselý, D. & Erben, M. Influence of methyl groups on ferrocene on rate of drying of oxidizable paints by using model compounds. *Prog. Org. Coatings* 56, 111–113 (2006).
 79. Stava, V., Erben, M., Vesely, D. & Kalenda, P. Properties of metallocene complexes during the oxidative crosslinking of air drying coatings. *J. Phys. Chem. Solids* 68, 799–802 (2007).
 80. Kalenda, P., Veselý, D., Kalendová, A. & Št'áva, V. Ferrocene-based catalyst systems for alkyd paint drying. *Pigment Resin Technol.* 39, 342–347 (2010).
 81. Št'áva, V., Veselý, D. & Kalenda, P. Catalytic effects of transition metals in the form
-

-
- of the salts of organic acids in the cross linking of alkyds. *Pigment Resin Technol.* 37, 67–72 (2008).
82. Pirš, B. *et al.* The influence of Co/Sr and Fe/Sr driers on film formation of high solid alkyd coatings. *Acta Chim. Slov.* 62, 52–59 (2015).
83. Pirš, B. *et al.* Iron as an alternative drier for curing of high-solid alkyd coatings. *J. Coatings Technol. Res.* 12, 965–974 (2015).
84. Micciché, F., Oostveen, E., Van Haveren, J. & Van Der Linde, R. The combination of reducing agents/iron as environmentally friendlier alternatives for Co-based driers in the drying of alkyd paints. *Prog. Org. Coatings* 53, 99–105 (2005).
85. Hage, R., de Boer, J. & Maaijen, K. Manganese and Iron Catalysts in Alkyd Paints and Coatings. *Inorganics* 4, 11 (2016).
86. Gezici-Koç, Ö. *et al.* In-depth study of drying solvent-borne alkyd coatings in presence of Mn- and Fe- based catalysts as cobalt alternatives. *Mater. Today Commun.* 7, 22–31 (2016).
87. Mallégol, J. *et al.* Influence of drier combination on through-drying in waterborne alkyd emulsion coatings observed with magnetic resonance profiling. *J. Coatings Technol.* 74, 113–124 (2002).
88. Gorkum, R. Van & Bouwman, E. The oxidative drying of alkyd paint catalysed by metal complexes. *Coord. Chem. Rev.* 249, 1709–1728 (2005).
89. Muizebelt, W. J., Hubert, J. C., Nielen, M. W. F., Klaasen, R. P. & Zabel, K. H. Crosslink mechanisms of high-solids alkyd resins in the presence of reactive diluents. *Prog. Org. Coatings* 40, 121–130 (2000).
90. Gorce, J.-P. *et al.* Vertical water distribution during the drying of polymer films cast from aqueous emulsions. *Eur. Phys. J. E. Soft Matter* 8, 421–429 (2002).
91. Frankel, E. N. Lipid oxidation: Mechanisms, products and biological significance. *J. Am. Oil Chem. Soc.* 61, 1908–1917 (1984).
92. Wallin, M., Glover, P. M., Hellgren, A. C., Keddie, J. L. & McDonald, P. J. Depth profiles of polymer mobility during the film formation of a latex dispersion undergoing photoinitiated cross-linking. *Macromolecules* 33, 8443–8452 (2000).
93. Erich, S. J. F., Laven, J., Pel, L., Huinink, H. P. & Kopinga, K. Dynamics of cross linking fronts in alkyd coatings. *Appl. Phys. Lett.* 86, 1–3 (2005).
94. Soucek, M. D., Khattab, T. & Wu, J. Review of autoxidation and driers. *Prog. Org. Coatings* 73, 435–454 (2012).
95. Muizebelt, W. J., Hubert, J. C. & Venderbosch, R. A. M. Mechanistic study of drying of alkyd resins using ethyl linoleate as a model substance. *Prog. Org. Coatings* 24, 263–279 (1994).
96. Dubrulle, L., Lebeuf, R., Thomas, L., Fressancourt-Collinet, M. & Nardello-Rataj, V. Catalytic activity of primary and secondary driers towards the oxidation and hydroperoxide decomposition steps for the chemical drying of alkyd resin. *Prog. Org. Coatings* 104, 141–151 (2017).
97. Froud, C. A., Hayward, I. P. & Laven, J. Advances in the raman depth profiling of

-
- polymer laminates. *Appl. Spectrosc.* 57, 1468–1474 (2003).
98. Marton, B. *et al.* A depth-resolved look at the network development in alkyd coatings by confocal Raman microspectroscopy. *Polymer.* 46, 11330–11339 (2005).
 99. Erich, S. J. F., Laven, J., Pel, L., Huinink, H. P. & Kopinga, K. Comparison of NMR and confocal Raman microscopy as coatings research tools. *Prog. Org. Coatings* 52, 210–216 (2005).
 100. Glover, P. M., Aptaker, P. S., Bowler, J. R., Ciampi, E. & McDonald, P. J. A novel high-gradient permanent magnet for the profiling of planar films and coatings. *J. Magn. Reson.* 139, 90–97 (1999).
 101. Hellgren, A. C. *et al.* New techniques for determining the extent of crosslinking in coatings. *Prog. Org. Coatings* 43, 85–98 (2001).
 102. Erich, S. J. F., Huinink, H. P., Adan, O. C. G., Laven, J. & Esteves, A. C. The influence of the pigment volume concentration on the curing of alkyd coatings: A 1D MRI depth profiling study. *Prog. Org. Coatings* 63, 399–404 (2008).
 103. Erich, S. J. F., Van Der Yen, L. G. J., Huinink, H. P., Pel, L. & Kopinga, K. Curing processes in solvent-borne alkyd coatings with different drier combinations. *J. Phys. Chem. B* 110, 8166–8170 (2006).
 104. Mitra, S., Ahire, A. & Mallik, B. P. Investigation of accelerated aging behaviour of high performance industrial coatings by dynamic mechanical analysis. *Prog. Org. Coatings* 77, 1816–1825 (2014).
 105. Wu, T. H. *et al.* Wet adhesion of epoxy–amine coatings on 2024-T3 aluminum alloy. *Mater. Chem. Phys.* 145, 342–349 (2014).
 106. Erich, S. J. F., Adan, O. C. G., Pel, L., Huinink, H. P. & Kopinga, K. NMR imaging of coatings on porous substrates. *Chem. Mater.* 18, 4500–4504 (2006).
 107. Stamm, A. J. Review of nine methods for determining the fiber saturation points of wood and wood products. *Wood Sci.* 4, 114–128 (1971).
 108. Topgaard, D. & Söderman, O. Changes of cellulose fiber wall structure during drying investigated using NMR self-diffusion and relaxation experiments. *Cellulose* 9, 139–147 (2002).
 109. Casieri, C., Senni, L., Romagnoli, M., Santamaria, U. & De Luca, F. Determination of moisture fraction in wood by mobile NMR device. *J. Magn. Reson.* 171, 364–372 (2004).
 110. Dvinskikh, S. V., Furó, I., Sandberg, D. & Söderström, O. Moisture content profiles and uptake kinetics in wood cladding materials evaluated by a portable nuclear magnetic resonance spectrometer. *Wood Mater. Sci. Eng.* 6, 119–127 (2011).
 111. Riggan, M. T., Sharp, A. R., Kaiser, R. & Schneider, M. H. Transverse NMR relaxation of water in wood. *Journal of Applied Polymer Science* 23, 3147–3154 (1979).
 112. Menon, R. S. *et al.* An NMR determination of the physiological water distribution in wood during drying. *J. Appl. Polym. Sci.* 33, 1141–1155 (1987).
 113. Araujo, C. D., MacKay, A. L., Hailey, J. R. T., Whittall, K. P. & Le, H. Proton magnetic resonance techniques for characterization of water in wood: application to white
-

-
- spruce. *Wood Sci. Technol.* 26, 101–113 (1992).
114. Telkki, V. V., Yliniemi, M. & Jokisaari, J. Moisture in softwoods: Fiber saturation point, hydroxyl site content, and the amount of micropores as determined from NMR relaxation time distributions. *Holzforschung* 67, 291–300 (2013).
 115. Zhang, M. H., Wang, X. M. & Gazo, R. Water States in Yellow Poplar during Drying Studied by Time-Domain Nuclear Magnetic Resonance. *Wood Fiber Sci.* 45, 423–428 (2013).
 116. Thygesen, L. G. & Elder, T. Moisture in Untreated, Acetylated, and Furfurylated Norway Spruce Monitored During Drying Below Fiber Saturation Using Time Domain NMR. *Wood Fiber Sci.* 41, 194–200 (2009).
 117. Hameury, S. & Sterley, M. Magnetic resonance imaging of moisture distribution in *Pinus sylvestris* L. exposed to daily indoor relative humidity fluctuations. *Wood Mater. Sci. Eng.* 1, 116–126 (2006).
 118. Rosenkilde, A. & Glover, P. High Resolution Measurement of the Surface Layer Moisture Content during Drying of Wood Using a Novel Magnetic Resonance Imaging Technique. *Holzforschung* 56, 312–317 (2002).
 119. Kekkonen, P. M., Ylisassi, A. & Telkki, V.-V. Absorption of Water in Thermally Modified Pine Wood As Studied by Nuclear Magnetic Resonance. *J. Phys. Chem. C* 118, 2146–2153 (2014).
 120. Siau, J. F. *Transport Processes in Wood.* 2, (Springer Berlin Heidelberg, 1984).
 121. Hahn, E. L. Spin Echoes. *Phys. Rev.* 80, 580–594 (1950).
 122. Carr, H. Y. & Purcell, E. M. Effects of Diffusion on Free Precession in Nuclear Magnetic Resonance Experiments. *Phys. Rev.* 94, 630–638 (1954).
 123. Gezici-Koç, Ö. *et al.* In-depth study of drying solvent-borne alkyd coatings in presence of Mn- and Fe- based catalysts as cobalt alternatives. *Mater. Today Commun.* 7, 22–31 (2016).
 124. Araujo, C. D., Mackay, A. L., Whittall, K. P. & Hailey, J. R. T. A Diffusion Model for Spin-Spin Relaxation of Compartmentalized Water in Wood. *J. Magn. Reson. Ser. B* 101, 248–261 (1993).
 125. Bulian, F. & Graystone, J. *Wood coatings : theory and practice.* (Elsevier Science, 2009).
 126. Skaar, C. *Wood-Water Relations.* (Springer Berlin Heidelberg, 1988).
 127. Almeida, G., Gagné, S. & Hernández, R. E. A NMR study of water distribution in hardwoods at several equilibrium moisture contents. *Wood Sci. Technol.* 41, 293–307 (2007).
 128. Passarini, L., Malveau, C. & Hernández, R. E. Water State Study of Wood Structure of Four Hardwoods Below Fiber Saturation Point with Nuclear Magnetic Resonance. *Wood Fiber Sci.* 46, 480–484 (2014).
 129. Peemoeller, H. *et al.* NMR detection of liquid-like wood polymer component in dry aspen wood. *Polymer.* 54, 1524–1529 (2013).
 130. Labbé, N. *et al.* Moisture Content and Extractive Materials in Maritime Pine Wood

-
- by Low Field ¹H NMR. *Holzforschung* 56, (2002).
131. Bear, J. & Bachmat, Y. *Introduction to Modeling of Transport Phenomena in Porous Media*. 1, (Springer Science & Business Media, 1990).
 132. Matano, C. On the Relation between the Diffusion Coefficients and the Concentrations of Solid Metals (The Nickel-Copper System). *Japanese J. Phys.* 8, 109–113 (1933).
 133. Sonderegger, W., Glaunsinger, M., Mannes, D., Volkmer, T. & Niemz, P. Investigations into the influence of two different wood coatings on water diffusion determined by means of neutron imaging. *Eur. J. Wood Wood Prod.* (2015).
 134. Gezici-Koç, Ö., Erich, S. J. F., Huinink, H. P., van der Ven, L. G. J. & Adan, O. C. G. Bound and free water distribution in wood during water uptake and drying as measured by 1D magnetic resonance imaging. *Cellulose* 24, 535–553 (2017).
 135. de Meijer, M. & Militz, H. Moisture transport in coated wood. Part 1: Analysis of sorption rates and moisture content profiles in spruce during liquid water uptake. *Holz als Roh- und Werkst.* 58, 354–362 (2000).
 136. Mikac, U. *et al.* Application of MR microscopy for research in wood science. *Microporous Mesoporous Mater.* (2017).
 137. Žlahtič, M., Mikac, U., Serša, I., Merela, M. & Humar, M. Distribution and penetration of tung oil in wood studied by magnetic resonance microscopy. *Ind. Crops Prod.* 96, 149–157 (2017).
 138. Meijer, M., Thurich, K. & Militz, H. Comparative study on penetration characteristics of modern wood coatings. *Wood Sci. Technol.* 32, 347–365 (1998).
 139. Singh, A. P. Advances in Probing Wood-Coating Interface by Microscopy: A Review. *J. Surf. Eng. Mater. Adv. Technol.* 03, 49–54 (2013).
 140. Singh, A. P. & Dawson, B. S. W. Confocal microscope—A valuable tool for examining wood-coating interface. *J. Coatings Technol. Res.* 1, 235–237 (2004).
 141. ISO 2808:2007 - Paints and varnishes -- Determination of film thickness.
 142. ISO 1463:2003 - Metallic and oxide coatings -- Measurement of coating thickness -- Microscopical method.
 143. Erich, S. J. F. *et al.* The influence of calcium and zirconium based secondary driers on drying solvent borne alkyd coatings. *Polymer.* 121, 262–273 (2017).
 144. ASTM D4708 - 12 Standard Practice for Preparation of Uniform Free Films of Organic Coatings.
 145. ASTM E96 / E96M - 16 Standard Test Methods for Water Vapor Transmission of Materials.
 146. Arends, T., Pel, L. & Huinink, H. P. Hygromorphic response dynamics of oak: towards accelerated material characterization. *Mater. Struct.* 50, 181 (2017).
 147. Graystone, J. Moisture transport through wood coatings: The unanswered questions. *Surf. Coatings Int. Part B Coatings Trans.* 84, 177–187 (2001).
 148. Huldén, M. & Hansen, C. M. Water permeation in coatings. *Prog. Org. Coatings* 13,
-

-
- 171–194 (1985).
149. Shreepathi, S., Naik, S. M. & Vattipalli, M. R. Water transportation through organic coatings: correlation between electrochemical impedance measurements, gravimetry, and water vapor permeability. *J. Coatings Technol. Res.* 9, 411–422 (2012).
 150. Brunauer, S., Deming, L. S., Deming, W. E. & Teller, E. On a Theory of the van der Waals Adsorption of Gases. *J. Am. Chem. Soc.* 62, 1723–1732 (1940).
 151. Baukh, V., Huinink, H. P., Adan, O. C. G., Erich, S. J. F. & van der Ven, L. G. J. Predicting water transport in multilayer coatings. *Polymer.* 53, 3304–3312 (2012).
 152. Muizebelt, W. J. & Heuvelsland, W. J. M. Permeabilities of Model Coatings: Effect of Cross-link Density and Polarity. in 110–114 (1986).
 153. Gezici-Koç, Ö., Erich, S. J. F., Huinink, H. P., van der Ven, L. G. J. & Adan, O. C. G. Understanding the influence of wood as a substrate on the permeability of coatings by NMR imaging and wet-cup. *Prog. Org. Coatings* 114, 135–144 (2018).
 154. Sangaj, N. S. & Malshe, V. C. Permeability of polymers in protective organic coatings. *Prog. Org. Coatings* 50, 28–39 (2004).
 155. van der Wel, G. K. & Adan, O. C. G. Moisture in organic coatings — a review. *Prog. Org. Coatings* 37, 1–14 (1999).
 156. Sivadjian, J. & Ribeiro, D. Comparative studies on the permeability to water and to water vapor of plastic materials by the hygrophotographic technique. *J. Appl. Polym. Sci.* 8, 1403–1413 (1964).
 157. Arends, T., Pel, L. & Smeulders, D. Moisture penetration in oak during sinusoidal humidity fluctuations studied by NMR. *Constr. Build. Mater.* 166, 196–203 (2018).
 158. de Vrieze, P. High resolution magnetic resonance imaging of penetration and crosslinking of alkyd coatings on wood. (Technische Universiteit Eindhoven, 2016).

Summary

The awareness of the environmental risks of several coating ingredients has increased much in the last decades. Therefore, more environmental friendly constituents in the coating formulations have gained interest. One is the tendency to replace cobalt-based alkyd driers with more environmentally friendly alternatives. Another environmental issue is the regulations concerning the usage and emissions of volatile organic compounds (VOCs) in coatings, especially in wood coatings.

Alkyd based paints are widely used as air drying coatings. Without any catalysts, the natural drying time of alkyd based coatings would be weeks or months, which is not desirable from the practical point of view. The autoxidation process can be accelerated by adding catalysts, the so-called driers. Regarding the function of driers, they are commonly divided into two main classes: primary and secondary driers. Primary driers promote oxygen uptake, hydroperoxide formation and decomposition processes, whereas secondary driers are said to enhance the crosslinking of the film. As primary driers, cobalt-based driers are the most used drying catalysts as they lead to highly crosslinked and hard films.

There is a clear driver to replace cobalt-based driers by eco-friendlier alternatives as a result of its potential health implications. In Chapter 2, we investigated the influence of cobalt and alternative metals - an iron based and two manganese based driers - on the oxidative drying of alkyd coating films using a combination of techniques. High spatial resolution NMR profiling allows tracing the depth-resolved crosslinking during drying, and is used for the first time in conjunction with time-resolved ATR-FTIR and standard methods like the Beck-Koller (BK) drying test, König hardness and DMA. Based on the results from these different techniques, we found correlations between the drying pattern of driers and properties such as the drying rate, the overall and depth-resolved crosslink density and hardness development. During the drying in the presence of cobalt-based drier, a skin layer is formed that acts as a front and moves towards the bottom of the film. On the other hand, cobalt alternatives exhibit more uniform, i.e. homogeneous, crosslinking throughout the film. Further analyses show that cobalt gives a lower overall drying rate, significantly higher final crosslink density and hardness development compared to its alternatives. These results can be explained by the balance between the speed of crosslinking reactions and oxygen diffusion, which determines the dominating type of drying.

In order to enhance homogeneous drying of the film, primary driers are used in combination with secondary driers. However, each combination of primary and secondary driers leads to a different oxidative drying pattern resulting in variations in the crosslink density and hardness development. In Chapter 3, we investigated the curing behavior of secondary driers, calcium and zirconium, using high spatial resolution NMR. In the beginning of drying,

there is an inhibition period present. The addition of secondary driers reduces the inhibition period. Calcium seems to be more efficient than zirconium in reducing the inhibition period. Furthermore, we observed increased drying speeds and higher crosslink densities when adding secondary driers. While calcium showed to promote the front speed, zirconium showed to increase the measured crosslink density. In a diagram showing both the crosslink density and front speed, the effect of calcium and zirconium can be described as a vector addition, i.e. they have additive effects.

These findings provide an overall update for the paint industry and the ongoing research of cobalt alternatives. For further optimization of cobalt alternatives, the focus of the research should be on understanding the influence of the driers on drying pattern of the film and the role of inhibition period on the drying rate. Front drying works best to obtain densely crosslinked hard films. For a fast drying film with a reasonable crosslink density and hardness, a primary drier in combination with secondary driers promoting homogeneous drying without an inhibition period should be preferred.

Another driver for coating innovation is due to stricter regulations concerning the usage and emission of VOCs. With the regulations on VOCs and new technical developments, waterborne coatings are becoming more and more common in the wood coatings sector. However, waterborne coatings are more sensitive to water compared to solventborne coatings. It has led to an increased interest in studying the influence of coatings on the changes of wood moisture content. Understanding the changes of wood moisture content is of practical importance, since the mechanical properties or the dimensional stability of wood are influenced by the moisture content. Moreover, a high moisture content may result in durability loss due to fungal growth and/or delamination of an applied protective coating. Since protection of the substrate is a main feature of coatings, getting knowledge on how a coating resists and interacts with water is helpful in predicting the service life of the wood substrate and the coating. As a first step, the influencing factors on the coating performance against water should be identified. These factors can be the wood substrate, the type of binder, pigmentation, film thickness, etc.

To investigate water transport through coatings on wood, we started to analyze transport through the wood itself in Chapter 4. Oak, teak and pine sapwood were selected as the wood types covering a whole range of low to high density wood. The first experimental part on uncoated wood was to do the calibration of moisture content for each type with the low resolution NMR. The calibration results allow us to directly quantify the amount of water from the NMR signal during water uptake and drying of wood samples. Relaxation analyses were performed to understand the state of water within the wood, e.g. bound water in the cell wall or free water in lumen or voids. For all wood types, water transport appeared to be internally (i.e. wood) limited during both uptake and drying. This means that the water movement is limited by water transport within the wood. We further found that there is a

unique coupling between the MC and the fractions of bound and free water during uptake and drying. This fact allows to obtain the ratio between each state at any period, just by knowing the MC. For conceptual understanding of transport mechanism, we compared experimentally determined diffusion constants with those derived by the diffusion models. We found that diffusion in the cell wall fibers plays a critical role in the transport process.

While Chapter 4 only deals with wood, coated wood has been studied in Chapters 5 and 6. In all our formulations used in this thesis, we have studied transparent coatings in order to avoid the influence of pigments, especially on the water permeability. Three types of coatings were formulated: a solventborne (SB) alkyd, a waterborne (WB) alkyd and a waterborne (WB) acrylic, specifically for this project.

To understand the influence of the wood substrate on the permeability, we compared water permeability of free films and wood supported films in Chapter 5. We studied free films in two pre-conditioned states, whereas the free films with water treatment are considered as leached and without water treatment as non-leached. This allows to study the differences in the permeability, solubility and diffusion. Non-leached WB films show a significant higher permeability and solubility compared to leached ones. After removal of the hydrophilic material (such as surfactants) in the films by leaching with water, the permeability and solubility values decrease significantly for the WB coatings, but the leaching has no significant influence on the values for the SB alkyd. We found that the permeability of the coatings is similar for leached free films and films on wood. Apparently, the interaction of the coating with the wood has no influence on the permeability for the considered combinations. These results show that wet-cup is a good indication for testing permeability of these coatings, when applied on wood. The films, especially WB systems, should undergo, prior to a wet cup experiment, a leaching process.

Finally, we have demonstrated the direct relation of the permeability with the average water activity inside the coating, which is connected to the activities of both sides of the coating, in Chapter 6. The permeability rises when the average activity increases during uptake, and drops when the average activity decreases during drying. Further, the correlation between the sorption isotherms and the permeability is found to be remarkably well, which proves that the permeability variations are due to the amount of water present in the coating. In overall, the permeability is not about the type of water vapour or liquid present at one side of the coating; it is all about the moisture content of the coating.

Samenvatting

De bewustwording van de omgevingsrisico's van enkele verf-ingrediënten is de laatste jaren enorm toegenomen. Als gevolg hiervan hebben milieuvriendelijke bestandsdelen van coatings een grotere aandacht gekregen. Een van de voorbeelden is de wens om kobalt houdende drogers te vervangen door milieuvriendelijkere alternatieven. Een ander voorbeeld is de regelgeving op het gebied van organische oplosmiddelen (VOCs), vooral in het geval van verf voor houttoepassingen.

Verven gebaseerd op zuurstof drogende alkydhars worden veel gebruikt. Zonder katalysator zou de natuurlijke droogtijd liggen in de orde van enkele weken of maanden, wat ongewenst is vanuit het oogpunt van de toepassing van de verf. Katalysatoren, ook wel drogers genoemd, versnellen het zogenaamde "autoxidatie" proces. Deze drogers worden over het algemeen ingedeeld in twee klassen: primaire drogers en secundaire drogers. Primaire drogers helpen zuurstofopname, hydroperoxide vorming en decompositie. Van secundaire drogers wordt aangegeven dat ze netwerkvorming van de verffilm versnellen. Kobalt is een van de meest veelvuldig toegepaste primaire drogers, met name vanwege het vormen van dichte netwerken.

Er is een duidelijke maatschappelijke wens om kobalt te vervangen door vriendelijkere alternatieven mede vanwege mogelijk gezondheid implicaties. In hoofdstuk 2 wordt de invloed van kobalt en alternatieven voor kobalt drogers, te weten ijzer en twee mangaan houdende drogers onderzocht. De invloed van deze alternatieven op de oxidatieve droging van alkyd verffilms is onderzocht met een combinatie van technieken. Hoge resolutie kernspinresonantie maakt het mogelijk plaatsopgelost het netwerkvormingsproces gedurende de droging te visualiseren. Deze techniek is voor het eerst in combinatie met tijdsopgeloste ATR-FTIR metingen en standaard verfkarakteriseringstechnieken toegepast, waaronder de Beck-Koller (BK) droogtest, König hardheidstest en DMA. Met behulp van deze technieken is een relatie gelegd tussen het droogpatroon, de droogsnelheid, de hardheidsontwikkeling en de plaatsafhankelijke en totale vernettingsgraad. In aanwezigheid van een kobalt houdende droger wordt een huidje gevormd dat als een front naar de onderkant van de verflaag trekt. De onderzochte alternatieven laten een meer homogene droging zien. Analyses op de resultaten laten zien dat kobalt een lagere totale droogsnelheid heeft met een significant hogere vernettingsgraad en hardheidsontwikkeling in vergelijking met de onderzochte alternatieven. Deze resultaten kunnen worden verklaard door de balans tussen de snelheid van vernetten en zuurstoftransport. Deze balans bepaalt het geobserveerde dominante drooggedrag.

Om primaire drogers beter te laten functioneren worden veelal secundaire drogers toegevoegd. Echter, iedere combinatie van primaire en secundaire drogers zorgt voor een

ander drooggedrag, met andere vernettingsgraad en hardheidsontwikkeling. In hoofdstuk 3 wordt met behulp van kernspinresonantie de verandering van drooggedrag onderzocht voor verschillende secundaire drogers, zoals calcium en zirkonium. In het begin van het droogproces wordt een inhibitieperiode geobserveerd. Wanneer de secundaire drogers worden toegevoegd verdwijnt deze inhibitieperiode. Hierbij blijkt calcium effectiever te zijn dan zirkonium. Daarnaast zorgt toevoeging van secundaire drogers tot een verhoogde droogsnelheid en vernettingsgraad. Calcium laat hierin een versnelling van een front zien, terwijl zirkonium een verhoging van de vernettingsgraad laat zien. In een diagram, waarin zowel de vernettingsgraad en frontnelheid wordt weergegeven, blijkt het gecombineerde effect van twee drogers beschreven te kunnen worden met een vectoradditie.

Deze observaties helpen de verfindustrie bij het onderzoek naar alternatieven. Om verdere optimalisatie te bewerkstelligen, zou het onderzoek zich moeten richten op de invloed van de drogers op het drooggedrag van de film en op de inhibitie. Frontdroging werkt het beste op sterk vernette verffilms. Om snelle droging te bewerkstelligen met een redelijke vernettingsgraad en hardheid, verdient het aanbeveling een primaire droger in combinatie met secundaire drogers toe te passen.

Een andere drijfveer voor coating innovatie is de striktere regelgeving op het gebied van gebruik van organische oplosmiddelen. Deze ontwikkeling, in combinatie met nieuwe technologische ontwikkelingen op het vlak van watergedragen verfsystemen, zorgen ervoor dat watergedragen verfsystemen steeds vaker op hout worden toegepast. Echter, watergedragen coatings zijn gevoeliger voor vocht dan solvent gebaseerde verven. Als gevolg hiervan is er een verhoogde interesse in vochtgehalte variaties in hout voor verschillende verven. Begrip hiervan is van praktisch belang, aangezien de mechanische eigenschappen of dimensionele stabiliteit van hout worden beïnvloed door de aanwezigheid van vocht. Bovendien kan, een hoge vochtgehalte de duurzaamheid van hout sterk aantasten door schimmelgroei en/of onthechting van een beschermende verflaag. Aangezien bescherming van het substraat een van de kerneigenschappen van verf is, is het begrip van de barrière eigenschappen van verf van belang om de levensduur van hout en coating te kunnen voorspellen. Als eerste stap moeten de factoren die de barrière eigenschappen bepalen worden achterhaald, zoals substraat, type bindmiddel, pigmentatie en filmdikte.

In hoofdstuk 4 geeft een analyse van het watertransport door hout. Eiken, teak en vuren zijn geselecteerd als referentie hout, met hoge tot lage dichtheid, respectievelijk. Het eerste experimentele werk op ongeverfd hout vond plaats ter kalibratie van het vochtgehalte zoals gemeten met kernspinresonantie. Deze kalibratie maakt het mogelijk om direct het vochtgehalte vanuit de signalen te bepalen gedurende de metingen van het wateropname of droogproces. Signaalrelaxatie analyses werden uitgevoerd om de toestand van het water in het hout te kunnen achterhalen, bijvoorbeeld gebonden water in de cel en vrij water in

lumen of leemtes. Voor alle typen hout blijkt het watertransport bij zowel opname als drogen intern gelimiteerd. Dit betekent dat het opname of droogproces gelimiteerd wordt door het transport in het hout. Daarnaast blijkt er een koppeling te zijn tussen het vochtgehalte en de fracties van gebonden of vrij water, zowel bij drogen als bevochtiging. Deze koppeling zorgt ervoor dat de verhouding tussen de twee fracties bekend is, als alleen al het lokale vochtgehalte bekend is. Om het vochttransport mechanisme te begrijpen, is de experimenteel bepaalde diffusieconstante vergeleken met die van enkele diffusie modellen. Hieruit is gevonden dat diffusie in de celwanden een cruciale rol speelt in het transportproces.

Hoofdstukken 5 en 6 beschrijving verf op hout in tegenstelling tot hoofdstuk 4, waarin alleen naar het hout gekeken is. In onze studies zijn alleen transparante verfformuleringen gebruikt om invloed op watertransport van pigmenten uit te sluiten. Drie verf typen zijn voor deze studie gekozen; een solventgedragen (SB) alkyd, een watergedragen (WB) alkyd en een watergedragen (WB) acrylaat.

Om de invloed van hout substraat op de permeabiliteit te begrijpen is in hoofdstuk 5 waterpermeabiliteit vergeleken van vrije films en films aangebracht op hout. Daarbij zijn vrije films in twee geconditioneerde toestanden onderzocht. De vrije films zijn direct gebruikt of eerst uitgeloozd in water, om het verschil in waterpermeabiliteit, oplosbaarheid en diffusie te kunnen bekijken. Niet uitgeloozde watergedragen vrije verflagen laten een significant hogere permeabiliteit en wateroplosbaarheid zien dan uitgeloozd varianten. Na verwijderen van het hydrofiele materiaal (zoals oppervlakte actieve stoffen) door uitloging, reduceert de permeabiliteit en oplosbaarheid significant, met uitzondering van de solventgedragen systemen. In het geval van solventgedragen systemen blijft de permeabiliteit onveranderd. De studie laat zien dat er geen invloed is van hout op de permeabiliteit, en dat met behulp van de wet-cup methode een goede indicatie gekregen kan worden van de permeabiliteit van lagen op hout. Daarvoor is noodzakelijk om de verflagen uit te logen voor het wet-cup experiment, vooral voor de watergedragen systemen.

In het laatste hoofdstuk 6 wordt getoond dat er een directe relatie is tussen de permeabiliteit en de gemiddelde wateractiviteit in de verflaag. De gemiddelde wateractiviteit is gerelateerd aan de wateractiviteit aan beide zijdes van de coating. De permeabiliteit neemt toe, wanneer de gemiddelde wateractiviteit toeneemt gedurende het opnameproces, en neemt af, wanneer de gemiddelde wateractiviteit afneemt gedurende droging. Daarnaast blijkt er een verband te zijn tussen de gevonden sorptie-isothermen en de permeabiliteit, hetgeen bewijst dat variaties in permeabiliteit het gevolg zijn van de hoeveelheid water in de coating. In essentie wordt geconcludeerd dat de permeabiliteit bepaald wordt door het water in de coating, en niet in welke toestand het water (vloeibare of gasvormige) aan een zijde van de coating zit.

List of publications

Ö. Gezici-Koç, S.J.F. Erich, H.P. Huinink, L.G.J. van der Ven, O.C.G. Adan. 'Moisture content of the coating determines the water permeability as measured by 1D magnetic resonance imaging'. Submitted to *Progress in Organic Coatings*.

Ö. Gezici-Koç, S.J.F. Erich, H.P. Huinink, L.G.J. van der Ven, O.C.G. Adan. 'Understanding the influence of wood as a substrate on the permeability of coatings by NMR imaging and wet-cup'. *Progress in Organic Coatings*, 114, 135-144 (2018).

S.J.F. Erich*, **Ö. Gezici-Koç***, M.B. Michel, C.A.A.M. Thomas, L.G.J. van der Ven, H.P. Huinink, J. Flapper, F.L. Duivenvoorde, O.C.G. Adan. 'The influence of calcium and zirconium based secondary driers on drying solvent borne alkyd coatings'. *Polymer*, 121, 262-273 (2017). (*Equally contributed)

Ö. Gezici Koç, S.J.F. Erich, H.P. Huinink, L.G.J. van der Ven, O.C.G. Adan. 'Bound and free water distribution in wood during water uptake and drying as measured by 1D magnetic resonance imaging'. *Cellulose*, 24(2), 535-553 (2017).

Ö. Gezici-Koç, C.A.A.M. Thomas, M.B. Michel, S.J.F. Erich, H.P. Huinink, J. Flapper, F.L. Duivenvoorde, L.G.J. van der Ven, O.C.G. Adan. 'In-depth study of drying solvent-borne alkyd coatings in presence of Mn and Fe based catalysts as cobalt alternatives'. *Materials Today Communications*, 7, 22-31 (2016).

Ö. Gezici, I. Durmaz, E. Bilget Guven, O. Unal, A. Ozgun, R. Cetin-Atalay, D. Tuncel. 'Dual functionality of conjugated polymer nanoparticles as an anticancer drug carrier and a fluorescent probe for cell imaging'. *RSC Advances*, 4(3), 1302-1309 (2014).

V. İbrahimova, S. Ekiz, **Ö Gezici**, D. Tuncel. 'Facile synthesis of cross-linked patchy fluorescent conjugated polymer nanoparticles by click reactions'. *Polymer Chemistry*, 2, 2818-2824 (2011).

Acknowledgement

When I started this journey, the end seemed very far to reach. But now, this is the very happy end with a degree and the collection of so many nice people that I met during this journey. I am one of the lucky people who can remember PhD period with a big smile on my face.

First of all, I would like to thank my promotor Prof. Olaf Adan for giving me the opportunity to perform my PhD studies in his group. Olaf, thank you for your encouragement, trust, guidance, criticism, and motivating support throughout my studies. Also your leadership during my first canoe experience was very valuable for me to complete it dry.

I would like to thank my second promoter, Prof. Joseph Keddie, for his motivating and supporting comments on my thesis. I would also like to thank my committee members for being a part of my PhD defense ceremony and for their valuable feedback on the thesis.

Bart, this thesis would not be possible without your help and guidance. I am grateful for your being my supervisor. In the beginning, you were the hardest challenge for me with your endless energy during our meetings that it was very hard to keep you focused on one single subject. But after I learn how to deal with your multi-thinking, every meeting was so fruitful and instructive. I will never forget your visit to Turkey for my wedding and your wonderful (mükemmel) Turkish dance at the party. And thank you for Dutch summary of the thesis.

Henk, thank you for your invaluable help along this journey. Your supervision with your excellent skills in theory and structuring the complex issues made my results even more concrete and appealing.

Leo (van der Ven), I want to express my gratitude to you. Your infinite and invaluable knowledge in coatings contributed a lot to this thesis. You are the one whom I could experience Dutch punctuality and discipline. You are also the one whom I felt like a family member. The chats with you were always warm and sincere. After I returned to Turkey, you helped me not to lose the track of this study. And you were also there to share my grief.

I am thankful for TU/e, TNO and AkzoNobel Decorative Paints for the collaboration and funding this project. I would like to thank AkzoNobel team; Joldert Faber, Michel Rosso, Francis Duivenvoorde and Anthonie Stuiver for useful discussions; Paul van de Keer for optical microscope images; Jie Zhao, Patrick Grosze Nipper and Andre Schaap for samples preparation and analysis measurements.

Charlotte and Marc, thank you very much for your hard work during your internship period. I am very happy to have had you as my first master level student supervising experience. One year of work from each of you with inspiring outcome resulted in two publications, which are Chapters 2 and 3 of this thesis. I would also like to thank Jitte Flapper and Francis Duivenvoorde from AkzoNobel Decorative Paints for giving this internship opportunity to

them and their collaboration with TPM group at TU/e. Jitte and Francis, thank you very much for useful and comprehensive discussions during our meetings and your valuable contribution to the articles we published together.

I would like to thank Berit Wassenaar for her contribution to this study during her Bachelor end project. Berit, I was very happy for supervising (together with Henk) you as my first student. I would also like to thank, Jef for his help in technical issues; Hans for his assistance to use some instruments and his exceptional inventory; Henk and Ginny from the workshop for their help in designing and making the wood samples and teflon holders; Marc van Maris for CT images.

Nicolae, I also benefited from your regular visits to TPM by having good chats. It was an unforgettable memory that you and your wife Mariana invited me and my husband Ali to your house for dinner with a delicious Romanian cuisine.

Wendy, thank you very much for all your help to make my life easier in the Netherlands. I always enjoyed having chat with you, and appreciated your continuous support.

Kateryna and Kees, thank you for making me the luckiest person for being an officemate of you. You were always there when I needed any work-related help or a good conversation.

Kees, I always admired your great skills in presenting and your self-confidence. And your optimistic attitude always comforted me even at my saddest moments. Kateryna, you became a very good friend of me. You were very generous for serving sweets, cakes, various types of teas and giving gifts. Now my home is full of many pieces from you. Thanks for accepting being my paranimfen.

Sonia and Raheleh, I always enjoyed with our plans after work and on weekends. Raheleh, you are a perfect cook, I loved Iranian cuisine. Sonia, I appreciated your efforts to make food less spicy when you invited non-Indian friends.

Pim, thank you very much for all your help during my studies. I am also very grateful for your friendship. I enjoyed a lot at the borrels and afterwards dinners. When Ali and me were looking for a place to stay at the last month of our Eindhoven period, you let us stay at your home for a month. I am still very grateful with this help.

I would like to express my sincere thanks to my other colleagues of TPM group; Ahmed, Anja, Benjamin, Cemal, Faiyas, Jinping, Jo-Hendrik, Karel, Klaas, Leo, Leyla, Loes, Marlouke, Michiel, Mirjam, Negar, Nico, Okan, Peter, Philip, Sofii, Stephan, Steven, Tamerlan, Thomas and Victor. You made a nice atmosphere to work. I will miss the lunches, the coffee breaks and borrels with you.

My friends in Cascade, Özge and Altuğ, thank you very much for your open doors whenever I need a good chat in my own language. Alessandro, Guilia and Alvaro, our last year together was much more fun with you.

Thanks to all members of Turkish Drama Club “Kulis” who made Eindhoven like a hometown. Başta Sevinç hocam olmak üzere, ailemden uzaktayken bana bir ablanın bir annenin sıcaklığını hissettiren Ayşe ablam ve İnci ablama çok teşekkür ederim. Ve diğer tüm

Tiyatro Kulis üyeleri; Nazlı, Ayşe, Yeşim, Aygöl, Reyhan, Orkun, Ayhan, Mehmet, Suzan, Çağrı, Suat abi, Ali, Ferah, Hacer, Mehtap, Damla sizleri tanımış olmaktan dolayı çok mutluyum ve paylaştığımız tüm anılar için çok teşekkür ederim.

Hollanda'daki yıllarımı kolaylaştıran ev arkadaşım Rukiye ve annesi, komşularımız Sunay abla ve Selçuk abi, canım akrabam Makbule ve sevgili ailesi, aile sıcaklığını yaşattığınız için çok teşekkür ederim. Tezimin kapak fotoğrafı için özenle çalışan canım arkadaşım Rengin ve sevgili eşi İsa, çok teşekkür ederim.

Bu yolda desteğini esirgemeyen annelerim ve babalarım sizleri çok seviyorum. Kardeşlerim Gizem ve İsa, paylaşabilmenin güzelliğini sizlerle yaşayabildiğim için çok şanslıyım. Ali'min anne-ablası benim de kendimi bileli olmasını istediğim ablam Mehvar, Ali Âli abi ve Ali Selim, moral ve destek olduğunuz için çok teşekkür ederim.

Bu tezin tamamlanabilmesindeki en büyük destekçim eşim Ali Vâlâ, sana teşekkürlerim sözcüklere dökübilmenin çok ötesinde. Ali'm, senin sonsuz sabrın, sevgin, anlayışın ve desteğin bu dereceyi alabilmemde en büyük rolü oynadı.

Her zaman 'Neşe'li annem, her süreçte yanımda olduğun gibi bunu bitirirken de yanımda olabilseydin, savunmamı yaparken benden çok daha heyecanlı bir şekilde en önde oturacağını biliyorum. Seni çok özlüyorum...

Curriculum Vitae



Özlem Gezici Koç was born on 17th of August 1986 in İzmir, Turkey. She studied Chemistry with a full scholarship at Bilkent University in Ankara, Turkey; ranked 1st in the Department of Chemistry and 2nd in the Faculty of Science in graduation in 2009. During her master studies between 2009 and 2011, she studied Biotechnology and worked as Research&Teaching Assistant at İzmir Institute of Technology, Turkey. She transferred to Bilkent University to complete her master studies in Chemistry with a specialization in synthetic organic chemistry; graduated with *magna cum lauda* in 2012. In 2011 Fall semester, she received Bilkent University Department of Chemistry Best Teaching Assistant Prize. She was a recipient of MSc Scholarship from Scientific and Technological Research Council of Turkey (TUBITAK). She also received Bachelor Degree in Business Administration at Anadolu University, Eskişehir, Turkey in 2011 (open and distance learning).

In September 2012, she started a PhD project at the Eindhoven University of Technology (TU/e) in the group of Transport in Permeable Media (TPM) under the supervision of Prof.dr.ir. Olaf Adan and Dr.ir. Bart Erich. The project is financed by AkzoNobel Decorative Coatings (Sassenheim, the Netherlands) in close collaboration with TNO (the Netherlands Organization for Applied Scientific Research). The most important results of this research are presented in this dissertation. Since March 2018, she is employed at TUBITAK (Ankara, Turkey) as a scientific expert and National Contact Point for *Nanotechnology, Advanced Materials, Advanced Manufacturing and Production Technologies* theme in Horizon2020.